UC San Diego
UC San Diego Electronic Theses and Dissertations

Title

Micro to Macro Investigation of Post-Wildfire Mudflow Initiation Mechanisms

Permalink

Author

Movasat, Mahta

Publication Date

2022

Peer reviewed|Thesis/dissertation

UNIVERSITY OF CALIFORNIA SAN DIEGO

Micro to Macro Investigation of Post-Wildfire Mudflow Initiation Mechanisms

A dissertation submitted in partial satisfaction of the requirements for the degree
Doctor of Philosophy

in

Structural Engineering

by

Mahta Movasat

Committee in charge:

Professor Ingrid Tomac, Chair
Professor Tara Hutchinson
Professor Peter Krysl
Professor Tajana Simunic Rosing
Professor Qiang Zhu

2022

The Dissertation of Mahta Movasat is approved, and it is acceptable in quality and form for publication on microfilm and electronically.

University of California San Diego

2022

DEDICATION

To my love, *Neema*, for being the sunshine and hope in my life,

to my mom, for being my motivation,

and to my dad, for being my inspiration.

TABLE OF CONTENTS

LIST OF FIGURES

LIST OF TABLES

LIST OF SYMBOLS

a, b Fitting parameters

C Tuning parameter

C_c Coefficient of curvature

C_{def} Factor of shape distortion

C_t Factor of turbulence inflow around the drop

C_u Coefficient of uniformity

C_τ Factor related to turbulence

c' Effective cohesion

Dr Relative density

D_c Crater diameter

D_{max} Maximum Drop diameter

$D_{(t)}$ Drop spread diameter at time (t)

D_0 Drop diameter

D_{10} Particle diameters defining 10% finer from the grain-size distribution curve

D_{50} Median grain size

D_{60} Particle diameters defining 10% finer from the grain-size distribution curve

E Impact energy

E_k Kinetic energy

E_{rex} Dimensionless rebound criterion

FN False Negatives

FP False Positives

$H(t)$ Height that the drop has to travel before reaching the 95% of terminal velocity

h Wettable layer thickness.

i Hydraulic gradient

J Seepage force

K_s Splash factor

k Permeability

$L(\lambda)$ Likelihood function

MSE Mean square error

M_c Number of columns for surface roughness measurement with Profilm3D Optical Profiler

M_r Number of columns for surface roughness measurement with Profilm3D Optical Profiler

$m_{(t)}$ Ratio of the infiltration depth to failure depth

N van Genuchten curve shape parameter, the measure of the pore size distribution

n Porosity

Oh Ohnesorge number

P Probability of occurrence of an event, logistic function (sigmoid function ($\sigma(x)$))

p Pressure

Q_t Cumulative water discharge

q Water discharge

q_n Normalized water discharge

q_p Peak water discharge

Re Reynolds number

RI Rain intensity

R^2 Coefficient of determination

Re^* Effective Reynolds number

r Roughness factor

S Spreading coefficient

S_q Soil surface roughness

t Time

$t_{failure}$ Infinite slope Failure time

t^* Dimensionless time

TN True Negatives

TP True positives

TS Threat score

v Velocity

$v(t)$ Drop velocity at each moment

v_d Downhill velocity

v_i Impact velocity

v_t Terminal drop velocity

$WDPT$ Water drop penetration time

We Weber number

W_N Normal gravitational force

W_T Tangential gravitational force

We_N Normal Weber number

We^* Effective Weber number

$X_1, X_2, \ldots, X_P$ Machine learning input features (variables)

x_{si}, y_{sj} Sampling point coordinates for surface roughness measurement with Profilm3D Optical Profiler

Z Profile height for surface roughness measurement with Profilm3D Optical Profiler

Z_c Maximum crater depth

z Failure depth

z_{inf} Infiltration depth

α Parameter related to the inverse of air/water entry value on drying/wetting curve

β Spread factor

β_{max} Maximum spread factor

γ Wet unit weight of soil

γ_{LS} Interfacial energy between liquid and solid

γ_{LV} Interfacial energy between liquid and vapor

γ_{SV} Interfacial energy between vapor and solid

γ_{eff} Effective surface tension

γ_{sat} Saturated unit weight of soil

γ_w Unit weight of water

γ' Buyout unit weight of soil

Δ Displacement

ΔG Gibbs free energy change

δ Slope Gradient/inclination

δ^* Seepage angle with respect to horizontal line

$\Theta(\psi)$ Water retention curve

Θ_r Residual water content

Θ_s Saturated water content

θ Static contact angle

θ_{C-B} Cassie-Baxter contact angle

θ_w Wenzel contact angle

θ_e^Y Static equilibrium contact angle on a flat smooth silica surface

$\kappa_{11}, \kappa_{21}, \dots, \kappa_{p1}$ Loading of the first principal component

$\lambda_0, \lambda_1, \dots, \lambda_p$ Optimal coefficients

μ_a Air dynamic viscosity

μ_f Fluid's dynamic viscosity

ϑ_p Effective viscosity

ρ_d Dry density of soil

ρ_w Density of water

ρ_a Density of air

σ_s Fluid surface tension

σ Normal stress

τ Shear stress

ω Response time

φ_s Solid fraction

φ' Effective friction angle

φ Friction angle

$|\psi|$ Suction pressure

Ψ_{wev} Water entry value

ACKNOWLEDGEMENTS

First, I would like to thank my advisor, Dr. Ingrid Tomac, for her support during my Ph.D. process. It has been a great opportunity for me to work with Dr. Tomac, and I would like to thank her for her insight and trust. I joined this program with a master of Geotechnical Engineering, with an experimental background of geotechnical earthquake engineering, and I had the opportunity to work on different scale studies from micro to macro and gain a lot of knowledge in different areas.

To my dissertation's committee members, Drs. Tara Hutchinson, Peter Krysl, Qiang Zhu, and Tajana Simunic Rosing, I am greatly appreciative of their review, feedback, and support during this research and my various interactions with them during my time at UC San Diego.

Thank you to the other faculty, our department dean, Dr. John McCartney, staff, and fellow students for their support during my time in this program. Special thanks to Yvonne Wollmann for her encouraging conversations and support. Thank you to Julie Storing, Joana Halnez, Sandra de Sousa, Kyung Brown, and Lindsay Walton. Without your help, I wouldn't have been able to succeed in this journey. My dear friends, Theresa Richards, Chaohsien Li, Brian Yamashiro, Jeffrey Thomas Newgard, Kuanpo Lin, Xiaolong He, Wenpei Ma, I truly appreciate your friendship and support feel so lucky to get to know you. I wish to thank my previous advisor, Dr. Masoud Hajialilue-Bonab for being a great mentor in my life.

I want to thank my parents, who have always believed in me and supported me. In the first place, my father has been my inspiration to be a civil engineer. Your memories are always with me. Thanks for giving me the courage and confidence to follow my dreams.

Thank you most of all to my love, *Neema*. You are always there by my side with all your kindness and generosity. Thanks to your family for their support and encouragement during this time.

This dissertation contains a combination of published and unpublished material, as described below.

Chapter 2 is based on materials from a manuscript entitled "Assessment of Physical Properties of Water-Repellent Soils" with authors Movasat, M., and Tomac, I. (2021) published in *Journal of Geotechnical and Geoenvironmental Engineering*, 147(9), 06021010. The dissertation author was the first investigator and author of this paper.

Chapter 3 is based on materials from a manuscript prepared entitled "Granularity Role of Water Repellent Sand Particles on Post-Impact Dynamics of Water Droplet" with authors Movasat, M., De La Cruz, A., and Tomac, I. The dissertation author was the first investigator and author of this paper.

Chapter 4 is based on materials prepared for the manuscript entitled "Effect of Spatial Variability and Granularity of Water Repellent Layer on Post-Wildfire Debris Flow Initiation Mechanism" with authors Movasat, M., and Tomac, I. The dissertation author was the first investigator and author of this paper.

Chapter 5 presents the machine learning framework for post-wildfire mudflow onset classification.

Each chapter is presented with its own specific conclusions, but Chapter 6 includes general conclusions from the numerical and experimental studies in this dissertation. The references from each of the individual chapters are presented together at the end of the dissertation.

VITA

2016   Bachelor of Science in Civil and Environmental Engineering, University of Tabriz, East Azerbaijan, Iran

2018   Master of Science in Geotechnical Engineering, University of Tabriz, East Azerbaijan, Iran

2022   Doctor of Philosophy in Structural Engineering, University of California San Diego, La Jolla, United States

Field of Study: Geotechnical Engineering

PUBLICATIONS

Movasat, M., and Tomac, I. (2022a). "The Effect of Grain Size on Rainfall-Triggered Debris Flow in Hydrophobic Granular Slopes." Geo-Congress 2022, 417–424.

Movasat, M., and Tomac, I. (2022b). "Evaluation of Post-Impact Behavior of Single Droplet on the Hydrophobic Soil Surface." Geo-Congress 2022, 425–432.

Movasat, M., and Tomac, I. (2021). "Assessment of Physical Properties of Water-Repellent Soils." Journal of Geotechnical and Geoenvironmental Engineering, 147(9), 06021010.

Movasat, M., and Tomac, I. (2020a). "Post-Fire Mudflow Prevention by Biopolymer Treatment of Water Repellent Slopes." In Geo-Congress 2020: Biogeotechnics, American Society of Civil Engineers, Reston, VA, 170–178.

Movasat, M., and Tomac, I. (2020b). "Evaluation and remediation of post-wildfire slope stability." E3S Web of Conferences, EDP Sciences, 04007.

Movasat, M., & Tomac, I. (2020, December). Understanding the onset of mudflows and rainwater droplet impact dynamics on hydrophobic tilted surfaces. In AGU Fall Meeting Abstracts (Vol. 2020, pp. NH006-08).

Movasat, M., & Bonab, M. H. (2019). Experimental study of soil-structure interaction on the improved ground by micro piles using shaking table. 8th International Conference on Seismology and Earthquake Engineering (SEE8), University of Tehran

Hajialilue-Bonab, M., Farrin, M., & Movasat, M. (2018). Shaking table test to evaluate the effects of earthquake on internal force of Tabriz subway tunnel (Line 2). In Physical Modelling in Geotechnics (pp. 797-801). CRC Press.

N. Ghanbari, M. Hoseinzadeh Asl & M. Movasat. (2017). The effect of bolts arrangement on the stiffness of rigid connections with end plate. 5th International Congress on Civil Engineering, Architecture & Urban Development, Shahid Beheshti University, Tehran, Iran.

ABSTRACT OF THE DISSERTATION

Micro to Macro Investigation of Post-Wildfire Mudflow Initiation Mechanisms

by

Mahta Movasat

Doctor of Philosophy in Structural Engineering

University of California San Diego, 2022

Professor Ingrid Tomac, Chair

Catastrophic mudflows and landslides, triggered by rainfall can occur suddenly and move with high speed, damaging infrastructure and threatening humans, are increasing due to the climate change. The risk of mudflows increases in post-wildfire areas mainly due to water repellent soil from burned soil organic matter gases. This research investigates mudflow initiation mechanisms by integrating micro, macro and machine learning approaches. The study shows modifications to drop dynamics on post-wildfire slopes, which is a precursor of erosion processes on granular post-

wildfire slopes. High-speed video recordings of impact of a single drop on both hydrophobic and regular grains revealed the significant effect of the sand grain size and hydrophobicity on the drop shape transformation, spreading, and splash. Specifically, the drop spread factor, fitted to a power law of *We/Oh* ratio, is larger on the hydrophobic than hydrophilic sand, and the maximum drop spread increases approximately 40% in fine compared to coarse sand. Moreover, hydrophobizing the sand grain drops the splash initiation threshold approximately 75% in fine sand. The effect of grain size on drop mobility is attributed to Cassie-Baxter and Wenzel wetting regimes, where we observed higher drop velocities and partial bounces in case of Cassie-Baxter model on fine sands, while the velocities dropped about 6.5 times in case of Wenzel model on coarse sand. A macro-investigation on the effects of spatial variability of the post-wildfire hydrophobic layers, with different grain size and under varied rain intensities and slope gradients, identifies failure mechanisms in these layouts. The results quantify a seepage-induced infinite failure mechanism with respect to time to failure, sediment discharge and water infiltration and overflow dynamics. Furthermore, surficial erosion patterns are linked to sand grain sizes, rain intensities, and sediment discharge in the surficial hydrophobic layer. The fine sand has been identified as the most vulnerable soil type in both layouts. A logistic regression model is built to identify the probability of infinite failure based on the experimental results. Despite the small amount of data, the model predictions are promising and indicates the advantage of using machine learning technics in wiser selection of critical parameters.

1. Introduction

1.1 Research motivation

Every year wildfires burn acres of lands around the world and in United States. Wildfires induce water repellency or hydrophobicity in surficial soil layers, which largely enhances the surface runoff and erosion that lead to economic disaster, injury, and life loss (1,2) (Figure 1.1). Changes in hillslope hydrological characteristics increase risks of overland flow and mudflows, which cause a significant threat to communities, infrastructure, and agriculture. Post wildfire hydrophobicity has become important since the frequency and duration of wildfires have increased in the past few decades. In the western USA factors such as increased spring and summer regional temperature and early spring snowmelt contributes to the increased frequency and duration of wildfires (3).
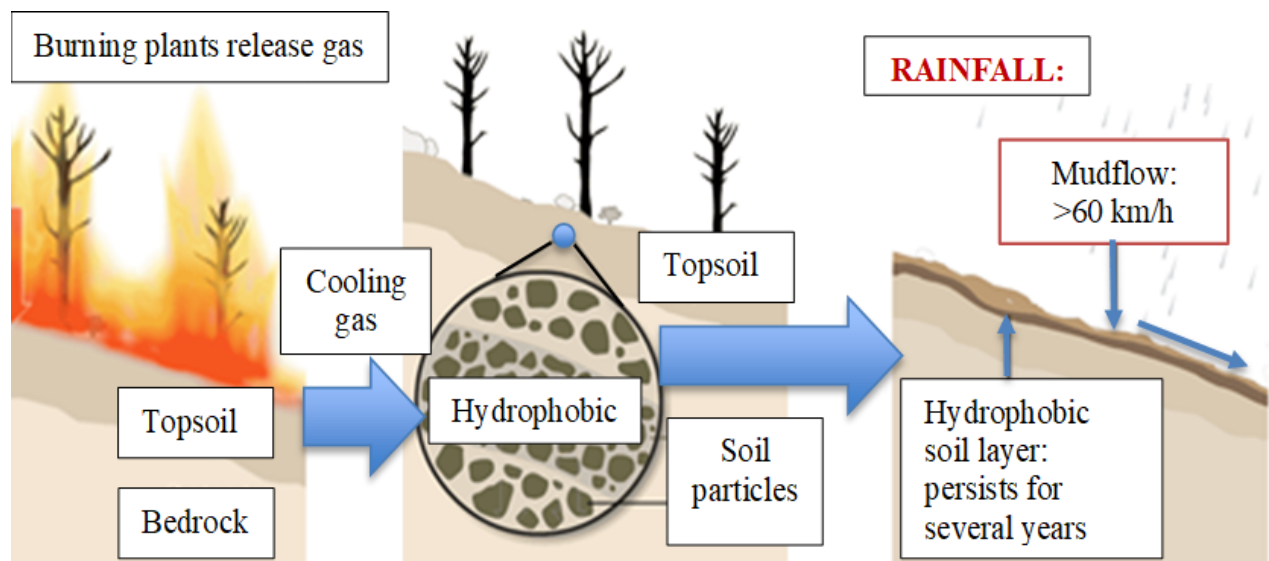
Figure 1.1 Process of hydrophobic layer formation after fire and mudflow occurrence

Water repellency is a phenomenon in which soil resists water absorption and water droplet beads on the soil surface. In addition, the water repellency prolongs the wetting process, increases soil erosion, loss of vegetation, forms preferential flow paths, changes watersheds' hydrological characteristics, and causes catastrophic mudslides (4,5). During fire, the accumulated organic matter burns in soil, and by-product gasses build a water-repellent layer on soil grain surfaces during fire intervals (1). The surface hydrophobicity lowers the grain surface energy and weakens the attraction between liquid and solid; thus, the surface tension of the water droplet dominates, and the drop does not spread on the grains (6). The amount of organic matter, soil texture, fire severity, and vegetation type affect water repellency levels in soil (7). Higher soil erosion rates occur in burned than unburned forests (8). Several rainfall-triggered mudflows and debris flows are reported worldwide, including in western United States areas burned by fire earlier, such as the debris flow in Montecito after the Thomas fire in California (9–12). As reported in the literature, infiltration-triggered soil slip and runoff-dominated erosion by surface runoff are two dominant debris flow initiation processes in areas that have experienced fire (13). The studies show that fire occurrence is an important factor in the erosive process of soil and mudflows and rainfalls and storms in post-fire areas pose a significant threat to people living in the vicinity of hills and mountainous areas. Despite limited available predictions and weather forecasts, mudflows in burned scars occur suddenly and remain unpredictable.

This research includes micro and macro studies of rain impact and erosion onset of hydrophobic soil. First, the physical and mechanical properties of post-wildfire soil are investigated, followed by studying the dynamics of a single drop on hydrophobic sand to observe and relate the effects of soil hydrophobicity and reflect it on the mechanism of mudflow and debris flow initiation. Finally, the macro study includes the rainfall simulation tests on hydrophobic

slopes that will relate soil properties to rain and slope characteristics to better understand mudflow onset and perform machine learning technics as a framework for future post-wildfire mudflow risk assessment. This study aims to identify how the soil surface hydrophobicity level and presence of different soil types induce surficial failure mechanisms and will relate grain size distribution, slope angle, granular soil type and hydrophobicity level with the erosion pattern.

1.2 Research Objectives

The overall aim of this research is to understand the mechanism underlying the debris flow and mudflow initiation in post-wildfire areas and conducting in-depth investigation to study the effect of various factors such as heterogeneity, grain size, hydrophobicity of sand by controlling relevant external factors such as rain intensity, slope gradient and layer configuration. The fundamental and applied research objectives of this study are:

- Assess the applicability of laboratory-made hydrophobic soils for studying mudflows by comparing them to natural hydrophobic soils collected from two burned sites.

- Measure the soil-water entry values and soil water retention curves (SWRC) of the hydrophobic soil.

- Understand the effect of hydrophobicity and granularity on spread behavior and splash threshold of water drop on regular and burned hills.

- Quantify the time-dependability of the erosion process and effect of grain size, hydrophobicity, and slope gradient on the development of the erosion process and amount of water discharge and erosion rate.

- Relate the micro behavior of droplets on hydrophobic soil to the macro-onset mechanism of the erosion and mudflows and identify the soil type that is the most susceptible to mudflows.

- Classify and predict the mudflow likelihood for the tested results with machine learning models such as logistic regression, support vector machine, and multiple linear regression.

1.3 Research Approach

To evaluate the applicability of laboratory-made hydrophobic soil to study the post-wildfire hydrophobic soils, artificial hydrophobic soil is prepared in the laboratory and compared to the properties of two post-wildfire naturally hydrophobic soils, collected from two burnt areas in southern California. Various physical and mechanical properties, as well as hydraulic properties, are investigated with simple shear tests, scanning electron microscopy, water entry and water retention tests. In addition, the collected soil samples are tested one year later to investigate the hydrophobicity severity and water retention characteristics of soil after one year.

The effect of rain drop behavior on hydrophobic and regular sand is investigated by a series of tests, using an automated dropper and prepared hydrophobic and regular surfaces with different size grains, fine, medium and coarse. The post-impact behavior of the drops is captured using high speed camera and video recordings quantify micromechanics and energy effects of surface on drop behavior. The spreading and splashing behaviors are determined and compared for different grain sizes and wettability.

The onset mechanism of post-wildfire soils is studied experimentally by building a rain simulator, sand box with two flumes and pumping system. Three fine, medium and coarse grain

sands are used to study the effect of grain size, and two different layer configurations are tested to study the effect of spatial variability of the hydrophobic layer on the failure triggering mechanism. Rainfall intensity and slope gradient are also altered to determine their effect on the amount of water discharge and sand erosion rate.

Finally, the experimental data are trained with various machine learning classification models. The models are evaluated using confusion matrices and precision and accuracy results. In addition, a logistic regression model is trained to determine the likelihood of infinite failure occurrence and sensitivity analysis are performed to demonstrate the sensitivity of the model over a representative range of values for an individual variable.

1.4   Dissertation Organization

This dissertation is prepared as a paper-based dissertation. The different chapters are comprised of excerpts of drafts, submitted or published works in peer-reviewed journals. The organization of the subsequent chapters for this dissertation is as follows:

Chapter 2 presents the assessment of the physical properties of water-repellent soils. This chapter investigates the applicability of laboratory-made hydrophobic soils for studying mudflows by comparing them to natural hydrophobic soils collected from two burned sites that will help understand and predict post-wildfire soil erosion and mudflow mechanisms.

Chapter 3 presents the granularity role of water repellent sand particles on post-impact dynamics of water droplet. The investigation is performed within a context of post-wildfire rain-induced erosion on burned slopes. A comprehensive investigation of a relationship between single drop dynamics and wildfire-induced surface hydrophobicity is a basis for a forthcoming understanding of high rain-induced soil erosion rates.

Chapter 4 presents the effect of spatial variability and granularity of the water repellent layer on post-wildfire debris flow initiation mechanism. Three fine, medium and coarse sands with different layer configurations are tested under different rain intensities and slope gradients and in total results of 36 experiments are presented.

Chapter 5 presents the machine learning framework for post-wildfire mudflow onset classification. The machine learning technics used in this study such as multiple linear regression, k-means clustering, support vector machine and logistic regression methods aim to classify and synthesize the experimental results of chapter 4.

Chapter 6 summarizes conclusions of all chapters for this research.

2. Assessment of physical properties of water repellent soils

2.1 Introduction

2.1.1 Origins, formation, and properties of water repellent soils

During wildfires, accumulated organic matter such as plant root exudates, certain fungal species and surface wax from plant leaves decomposes and volatilizes into soil and induces soil water repellency, i.e., hydrophobicity, in shallow soil layers (1). A mechanism that underlies hydrophobicity is a weak attraction between the molecules of liquid water and solid due to low-energy soil grain surface created by the deposited organic matter (6). Change in micro-biological activities and their relation to soil moisture is considered responsible for the change in hydrophobicity severity (14–17). The loss of hydrophobicity with time in natural and fire-induced hydrophobic material is a complex coupled process. Decreased amount of organic soil carbon has been experimentally obtained several months after fire (18). In natural hydrophobic soils, decomposition of organic matter occurs from microorganisms or reduced microbial activity due to the loss of nutrients (19,20). Deposition of dust and atmospheric pollution (21) on hydrophobic and superhydrophobic surfaces attributes to the reduction of hydrophobicity. Hydrophobicity of surficial soil layers causes rain soil erosion, overland flow, rain-splash detachment and preferential flow paths in burned areas (5,8). Runoff-dominated processes have been widely reported in recently burned areas (9,11). Previous studies looked at the geographical patterns of the runoff and have shown that the grain size distribution, shape and characteristics of overland flow affect the erosion mechanism and sediment transport (22,23). The available literature for naturally hydrophobic soils has mostly focused on the data about the rainfall thresholds that trigger mudflows and landslides and not the mechanical properties of the soil of the burned area (24,25). Cannon et al. (2008) (24) developed an empirical relation for rain intensity-duration threshold for

7

occurrence of debris flows of naturally hydrophobic soils collected in California and Colorado. Tiwari et al. (2020) (12) studied the properties of debris flow soil from Montecito debris flow after Thomas fire in California. Vieira et al. (2015) (25) studied 109 records of wildfire and prescribed fire on soil erosion and post fire runoff. The study shows that fire occurrence is an important factor in erosive process of soil. However, the relevant soil properties, such as are the soil hydrophobicity levels and infiltration characteristics have not yet been extensively studied and related to runoff.

Mechanical properties of hydrophobic soils have been performed in a limited number of studies, which yielded consistent conclusions. Results from a ring shear test show that the residual shear strength of ash deposit was less than one-third of the residual shear strength of the soil matrix. Polymer-coated sand shear strength was recently investigated in triaxial tests, which proved the reduction in shear strength (26,27). Additional relevant studies of the mechanical properties of hydrophobic soils used glass beads and artificially made hydrophobic soils (28–30). Byun et al. (2012) (31) investigated the shear strength and stiffness of hydrophobized glass beads by doing direct shear test and shear velocity test and showed that the shear strength of hydrophobic sample is lower than the regular glass beads. Shear wave velocity remained constant in hydrophobic dry sample while it increased in hydrophilic sample due to increased interlock of particles during the shear test.

The relationship between the water content and the matric suction (ψ) is called the soil water retention curve (SWRC) and determines the hydraulic conductivity, drainage, solute movement, and suction distribution in soil (32,33), and can be fitted to the van Genuchten empirical model (34). Ahmad-Adli et al. (2014) (35) related rainfall infiltration processes into hydrophilic slopes to the air entry values, matrix suction and shear strength of soils in a numerical parametric study of slope stability problem. Liu et al. (2012) (36) studied the soil desorption curve

of three naturally hydrophilic and artificially hydrophobized soils. He concluded that SWRCs are divided into three domains with different wettability characteristics. The moisture-dependent wettability has no influence on water retention in the first and third domains, while significantly reducing the water retention capacity in the second domain. Bauters et al. (2000) (37) conducted infiltration and imbibing soil characteristic curve tests on different soil batches. The water infiltration tests are conducted for two naturally hydrophobic soils and for laboratory-made hydrophobic soil with different percentages of water repellency. The water retention curves are obtained for the mix of hydrophilic soil with no (0%), 3.1%, 5% and 9% by weight of added hydrophobic particles. The air entry value is lower for the water repellent soils and the reason could be due to infiltration patterns and the incomplete imbibed medium and hydrophobic finer pores. In 2010, Czachor et al. (29) investigated the water retention curves of a quartz model soil with different fractions of hydrophobized grains and field soils which contain organic matter. They indicated that the wetting branch of water retention curve is significantly affected with soil-pore water contact angle while the effects on the drying branch are minimal. Beckett et al. (2016) (28) have briefly introduced the hydrophobicity in the frame of unsaturated soils for geotechnical engineers and the microscopic and macroscopic scale effect of water repellency on unsaturated soil properties.

Dynamics of droplet shape and movement on surface can improve the understanding the mechanism of erosion and onset of mudflows. Surface energy and wettability are two factors that affect the behavior of water droplet on the surface (21). Soil minerals with higher density of charge and polar groups have a higher wettability and affinity for water (38). However, also smaller values of interfacial tension have been found for minerals in soil by Miyamoto (1971) (39). Wetting characteristics of soil demonstrate the spreading ability of water on the surface and can indicate

the interfacial forces between soil, liquid, and gas, which can be measured by soil water contact angle. Water contact angles are classified as ultra-hydrophilic (≈0º), hydrophilic (0º-90º), hydrophobic (90º-150º) and ultra-hydrophobic (>150º) (Chieng et al. 2019). In hydrophobic surfaces, the contact angle is low and thus the droplet tends to roll down and move easily (41). Water drop penetration time (WDPT) is time needed for the contact angle to decrease from non-wetting values to wetting values (42,43), which occurs when solid and liquid adhesive forces overcome the attraction forces among liquid molecules (44). Chemical composition of the hydrophobic coating, the degree of ordering and orientation of surface molecules affect the wettability (21). Organic compounds reorient and rearrange after they are in contact with water (45). Furthermore, an air gap is considered to act as a barrier beneath the surface layer due to the formation of a plate-shape clump of wet particles in the surface layer (44). The relationship between contact angle, water entry value, erosion and failure are such that higher contact angles, accompanied by positive water entry values in surficial soils prevent rainwater infiltration and enhance surface overflow. Water overflow, which increases with rain intensity, erodes the soil leading to debris flow. The failure of slopes with hydrophobic surface layer means removal of surficial soil by erosion processes. This study is motivated by a necessity of filling in the limited amount of available data of natural hydrophobic post-wildfire soil properties, which are difficult to collect and thus not frequently extensively studied. Soil water retention curves (SWRC) have not been, to our knowledge, performed on 100% hydrophobic soils, as well as wetting curves. Hydrophobic soils are considered non-wettable, and typically a positive pressure needs to be applied to the specimen for instantaneous water infiltration, which is what we obtained by measuring the water entry values. Measurements of the water drop penetration time, the contact angle, the direct shear strength, and smaller span of quasi-wetting SWRC measurements of the soil

water characteristics are conducted on hydrophobic and regular sands. Scanning Electron Microscope (SEM) and optical microscope images are taken from both samples to investigate the micro-properties of the hydrophobic soil. This note investigates the role of time delay for soil wetting and SWRC test, as well as the water entry value applicability to characterize hydrophobic soil behavior relevant to mudflow onset and its relationship to the water contact angle. Knowledge of soil characteristics will aid in better understanding the mechanisms of erosion and debris flow in hydrophobic soils, which has a potential to reduce life hazards and enhance early warning systems.

2.2 Materials and methodology

2.2.1 Collecting and preparing hydrophobic soil

In August 2018, the Holy Fire burned 23,000 acres of Cleveland National Forest in California. Hydrophobicity was reported by Burned Area Emergency Response (BAER) team in almost all burned areas with about 71% burned with moderate severity and chaparral dominated vegetation (46). The precipitation in the area ranges from 13 to 23 inch per year, with 78% of storms happening between October and April, including occasional summer thunderstorms. Geologically young and steep mountains in this area result in a higher risk of debris flow, rock fall and slumping, especially in the severely burned steep areas (46). We have collected hydrophobic soil samples directly from the area of Cleveland national forest in October 2018. A second batch of hydrophobic soil was collected in October 2020 from El Dorado fire site in southern California. After removing the ash layer from the soil surface, we performed water droplets beading assessment and tested in-situ hydrophobicity. Then, we carefully obtained soil samples from approximately 0-4 cm thick hydrophobic soil layers in a few locations, sealed them in airtight container and removed the remaining roots in the laboratory by sieving.

Ottawa F-65 sand, a rounded-particle soil, is another batch of tested soil that is processed to become artificially hydrophobic. After drying for 24 hours, the Ottawa F-65 sand is submerged in 10% by volume $V_{\text{n-octyltriethoxysilane}}$ /$V_{\text{isopropyl-alcohol}}$ solution for the next 48 hours and the sand is washed to remove any reactive compound and oven-dried for 24 hours (47–50). The Cleveland soil specimen was kept in an air-tight container which kept the initial moisture constant in laboratory in room conditions of 22° C for one year after collecting from the fire site. Hydrophobicity level is determined by WDPT for all soil samples. WDPT can be determined by placing 50 µL water droplets on the soil surface and measuring the time required for the complete penetration. The water repellency is categorized with the static water contact angle obtained from the sessile droplet method (51). A double-sided adhesive tape is fixed on a microscopic glass, and oven-dried soil is sprinkled on the 2 cm by 2 cm tape and tapped carefully to remove any excess soil. A 100-gr weight is used to press the soil particles to the tape, and the procedure is repeated two times for all the samples. Five drops of deionized water are placed on the soil layer by a pipette, where each drop's volume is 1.7 mm^3. A scientific Phantom Miro C320 camera images the droplet with high precision 640x480 pixels immediately and after 5 and 10 min.

2.2.2   Soil-water retention test

SWRCs are measured using the hanging column method according to the ASTM D6836-16 standard (52) for determining the wetting-path curve from dry specimens. It has been previously found that naturally formed hydrophobic soil from wildfire sites might lose the hydrophobicity once it reaches a critical water content (53). However, due to the laboratory chemical treatment, which is different from natural fire-induced combustion, the intensity of the artificially induced hydrophobicity does not change after soaking and re-drying. Testing of Cleveland soil proved a complete loss its hydrophobicity after it was wetted once, unlike the artificial soil. We attribute

this difference to the different persistencies of two different coatings of soil surfaces to become hydrophobic. SRWC was measured on a dry soil sample residing in the retaining ring with filter-paper bottom, which is twisted for 45º when putting into a glass funnel to ensure the contact between the sample and a saturated (for 24h) porous plate. A thin plastic film covers the funnel to avoid evaporation. Lowering the funnel from the balance point applies various suctions to the specimen, while entered or expelled water level is measured by a capillary tube. Water elevation is recorded in each step and water retention curves are obtained.

2.2.3   Water entry test

The water entry value, which corresponds to the positive pressure of a column of water on top of the hydrophobic soil that is needed for instantaneous infiltration, is measured for hydrophobic samples by using the water-ponding method shown in the test procedure in a study by (53). A 4-cm diameter transparent tube is sprayed with water repellent solution. The bottom 5 cm of the tube is filled with the soil sample. The soil sample is placed on a porous plate to avoid air entrapment. Water is carefully poured and ponded on the soil sample by using a syringe to avoid soil surface disruption. The ponding height at which water starts to infiltrate the soil is the water entry value.

2.2.4   Direct shear test

Direct shear tests are conducted on dry specimens subjected to three different vertical stresses of σ_1=83 kPa, σ_2=134 kPa, and σ_3=180 kPa in displacement-control mode with a shearing rate of 0.5 mm/min. All specimens are tamped in three identical dry layers in a 63.5x63.5 mm square-shaped box and sheared to failure.

2.2.5   Scanning electron microscope

To obtain Scanning Electron Microscope (SEM) images of the site soil and treated and untreated sand, the soil sample is coated in a sputter coater device (Emitech K575X) with iridium to provide a conductive surface to scan the sample, and images are taken (FEI Quanta FEG 250 device). In addition to SEM images, energy-dispersive X-ray microanalysis (EDX) is conducted for each sample to map chemical element distribution and characterize constitutive soil minerals present in the sample.

2.3   Results

Soil particle distribution for soils used in this study is shown in Figure 2.1. The coefficient of uniformity and curvature are 4.7 and 0.8, respectively for Cleveland soil, which is classified as poorly graded sand (SP). The grain distribution of Ottawa F-65 indicates that the sand is also SP, with a coefficient of uniformity and curvature of 1.61 and 0.96. WDPT test results show that the sample taken from Cleveland national forest and the hydrophobic Ottawa F-65 sand are strongly and severely hydrophobic, respectively (Table 2.1). The WDPT for the recently collected soil from El Dorado fire (2020) site in San Bernardino, California, shows that the soil is extremely water repellent, with an infiltration time of over 10 minutes.
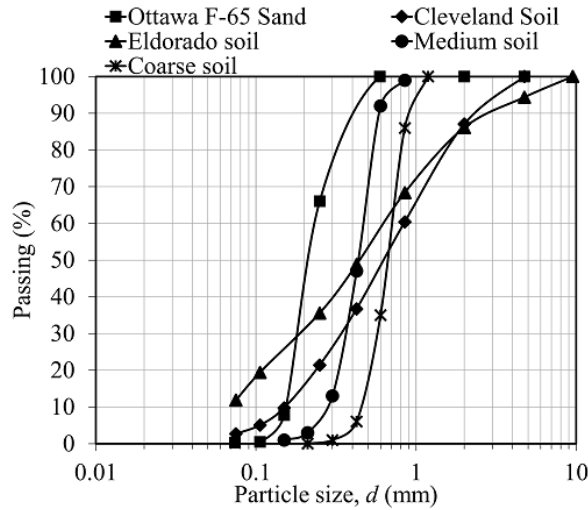
Figure 2.1 Grain size distribution of Cleveland hydrophobic soil and Ottawa F-65 Sand

Table 2.1 Water drop penetration time test results

Soil	WDPT	Classification
Ottawa F-65 regular	5 s	Wettable
Cleveland (1 year)	20 s	Moderately hydrophobic
Cleveland	100 s	Strongly hydrophobic
El Dorado fire site (San Bernardino)	720 s	Severely hydrophobic
Ottawa F-65 hydrophobic	3600 s	Severely hydrophobic

The water repellency stability and severity for the specimens are measured by the water drop penetration time (WDPT) and contact angle tests. At first, the Cleveland soil was classified strongly hydrophobic based on WDPT test with the contact angle of 100°. After one year the WDPT indicated that the soil became more wettable, and the contact angle reduced to 88°. The El Dorado fire soil contact angle is 109°. Investigation of the hydrophobicity loss in natural soil is outside of the scope of this note and would require chemical analysis. The water drop contact angle of both hydrophobic and regular Ottawa F-65 sand is measured using sessile drop method (Figure 2.2). The photos of the drop are taken immediately after the drop was placed and after 10 s, 1 min and 10 min. The images show that the initial contact angle in hydrophobic sample is 115° and 61°

15

in regular sample, the angle has changed over time in both samples, but the rate of change in regular sample is more significant than in hydrophobic.

| (a) | (b) | (c) |
| (d) | (e) | (f) |
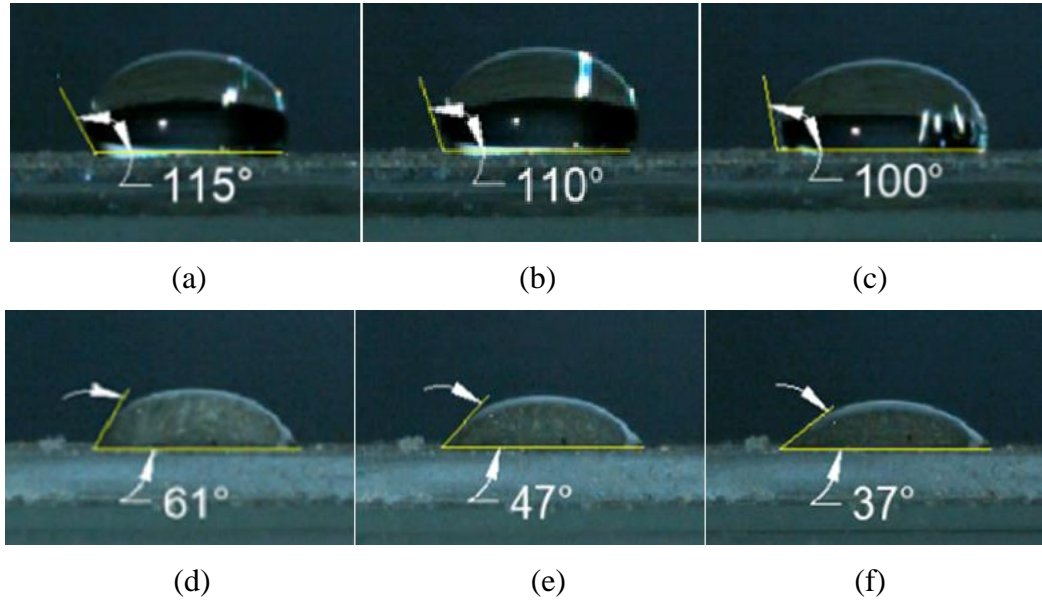
Figure 2.2 Contact angle θ measurements in (a–c) hydrophobic and (d–f) regular sand; (a and d) immediately after placing drop; (b and e) after 5 min; and (c and f) after 10 min.

The SWRCs for the Cleveland, Ottawa F-65 regular and hydrophobic sand are shown in Figure 2.3 in terms of the volumetric water content and the degree of saturation. Although SWRC for regular Ottawa F-65 sand was measured using standard procedures, in cases of hydrophobic soil that was not possible. Independently fitted parameters, namely α and N, in van Genuchten SWRC equation (Eq. 2.1) are shown for all materials in Figure 2.3 (Van Genuchten 1980):

$$\Theta(\psi) = \Theta_r + \frac{\Theta_s - \Theta_r}{[1 + (\alpha|\psi|)^N]^{1-\frac{1}{N}}} \qquad (2.1)$$

where $\Theta(\psi)$ is the water retention curve, $|\psi|$ is the suction pressure, Θ_s is the saturated water content, Θ_r is the residual water content, α and N are the shape parameter of the curve and the measure of the pore size distribution. The results of hydrophobic and regular Ottawa F-65 sand

16

indicate that the final volumetric water content of hydrophobic soil has reduced about four times. The final water content of Cleveland and Ottawa F-65 hydrophobic specimens is about 7.4% and 4.7%, respectively when reaching zero suction. The Cleveland soil is also retested after one year. Water retention curve of the Cleveland soil after one year shows that the water content at zero suction has increased from 7.4 to 19%. A long waiting time up to several hours was needed for the test to react, which is somewhat inconsistent with values in Table 2.1. The SWRC results clearly indicate and confirm that hydrophobic soils resist water infiltration and absorb less water than regular soil during rainfall event, developing various and unpredictable time-dependability behavior of the hydrophobic soil, which has been explained in the literature as infiltration instability and imbibition problem. Therefore, SWRC results for hydrophobic soils are only indicative, but they cannot be used for any slope stability assessment due to a longer undefined waiting time. Lower water content and the reduction of stored water were recorded in hydrophobic soil compared to regular soil. Results indicate a decrease in mobility of water through pores between dry non-wettable grain surfaces initially filled with air.
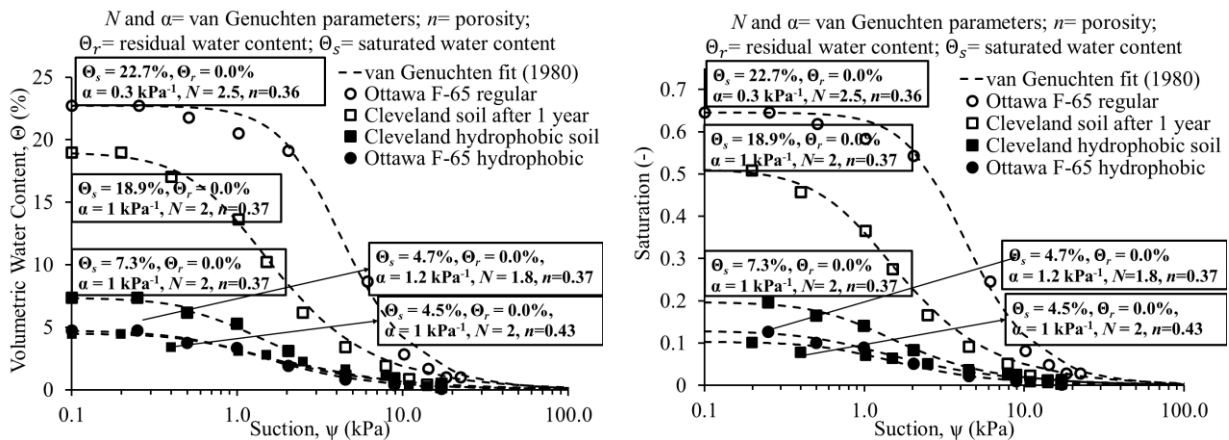
Figure 2.3 Wetting curves from SWRC test in terms of (a) volumetric water content; and (b) saturation for Cleveland and Ottawa hydrophobic and regular soil, where n is porosity, Θs and Θr are saturated and residual values of soil water content, respectively, and α and N are van Genuchten parameters.

The water entry tests are performed for four soil types with three different dry densities. Four soils used in these tests are artificially hydrophobic Ottawa sand, medium grain soil, coarse grain soil and two naturally hydrophobic sands, Cleveland soil after approximately 14 months after the fire and new soil 2 months after the fire from Eldorado fire in San Bernardino, California. Additionally, the results are compared with the results of Organo-silane treated Ottawa sand from Keatts et al. (2018) (54) and Oddrop soil in Netherlands from Wang et al. (2000) (53). Figure 2.4 shows the test results for water entry values of the above-mentioned soil samples versus the contact angle, the median diameter value of the particle size distribution (D_{50}) and the dry density. Results from the water entry level test show that all hydrophobic samples have a positive water entry value, and this value increases in samples with larger contact angles (Figure 2.4 (a)). While the contact angle of Cleveland hydrophobic soil decreased to 88° after one year, it still has a positive water entry value of 0.098 kPa. The results of the contact angle versus the water entry value demonstrate a linear relationship. The results of the water entry value versus D_{50} show that the finer the soil, the higher the water entry value is (Figure 2.4 (b)). Since the water entry value increase leads to larger inhibition of infiltration, more water can flow over the sloped soil surface, causing erosion. The D_{50} results indicate that a higher rate of erosion in post-fire areas is expected with finer soil compared to coarser areas. The dry density of soil moderately affects the water entry values. Although, generally, the samples with higher dry density require a taller water column to initiate the infiltration (Figure 2.4 (c)), the dependence of the water entry value on the dry density of Cleveland soil after one year is small. The results from three layers of Oddrop soil from Netherlands (53) are also added in Figure 2.4 (c). Results show that the severity of hydrophobicity and the median diameter value of the particle size distribution play an important role in water entry values.
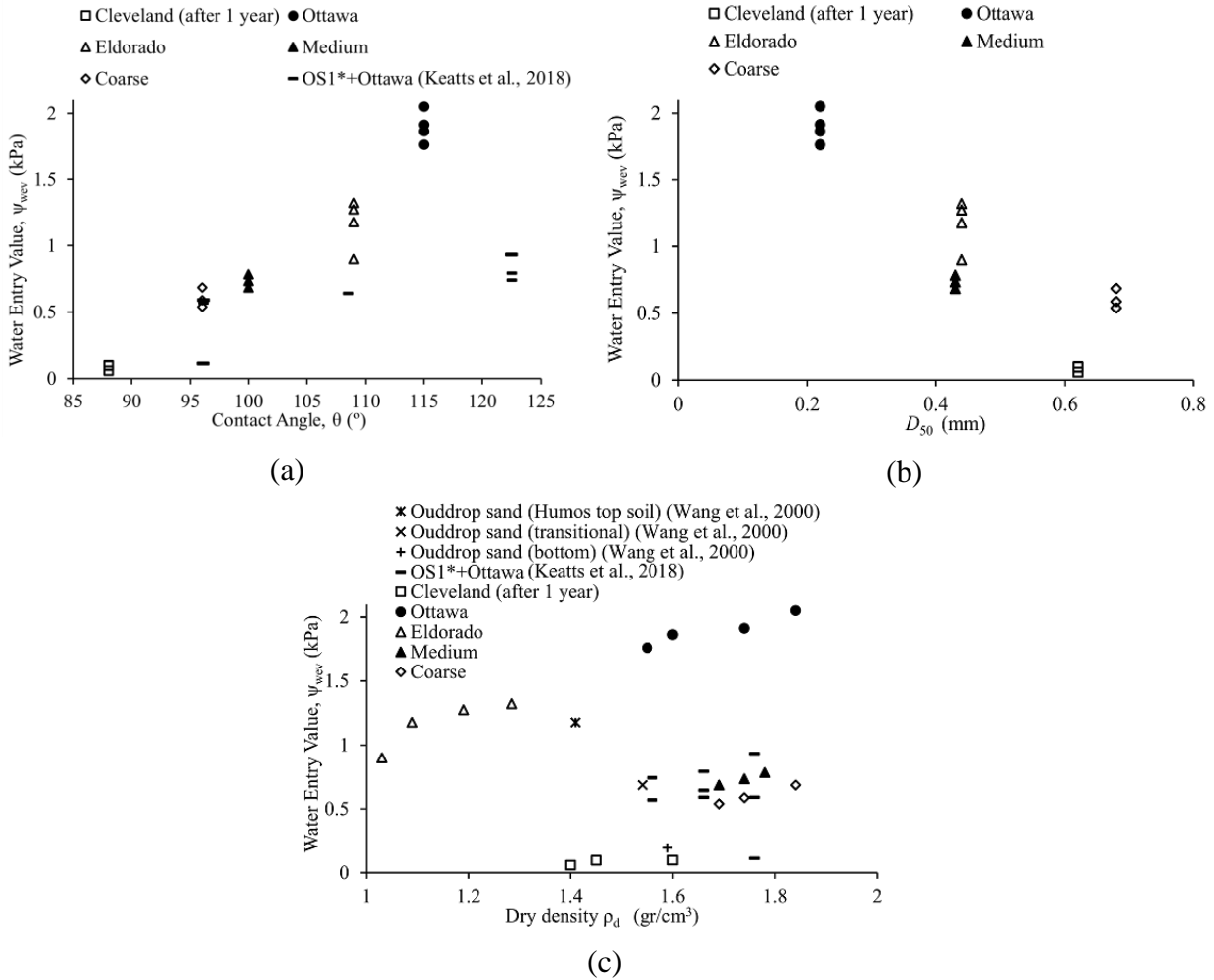
Figure 2.4 Water entry value versus: (a) contact angle θ; (b) D_{50}; and (c) dry density, OS1*= organosilane-treated soil for hydrophobicity.

Direct shear tests have been performed on dry specimens for general material characterization, also to compare to previous studies that showed that dry hydrophobic specimens have lower shear strength even before the rain (47,55). Furthermore, the infiltration rate in hydrophobic soil is negligible and our previous rainfall experiments (56) on a hydrophobic slope have shown that the water mostly flows on the hydrophobic slope instead of infiltrating it, or saturates a thin wettable soil layer above the hydrophobic soil causing infinite slope failure via dry hydrophobic layer. In addition, it is shown that if water ponds on a hydrophobic surface for a long time, the infiltration happens in fingering pattern and develops as fingers in a soil layer (57,58).

Results of Cleveland hydrophobic soil at a shearing rate of 0.5 mm/min and a unit weight of 15.5 kN/m^3, show a friction angle of 39°. Dry Ottawa F-65 regular and hydrophobic sand direct shear tests indicate that the friction angle decreases after the soil becomes hydrophobic. Both samples are tamped in three-layer and with a unit weight of 17.5 kN/m^3. The friction angle for Ottawa F-65 sand is 37° while it drops to 30° in hydrophobic Ottawa F-65 sand (Figure 2.5). Similar trend is shown from direct shear test results of previous studies by Byun and Lee (2012), Karim et al. (2018) and Kim et al. (2013) (47,55,59). However in a study by Tatar (2018) (60) no significant change was observed during consolidated undrained triaxial testing of the hydrophobic soil, where the reduction in effective stress-based shear strength parameter is believed to be compensated by an increase in the dilatancy. We show that the modification of the soil grain surface which leads to hydrophobicity already changes the internal friction angle of the soil in dry state, which is shown in Figure 2.5 for artificially induced hydrophobicity. We did not sample the site soil before the wildfire; therefore, we are missing information on the natural Cleveland soil. Nevertheless, it is shown that the surface modifications have been identified in SEM images as flakes on the grain surface, which provide a qualitative microstructural explanation of the variation in shear strength on dry specimens and the hydrophobicity of those samples.
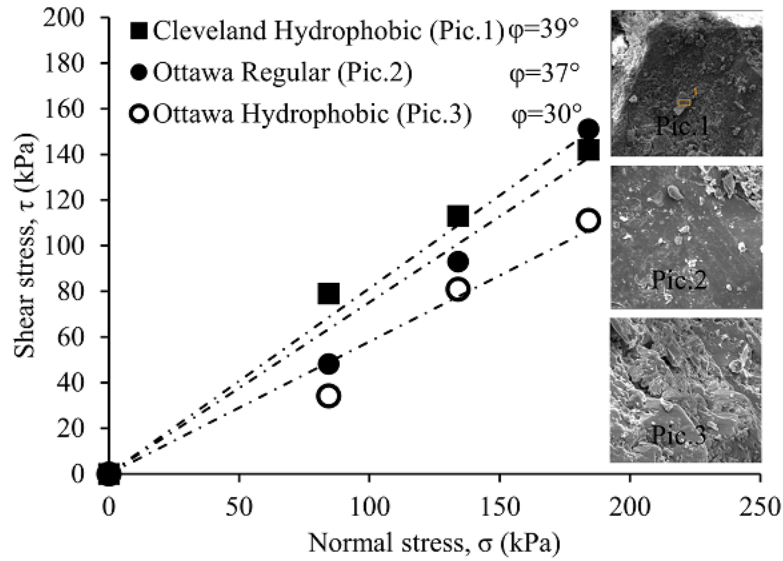
Figure 2.5 Direct shear test results

The addition of flakes on the grain surface, which have different chemical composition than silica and contain carbon (C^{4-}), thus organic matter, change the dry internal friction angle of the granular assembly. The investigation of the extent and origin of this behavior is outside of the scope of this study, but we could speculate here that the surfaces may in fact become more "slippery", or repellent to silica like to water, since both silica and water are polar molecules. Recently, surface modifications of sand coated with polymers revealed decreased fracture roughness compared to the untreated sands, which would lead to a decrease in shear strength (61). Scanning electron microscopic image and EDX analysis are shown in Figure 2.6 (a) and (b). The soil particles have angular shapes, and their surface area is covered with minuscule flakes. Oxygen (O), Silicon (Si) and Aluminum (Al) constitute 55%, 18% and 10% of the atomic weight of the soil sample. Iron, Potassium, Magnesium, Titanium and Sodium are the other minor minerals found in the soil sample. Iridium is found in the soil since the sample was Iridium-coated. The minerals in soil indicate that the geological structure of the area can consist of quartz and alkali feldspars.
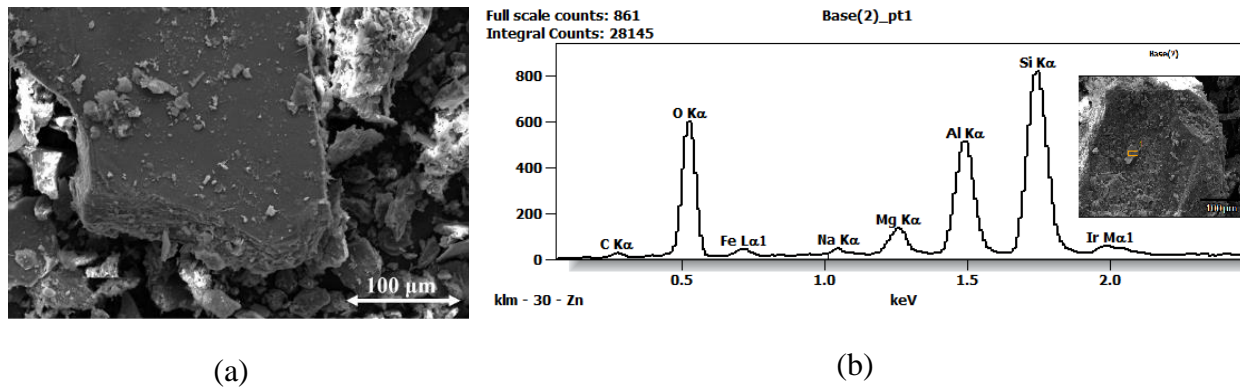
Figure 2.6 (a) SEM image of Cleveland hydrophobic soil with a magnification of 100 μm, (b) EDX analysis

Figure 2.7 (a) and (b) show regular and hydrophobic Ottawa F-65 sand. The soil grains have a rounded shape, and the regular sand surface is smoother than the hydrophobic sand surface. The hydrophobic sand surface has more irregularities and is coated with a thin layer of flakes in some parts. EDX analysis (Figure 2.8) shows that most of the chemical composition of the soil is mainly Oxygen (O) and Silicone (Si) with an increased amount of Oxygen in the hydrophobic sample due to the n-octyltriethoxysilane ($C_{14}H_{32}O_3Si$) coating.

Based on the results from the contact angle test and WDPT, we believe that laboratory-made hydrophobicity is more persistent over time because most of the soil grains are coated with the hydrophobic agent, while in natural soil this is not the case and only some particles have become hydrophobic. In addition, the results from EDX analysis show that the natural hydrophobic soil contains more minerals than the laboratory-made hydrophobic soil. It can be assumed that the natural hydrophobic coating fades away after a period, while the chemical solution used in laboratory-made hydrophobic soil lasts longer. We have concluded that the artificially hydrophobic soil can be substantiated if the aim is to study the hydrophobic soil right after the fire.

However, the natural hydrophobic soil loses hydrophobicity, and its behavior changes over time while the artificial hydrophobic soil stays the same.

(a)

(b)
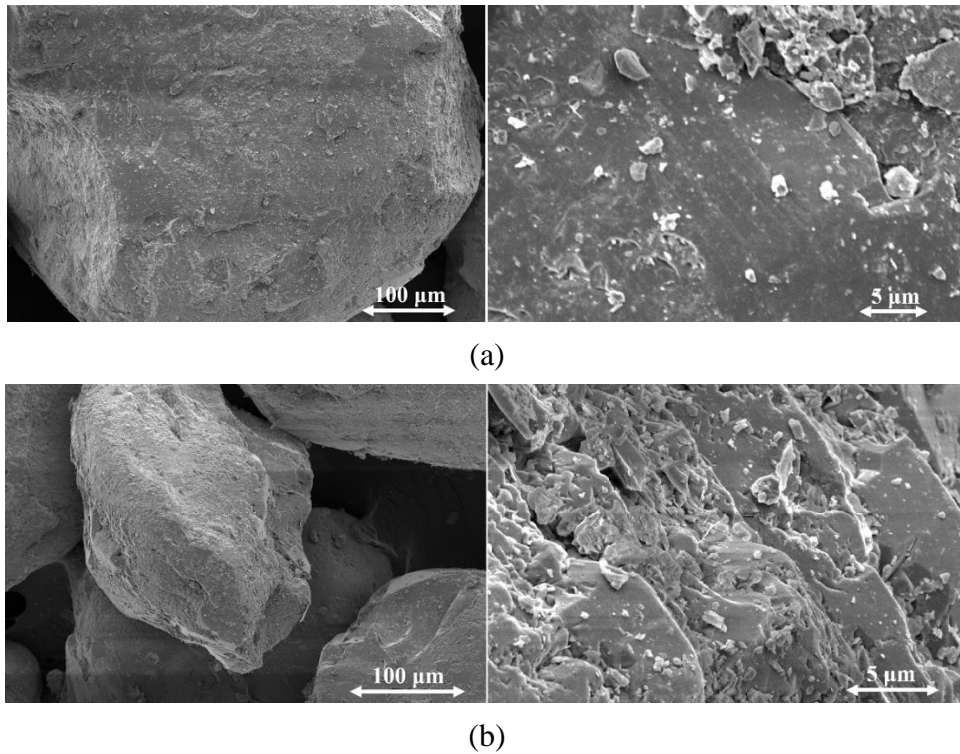
Figure 2.7 SEM images of (a) Ottawa F-65 regular and (b) Ottawa F-65 hydrophobic sand with magnification of 100 μm and 5 μm (from left to right)

(a)

(b)
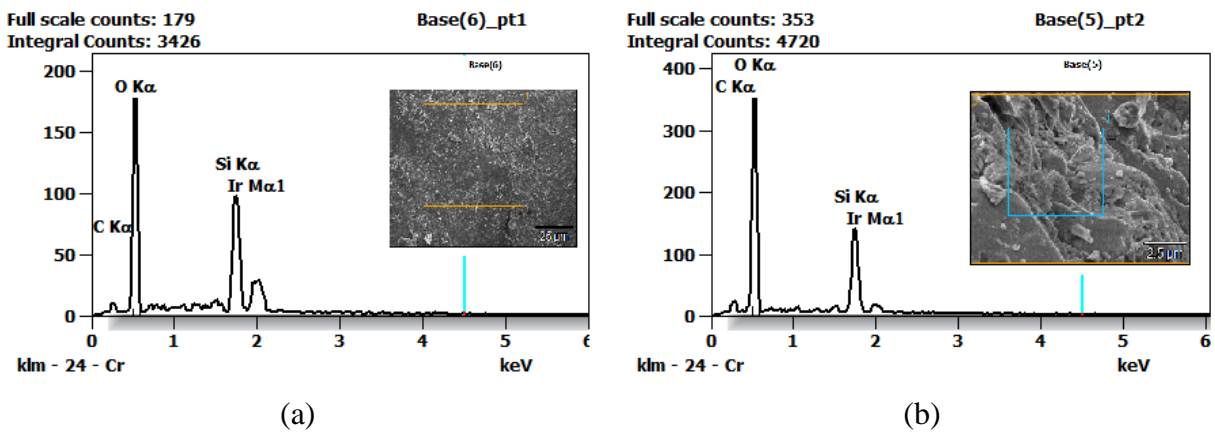
Figure 2.8 EDX analysis of (a) Ottawa F-65 regular (b) Ottawa F-65 hydrophobic sand

2.4   Conclusions

Hydrophobicity has a significant effect on the hydraulic and physical characteristics of soil. Conversion of surficial soil particle characteristics will lead to a change in soil behavior, which is critical during rainfall and flood in slopes. It is known that the post-wildfire soil properties do vary across the soil types and depend on the hydrophobicity level induced by different fire types and fuels. We report here comprehensive physical and mechanical properties of Cleveland soil after fire, which is typical for the given area and the fire that occurred and has to our knowledge, not yet been reported. We also evaluated the water entry values and contact angle of different batches of soil, including the soil collected from the newly burned Sen Bernardino area impacted by El Dorado fire. Additionally, we evaluate to what extent we can match artificially produced hydrophobic soil in the laboratory, which is necessary for further experiments on erosion and mudflow mechanisms. Furthermore, collecting homogeneous batches of post-wildfire hydrophobic soil for purposes of extensive laboratory experiments in large amounts is nearly impossible. Therefore, the comparison is important for evaluating how hydrophobicity affects mechanical properties.

Novel aspects of our study include water penetration test correlations with dry soil density, soil type, $D_{50,}$ and the drop contact angle. Natural soil properties vary by location, so this note adds in valuable data from two different sites in California. We also believe that comparing soil immediately after the fire and one year after with decreased natural hydrophobicity provides novel insights and can help in finding temporary precautions for the effective period of these types of soils. Cleveland soil, after one year, shows reduction in hydrophobicity, contact angle and time-delayed SRWC increase in water content from 7%. to 19%. The reason for the reduction of hydrophobicity can be due to the loss of soil organic carbon over time. Water contact angle results

reveal the larger contact angle for Ottawa F-65 hydrophobic sample, with the reduction of angle during time is less significant for the hydrophobic sample.

The water ponding test indicates that the water entry potential values for the hydrophobic samples are positive. The positive values for water entry in hydrophobic samples lead to the conclusion that the instantaneous wetting curve of SWRC should have a zero value of volumetric water content in negative suctions. However, the SWRC of hydrophobic samples shows a small amount of water gained by the samples in negative suction, which can be attributed to the long waiting time of the test. SWRC can be unreliable for assessing hydraulic properties of burned soils on slopes impacted by rain, because suction develops with significant time delay or is absent. Flash floods on inclined hydrophobic soil surfaces occur rapidly during rainfall, and the overflow water does not pond on slopes. The water entry values for the different tested soils indicate a linear relationship between the contact angle and water entry values. It is also concluded that the median diameter value of the particle size distribution can be a good parameter in predicting the water entry values. Increasing the dry density of soil also affects the water entry values but its influence is not as significant as the contact angle and D_{50} values.

To evaluate mechanical parameters, the direct shear test is used for two reasons: firstly, we wanted to evaluate only the friction angle of different soils, assuming that the principal stress rotation would not affect the results significantly, and secondly, we aimed to compare results with earlier studies (47,55,59,60). The direct shear test results for laboratory-made hydrophobic sand demonstrated a decrease in friction angle from 37º in normal sand to 30º for the hydrophobic sample, which causes a reduction of shear strength in the hydrophobic sample and will therefore increase the risk of failure in hydrophobic slopes. Soil samples SEM images show that there are

more flakes and dots on the hydrophobic samples. It is concluded that these flakes can be responsible for the reduction of dry friction angle of soil and in fact, can form a "slippery" surface.

SEM images illustrate a smoother surface for regular surface, while the hydrophobic sample has more irregularities on surface and a thin layer of flakes cover the surface. EDX analysis for each soil displayed that the Cleveland soil contained more minerals. However, the laboratory-made hydrophobic Ottawa F-65 sand was mainly consisted of Silica and Oxygen with higher amount of Oxygen in hydrophobic sample. Over a year, natural hydrophobic soil has shown progressively less resistance to water infiltration and the contact angle reduction, while the laboratory-made hydrophobic soil properties change was negligible. Laboratory-made hydrophobic soil is a common alternative to natural post-wildfire hydrophobic soil behavior testing, and we have confirmed that artificially hydrophobic soil can be used if the aim is to study the hydrophobic soil right after the fire.

Data Availability Statement

All data, models, and code generated or used during the study appear in the submitted article.

Acknowledgment

3. Role of hydrophobic sand particles granularity on water droplet post-impact dynamics

3.1 Introduction

3.1.1 Drop impact dynamics and governing relations

This chapter investigates the drop impact and post-impact behavior on granular hydrophobic and hydrophilic sand to better understand the onset of rain-induced post-wildfire mudflows. Particle hydrophobicity enhances the rate of sand erosion leading to mudflows (1,8,62), splash detachment and increased water overflow (1,2,5). A thin surficial layer turns hydrophobic during the combustion of pre-existing organic matter in soil, predominately affecting non-cohesive sandy soils. As a result, the surface hydrophobicity lowers the grain surface energy and weakens the attraction between liquid and solid (6). Although it is known that erosion depends on the sand particle mobility, what remains unclear is a preceding modification of a raindrop impact on a hydrophobic sand surface.

Generally, hydrophobic surface water-drop performance results from mechanical and physical water and solid properties, impact velocity, surface roughness and tension, wettability, interfacial tension, and trapped air (63). Drop impact dynamics manifest as rebounding, pinning, and fragmentation (64). For example, Rioboo et al. (65) identified that drop impact on a dry substrate could lead to six different scenarios: deposition, prompt splash, corona splash, receding break-up, partial rebound, and complete rebound. Rioboo et al. (65) divided the drop's spreading curve between kinematic, spreading, relaxation, equilibrium, and wettability stages. The kinematic phase is insensitive to physical drop properties, while surface parameters affect drop spreading. During the final wettability phase, when the surface hydrophobicity strongly influences the spreading, the drop recedes and sometimes breaks up. Several empirical models estimate the

27

maximum drop spread diameter using the energy balance(66,67) and the momentum balance (68,69).

Drop spread empirical scaling models consider different surface deformability and liquid properties. For example, Clanet et al. (70) scaled the maximum spread diameter normalized by the drop diameter to be $\beta_{\max} = We^{1/4}$ on a solid superhydrophobic surface. Additional contributions consider the drop impact on dry substrates with varying wetting characteristics (71–77). Lee et al. (78) suggested that the nature of the substrate has a negligible effect on the spreading and introduced the capillary energy at zero velocity. Wildeman et al. (74) compared the drop impact on slippery or lubricated vs. no-slip solid surfaces, and Tang et al. (79) incorporated the surface roughness effect in an empirical model. The results from post-impact dynamics on glass beads and spherical surfaces showed that higher drop velocity leads to more splashing on the granular medium than on a smooth surface (80), with increased susceptibility to splash erosion in hydrophobic surfaces (81). In addition, the maximum drop spread diameter increases at higher impact velocities, lower wettability, lower surface tension, and larger drop diameters (82). On a horizontal deformable bed of grains, effects of packing fraction and deformability (83), wettability (83,84), liquid property (80), fluid grain mixing (85), and temperature (86) are studied, and several scaling laws are obtained for crater morphology. On a horizontal deformable bed of hydrophilic bed, a scaling law of $\beta_{\max} \propto We^{\frac{1}{4}}$ is identified by several researchers (80,85,87,88). Nefzaoui and Skurtys (80) suggested $\beta_{\max} \propto We^{\frac{1}{4}}$ for liquid with low surface tension and $\beta_{\max} \propto We^{\frac{1}{5}}$ for drops with higher surface tension. Zhao et al. (84) implemented the effect of deformability by multiplying the term $\frac{D_0}{D_0 + Z_c}$ to We, where D_0 and Z_c are drop diameter and maximum crater depth, and obtained an effective We^* number. The effective Re^* number is obtained by using the effective

viscosity $\vartheta_p = 2kp(1-\varphi)/\mu_l$, where the permeability k, p pressure and μ_l dynamic viscosity

and φ packing fraction are involved (83). A scaling law of $\beta_{\max} \propto We^{*\frac{1}{10}} \propto Re^{*\frac{1}{5}}$ for large

hydrophilic grains and $\beta_{max} \propto We^{*\frac{1}{4}}$ for small hydrophilic grains was obtained. Zhao et al. also

mentioned that the scaling law for deformable bed of hydrophobic grains is $\beta_{max} \propto We^{*\frac{1}{4}}$ and

grain size does not affect the D_{max} in hydrophobic grains, however a transitional behavior from

capillary to viscous regime for hydrophilic tests was found. A scale of $\beta_{max} \propto We^{\frac{1}{3}}$ is found for

deformable bed of hydrophobic glass beads (85) and Poly(tetrafluoroethylene) (PTFE) particles

(89). Supakar et al. (85) implemented an effective surface tension due to the adhesion of

hydrophobic particles to the liquid drop and formation of liquid marbles with multiphase surface.

Furthermore, micro and nano roughness and micropillars (90–92) yield different drop

impact behaviors. Fakir-state stability occurs, and drops behave similarly to each other that

ultimately bounce, partially re-bounce, trap an air bubble, jet, stick, or vibrate at low We (90).

During an impact at intermediate velocity on an artificially rough micro- and nano-

superhydrophobic surfaces, a drop penetrates, then partially pins, and rebounds (92). On a smaller

scale, rough surfaces lead to Wenzel or Cassie-Baxter wettability models (93,94). For the Wenzel

model, a liquid droplet fills in surface grooves, while in the Cassie-Baxter model, the air is

entrapped between the solid surface and the liquid drop as a barrier. Although the Cassie-Baxter

model dominates hydrophobic sands, Wenzel or a transition between Wenzel and Cassie-Baxter

can also occur (95). A reformulated contact angle model for soil and a range of liquid surface

tensions, proposed by Bachmann and McHale, combines Cassie-Baxter and Wenzel's equation

using a new roughness factor that depends on Young's law (96). The empirical relations for the

studies mentioned above are presented later and compared to our experimental data.

Some researchers conducted drop deformation and crater formation studies on natural deformable sand samples. Lardier et al. (97) investigated the drop impact on two deformable beds of pure silica sand and loamy topsoil sand. They concluded that soil grain distribution and roughness control the variation in experimental results. The soil with broader variation in grain size and rougher surface shows a more anisotropic spread and more variation in results. The data are best fitted with an exponent of 0.22 for impact energy (E) to a cratering model for final crater rim diameter, $Dc \propto (\rho g)^{-0.17} D^{0.32} E^{0.17}$, proposed by Holsapple (98) and later modified in (84). Jong and Zhao (99) suggested that variation in the reported scaling laws can be related to overlooking the energy consumption for the drop deformation. The impact energy transferred to the cratering phase depends on the layer compressibility on a deformable natural soil bed with various granular packings, according to Wyser et al. (100).

The drop post-impact behavior on an inclined or oblique surface is relevant to post-wildfire rain-induced mudflows on natural slopes and hills. Drop hitting inclined, pre-fabricated hydrophobic, and superhydrophobic solid surfaces have been studied previously (101–105). Although the results have revealed that drop behaves similarly in lower *We* in oblique and normal surfaces, at higher *We*, impact results diverge due to spread asymmetry and complexity (106). The drop post-impacts on inclined superhydrophobic and hydrophobic solid surfaces are deposition, rivulet, sliding, rolling, partial rebound, and rebound (104). A critical *We* for the transition between deposition and rebound of a water drop on smooth and rough, dry glass surfaces is suggested by Sikalo et al. (101). Leclear et al. (103) indicated that the normal-to-surface drop velocity component is causing the wetting transition. Aboud and Kietzig (102) showed that a solid hydrophobic surface of Polytetrafluoroethylene has a lower splashing threshold than the hydrophilic surface at comparable roughnesses. A stretched rebound drop is the drop that rebounds

while outstretched in an elongated pancake shape. Studies of solid impactors on deformable beds of granular material have revealed that the surface inclination affects the scale of crater diameter.

On the contrary, a shallower and more elongated crater forms on steeper surfaces (107). The mobility of sand grains in a deformable bed of sand can result in a shear band under external driving that can affect the drop behavior (83). In addition, rolling a liquid drop on a powder consisting of hydrophobic particles results in particle adhesion onto the droplet surface and the formation of liquid marbles (particle-covered spherical drops) due to interfacial energy minimization (108). Therefore, the behavior of such a multiphase surface should be more complex than a pure liquid drop. Different concepts can serve such studies as effective surface tension (γ_{eff}) (109).

This study uses a fixed grain sand surface to remove the effect of sand bed mobility and deformability and liquid-sand mixing complexity. Despite previous studies on a drop impact on various industrial or natural hydrophobic rough or granular surfaces, there is a gap in the literature regarding specific sandy soil surfaces characterized by particle sizes and geotechnical parameters and found on natural slopes impacted by wildfires. Therefore, this study focuses on fine, medium, and coarse sands and investigates how the drop size, drop-free-fall impact velocity, sand surface roughness, or grain sizes, and hydrophobicity affect raindrop impact behavior before it leads to sand erosion. In addition, this study focuses on the grain size and surface roughness relationships to maximum drop spread. Furthermore, the reviewed literature shows a gap in the droplet post-impact on inclined hydrophobic soil samples, which this study aims to address.

3.2　Materials and methods

The experimental setup uses a firm surface covered with fixed-in-place fine, medium, and coarse sand grains. Poorly graded fine sand is rounded-particle Ottawa F-65 silica, the medium and coarse are sub-angular pure silica with the predominant size range of 20-50 and 12-30 U.S. sieve sizes, respectively. Sand chemical composition is SiO_2, Al_2O_3, CaO, and Fe_2O_3. Figure 3.1 show the grain size distribution curves and parameters, static contact angles, and images of prepared sand surfaces. The soil surface roughness (S_q) is measured using white light interferometric (WLI) technology with Filmetrics Profilm3D Optical Profiler, located in the Nano3 lab at the University of California, San Diego. Before scanning, sand samples are coated with iridium in a sputter coater device (Emitech K575X) to provide a conductive surface. Then, the samples are placed in the Profilm 3D device, and a 10x objective scans the samples. The scans are processed with Profilm Online software. The invalid points are interpolated from neighbor pixels, and the outlying data points with slopes larger than 70 % are removed from the surface by comparing them against the nearest neighboring points. Finally, a Gaussian spatial filter reduces the noise and smoothens the scan. The root mean square of the surface roughness (S_q) (Eq. 3.1) is obtained by squaring the profile height (Z) deviations and taking the square root of the mean of these values recorded within the evaluation length, measured from the mean line, where M_c is the number of columns, M_r is the number of rows in the surface, and x_{si}, y_{sj} are the sampling point coordinates.The scans are shown in Figure 3.1 (b) for fine, medium, and coarse sands, and the roughness values are reported in Table 3.1.

$$S_q = \sqrt{\frac{1}{M_c M_r} \sum_{j=1}^{M_r} \sum_{i=1}^{M_c} Z^2(x_{si}, y_{si})} \qquad\qquad (3.1)$$
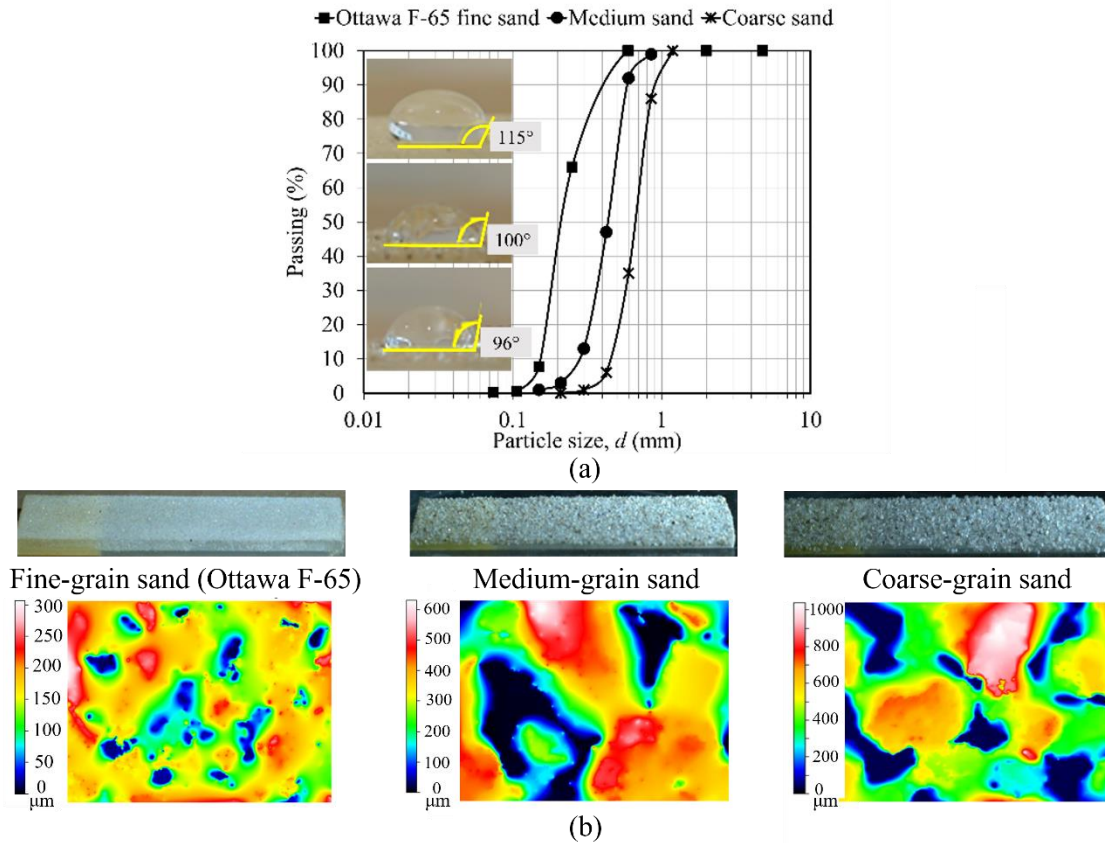
Figure 3.1 (a) Grain size distribution (b) prepared surfaces and surface topographical scans of fine, medium, and coarse sand using Filmetrics Profilm3D Optical Profiler.

Artificial hydrophobic sand is prepared in the laboratory for fine, medium and coarse sands. The contact angles (Table 3.1) are measured using the sessile drop method by placing a 10μl water drop with a microsyringe on the soil-coated slides and reading the contact angle at the three-phase boundary line. The measurements are repeated three times for each soil (110).

The Phantom Miro C320 high-speed scientific camera records videos at 1500 fps and 1280 x 1024 pixels. A single drop impacts horizontal and tilted surfaces from up to 180 cm height covered with sand at δ=30°, 40°, and 45°. Experiments use an automatic dropper with custom drop diameter modifications (Figure 3.2 (a)). The valve's opening duration controls the drop size. The accuracy of the dropper is examined for several drop sizes by measuring the drop diameters

in recorded high-speed videos and measured as ± 0.3 mm. Video footage and image analyses yield the impact velocity, drop diameter, maximum spread diameter, and contact angles.

Table 3.1 Soil contact angle and particle grading parameters.

Soil	Contact angle θ (°)		C_u	C_c	D_{10} (mm)	D_{50} (mm)	D_{60} (mm)	Roughness (Sq) (μm)
	Hydrophilic	Hydrophobic						
Fine	61	115	1.50	0.90	0.15	0.2	0.23	54.7
Medium	38	100	1.67	1.01	0.28	0.4	0.47	155
Coarse	27	96	1.53	1.03	0.46	0.65	0.70	250

Accuracy of the dropper, video capture, and system analysis are verified with theoretical predictions for a drop-free fall and compared to van Boxel's model (111). In van Boxel's model, two factors of shape distortion ($C_{def} = 1.5$) and turbulence inflow around the drop ($C_t = 23$) are included in the terminal velocity equation derived from the balanced equation between aerodynamic drag buoyant and gravitational forces. Turbulence development in the flow around the drop is incorporated by making friction a function of the particle Re, and distortion of the raindrop is expressed in terms of We. Another factor related to turbulence is C_τ, which is about 0.75 when the flow around the drop is fully turbulent (drop diameter > 0.3 mm) and increases by increasing diameter. By integrating Eq. 3.3 with respect to time (t), we see that the drop reaches 95% of its terminal velocity at the falling distance $H(t)$ (Eq. 3.5).

$$v_t . C_{def} . C_t = \frac{D_0^2 g(\rho_w - \rho_a)}{18\mu_a} \qquad (3.2)$$

$$v(t) = v_t \left(1 - e^{-\frac{t}{\omega}}\right) \qquad (3.3)$$

$$\omega = \frac{C_\tau v_t}{g} \qquad (3.4)$$

$$H(t) = v_t \left(t - \omega - \tau e^{-\frac{t}{\omega}} \right) \qquad\qquad (3.5)$$

where ρ_w and ρ_a are densities of water and air, g is gravity, D_0 is the drop diameter, $v(t)$ is the drop velocity at each moment, v_t is the terminal drop velocity, t is time, ω is response time, $H(t)$ is the height that the drop has to travel before reaching the 95% of terminal velocity, and μ_a is the air dynamic viscosity ($18 \cdot 10^{-6}$ Pa·s). Figure 3.2 (b) compares the velocity to distance relationship between experimental and van Boxel's data for a 3-mm drop, showing a good agreement.
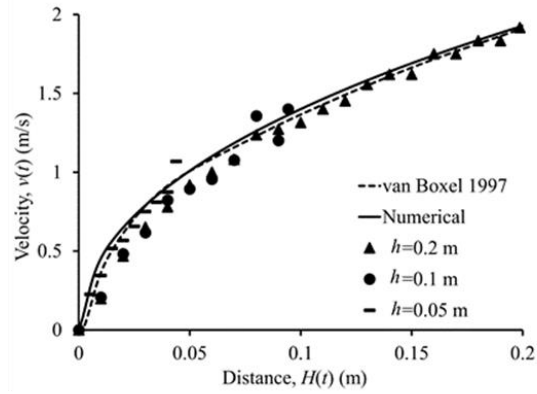
Figure 3.2 (a) Experimental setup, (b) velocity versus falling distance graphs of drops.

The drop behavior during impact and post-impact phases is studied by analyzing different drop and surface interaction properties. The drop's initial kinetic and surface energy dissipates during an impact by increasing the solid-liquid contact area and the viscous dissipation energy loss. Solid-liquid interactions are the primary reasons for this energy dissipation (112). The spread diameter at each moment and maximum spread diameter are normalized by the initial drop diameter and defined as the spread factor ($\beta = D_{(t)}/D_0$) and maximum spread factor ($\beta_{max} = D_{max}/D_0$), respectively. Eq. 3.6 shows the kinetic energy (E_k) at the impact point. Median diameter spherical drop is adopted in calculations, although we observed minor oscillations of the drop shape and during the falling time. After the drop reaches the maximum spread, it retracts and loses some

energy due to viscous dissipation. A dimensionless rebound criterion (E_{rex}) is defined based on energy conservation equations between the spreading and rebound stages in Eq. 3.7, in which the remaining energy of drop after retraction is normalized concerning the surface energy of the drop, assuming full recovery and attaining the original shape and diameter (Figure 3.3 (a)) (66):

$$E_k = \frac{\pi}{12} D_0^3 \rho v_i^2 \qquad\qquad (3.6)$$

$$E_{rex} = \frac{1}{4} \left(\frac{D_{max}}{D_0}\right)^2 (1 - cos\theta) - 0.12 \left(\frac{D_{max}}{D_0}\right)^{2.3} (1 - cos\theta)^{0.63} + \frac{2}{3} \left(\frac{D_0}{D_{max}}\right) - 1 \qquad (3.7)$$

where D_{max} is the drop diameter at maximum spread moment, D_0 is the initial drop diameter, v_i is the impact velocity, ρ is the water density, Re is the Reynolds number, and θ is the static contact angle.

Young's equation (96) can calculate the contact angle on flat and ideally smooth surfaces. However, when the surface is rough, the contact angle is computed with the theoretical equations of Wenzel (94) (Eq. 3.8) or Cassie-Baxter (93) (Eq. 3.9), based on the fact that the drop penetrates the surface grooves or air bridges remain in the gaps, respectively. In the Cassie-Baxter model, the close packing of grains produces tiny grooves acting as bridges for liquid. However, prominent the gaps between grains, not bridged but filled with water, lead to the Wenzel model:

$$\cos\theta_w = r \cdot \cos\theta_e^Y \qquad\qquad (3.8)$$

$$\cos\theta_{C-B} = \varphi_s \cdot \cos\theta_e^Y - (1 - \varphi_s) \quad (3.9)$$

where θ_w is the Wenzel contact angle, θ_{C-B} is the Cassie-Baxter contact angle, θ_e^Y is the static equilibrium contact angle on a flat smooth silica surface, r is the roughness factor defined as the ratio of the actual area of liquid-solid contact to the projected area and φ_s is the solid fraction and defined as solid-liquid contact (or solid) fraction of the surface.

To better identify the post-impact behavior of drop and quantify the impact outcomes, such as are splashing and non-splashing behavior, non-dimensional parameters are used:

$$Re = \frac{\rho v D_0}{\mu_f} \qquad\qquad (3.10)$$

$$We = \frac{\rho v D_0^2}{\sigma_s} \qquad\qquad (3.11)$$

$$Oh = \frac{\sqrt{We}}{Re} \qquad\qquad (3.12)$$

$$K_s = We^{\frac{1}{2}}Re^{\frac{1}{4}} \qquad\qquad (3.13)$$

where *Re*, *We*, and *Oh* are Reynolds, Weber, and Ohnesorge numbers, respectively, ρ is the water density equal to $\rho_w=1000$ kg/m³, μ_f is the fluid's dynamic viscosity, σ_s is the fluid surface tension, *v* is the velocity, K_s is the splash factor previously used, and D_0 is the initial drop diameter equal to the average drop diameter when airborne (80). The splash factor defines a threshold between the drop splashing and non-splashing, which may thus modify the soil erosion process (81).

The correlations and analysis methods are summarized in Table 3.2. Some of the models listed in Table 3.2 are insensitive to wettability, such as models proposed by Bayar and Megaridis (71), Clanet et al. (69) and Roisman et al.and Roisman et al. (113), others such as Tang et al. (114) and Wildeman et al.and Wildeman et al. (74) proposed models which are sensitive to wettability. Tang et al. (114) also included the roughness effect in their proposed model.

Table 3.2 Different models for the maximum spreading factor

Reference	β_{max} correlation	Surface/liquid properties	
Clanet et al. (69)	$\beta_{\max} \sim We^{0.25} \; for \; (We/Re^{\frac{4}{5}} < 1)$	Rigid	Insensitive to wettability
Bayer and Megaridis (71)	$\beta_{\max} \sim 0.72(We/Oh)^{0.14}$	Rigid	Insensitive to wettability
Roisman et al. (113)	$\beta_{\max} = a\,Re^{\frac{1}{5}} - b\,Re^{\frac{2}{5}}We^{-\frac{1}{2}}$ $(a, b) = (0.87, 0.4)$	Rigid	Insensitive to wettability
Nefzaoui and Skurtys (80)	$\beta_{max} \propto We^{\frac{1}{4}}$	Deformable	Liquid with low surface tension
Nefzaoui and Skurtys (80)	$\beta_{max} \propto We^{\frac{1}{5}}$	Deformable	Liquid with higher surface tension
Martson et al. (115)	$\beta_{max} \propto We^{\frac{1}{5}}$	Deformable	Low viscosity liquid Water drop on hydrophobic powder
Zhao et al. (84)	$\beta_{max} \propto We^{0.17}$	Deformable	Soda lime glass beads
Zhao et al. (83)	$\beta_{max} \propto We^{*\frac{1}{10}} \propto Re^{*\frac{1}{5}}$	Deformable	Large hydrophilic grains
	$\beta_{max} \propto We^{*\frac{1}{4}}$ We^* and Re^* (Effective We, Re)	Deformable	Small hydrophilic grains and hydrophobic grains
Wildeman et al. (74)	$\dfrac{3(1-cos\theta)}{We}\beta_{max} + \dfrac{\alpha}{\sqrt{Re}}\,\beta_{max}{}^2\sqrt{\beta_{max}-1}$ $= \dfrac{12}{We} + \dfrac{1}{2}$ $We > 30,\ \alpha=0.7$	Rigid	Sensitive to wettability
Supakar et al. (85)	$\beta_{max} \propto We^{\frac{1}{3}}$	Deformable	Insensitive to wettability

Table 3.2 Different models for the maximum spreading factor, continued.

Reference	β_{max} correlation	Surface/liquid properties	
Tang et al. (114)	$\beta_{\text{max}} = a(We/Oh)^b$	Rigid	Sensitive to roughness, wettability
Mozhi Devan Padmanathan et al. (89)	$\frac{6.36}{Re}\beta_{max}{}^4 + \left(\frac{6}{We}\right)\beta_{max}{}^2 - \left(\frac{12}{We} + \frac{1}{2} - k\left(\frac{Bo}{We}\right)^{\frac{1}{3}}\right) = 0$	Deformable	Poly(tetrafluoroethylene) (PTFE) particles
Lardier et al. (97)	$\beta_{max} \propto Re^{0.15}$	Deformable	Silica sand and Egmont soil

3.3 Results and Discussion

3.3.1 Post-impact spread behavior on horizontal surface

Water-drop experiments on fine, medium and coarse sand in dry hydrophilic (natural) and hydrophobic states investigate the effects of hydrophobicity and granularity. The raindrops with 1-7 mm diameters can reach terminal velocities of 9 to 13 m/s (116). This study varies the impact velocities (v_i) between 0.99 m/s and 6.0 m/s to investigate the effect of the kinetic energy of drops on its post-impact behavior. Figure 3.3 illustrates the characteristic drop's post-impact transformations in selected experiments with a 6-mm drop on hydrophobic and hydrophilic fine grain sand surface at 0.99 m/s and 3.13 m/s.

During the post-impact phase, the drop slightly retracts and stabilizes on the hydrophilic fine sand with a contact angle of 60° (Figure 3.3 (b) and 3.3(d)). In contrast, Figure 3.3 (a) shows that after the drop reaches a maximum spread diameter on the hydrophobic fine sand surface, the flow changes inward, and the drop partially recoils and rebounds. Finally, after a few oscillations, the drop stabilizes and deposits at a contact angle of 115°. Figure 3.3(c) shows detachment and splash as the outcome of the drop with 3.2 m/s and higher impact velocities on the same fine hydrophobic surface. Detachment and splash in hydrophobic sand (Figure 3.3 (c)) occur due to

lower surface tension, weakening fluid-solid bonds. Thus the drop expands and reaches the breaking point.

Figure 3.4 (a-d) quantifies grain size and hydrophobicity effects on the spread factor versus dimensionless time ($t^*=t$ (v_i/D_0)). It is shown that, by increasing the impact velocity, the dimensionless time to maximum spread diameter increases, unaffected by grain size in hydrophobic sand. Figure 3.4 (a) and (b) show the maximum dimensionless time for three different grains is approximately the same. Therefore, the hydrophobicity dominates over the roughness effect for the maximum spread time, especially at lower impact velocities. The maximum spread factor on fine-grained hydrophobic sand is 20 % larger than on coarse at 0.99 m/s drop impact velocity. Furthermore, when the drop impact velocity increases to 3.13 m/s, the fine-grained hydrophobic sand spread factor is 45 % larger than coarse. This increase in hydrophilic fine grain sand compared to coarse is about 17 % for a drop with an impact velocity of 0.99 m/s and 60 % for an impact velocity of 3.13 m/s. The hydrophilic sand results (Figure 3.4 (c-d)) indicate that the time to maximum spread is slightly affected by the grain size. The maximum dimensionless spread time on fine hydrophilic sand is higher than on medium and coarse sands. The normalized maximum spread time is weakly affected by the grain size at lower impact velocities; however, the grain size effect becomes more prominent at higher impact velocities. In addition, hydrophobicity seems to diminish the grain size effect on the normalized maximum spread time.
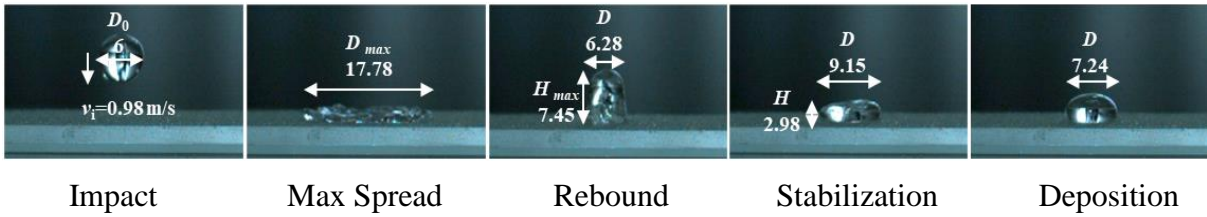
(a) **Hydrophobic fine sand**: Low impact 0.98 m/s velocity of a 6-mm drop
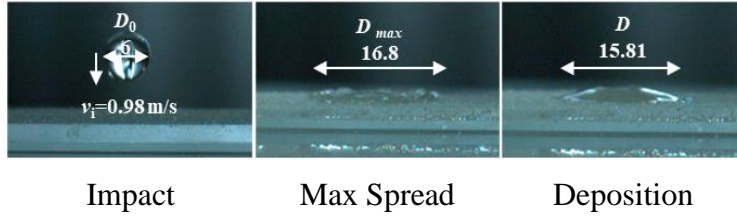
(b) **Regular fine sand**: Low impact 0.98 m/s velocity of a 6-mm drop
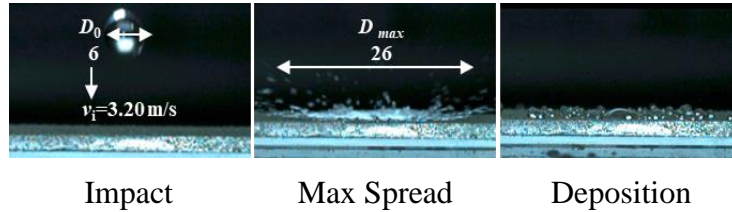
(c) **Hydrophobic fine sand**: High impact 3.2 m/s velocity of a 6-mm drop
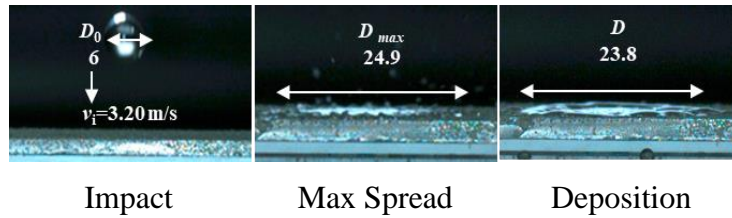
(d) **Regular fine sand**: High impact 3.2 m/s velocity of a 6-mm drop

Figure 3.3 Drop impact and post-impact spread in hydrophobic and hydrophilic fine grain sand surface.
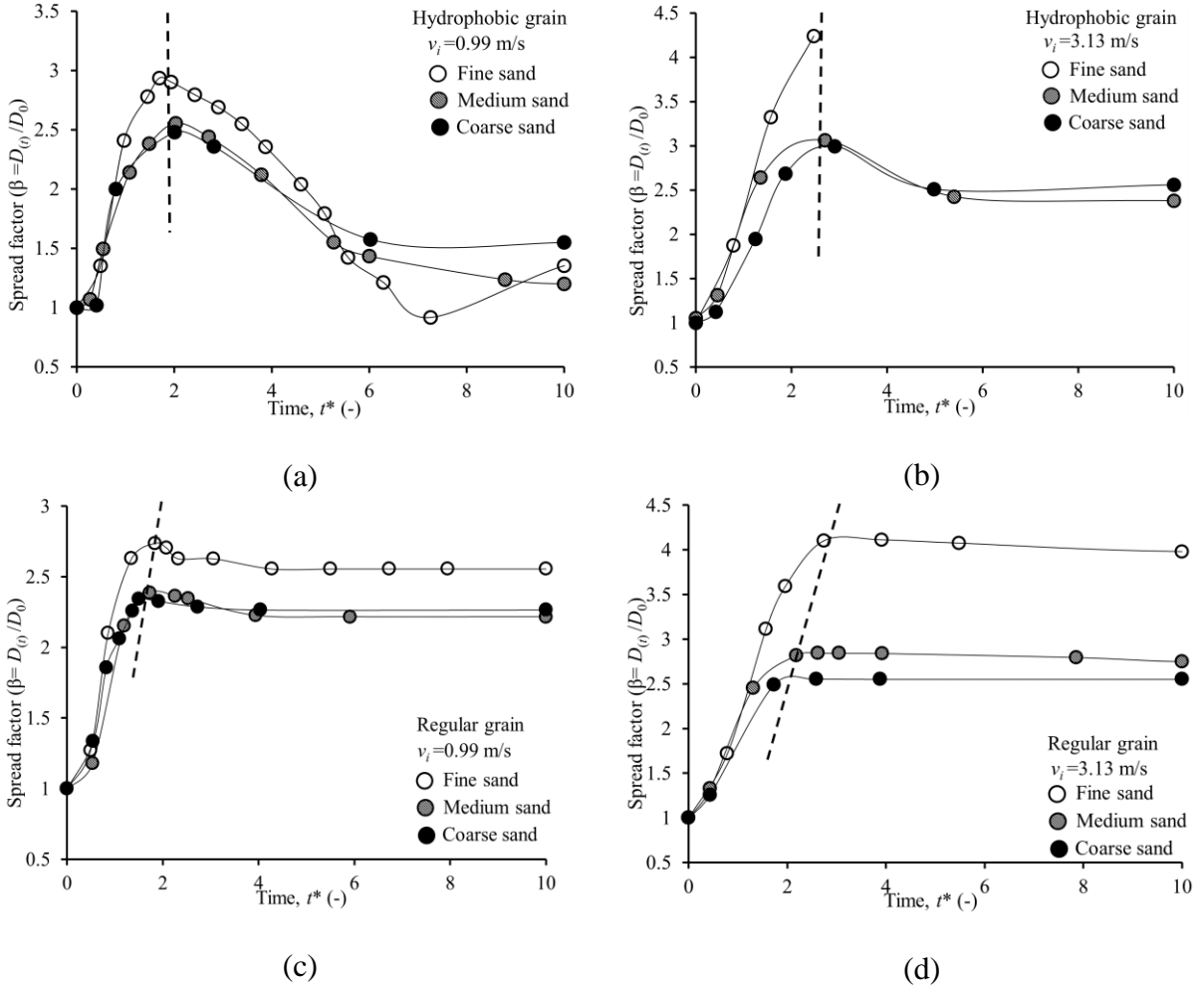
Figure 3.4 Spread factor versus normalized time (t^*) for (a-b) hydrophobic, (c-d) hydrophilic fine, medium, and coarse grain sand

The maximum spread factor versus *We* is extracted for similar grain sizes from different studies and compared to our results for fine sand. The grain diameter for the extracted results is about 200 μm, which is like the median grain size of fine-grain sand that we have used for this study. The comparison aims to demonstrate the effect of the grain bed deformability and the heterogeneity of the granular matter. As mentioned in the materials and methods section, we used a fixed bed of heterogeneous sand samples in this study. Therefore, the results from a deformable bed of hydrophobic soda-lime grains, clean ceramic and ceramic (83), and two silica sand and Egmont soil (97) are extracted and compared to the fixed hydrophobic and hydrophilic fine sand.

The maximum spread factor in the fixed hydrophobic and hydrophilic sand is more significant than the deformable-grain bed results (Figure 3.5 (a)). This is because the deformable bed grain mobility during the impact suppresses the maximum spread of the drop on the surface. In addition, the attachment of the grains to the drop can also be another reason for the lower spread diameter.

Furthermore, the effect of surface particle size heterogeneity can be seen by comparing the results of heterogeneous samples and uniform-grain size samples for hydrophobic and hydrophilic results. From Figure 3.5 (b) and (c), the maximum spread factor in hydrophobic samples has a narrower distribution than hydrophilic samples. However, grain size distribution can be essential in interpreting these results.
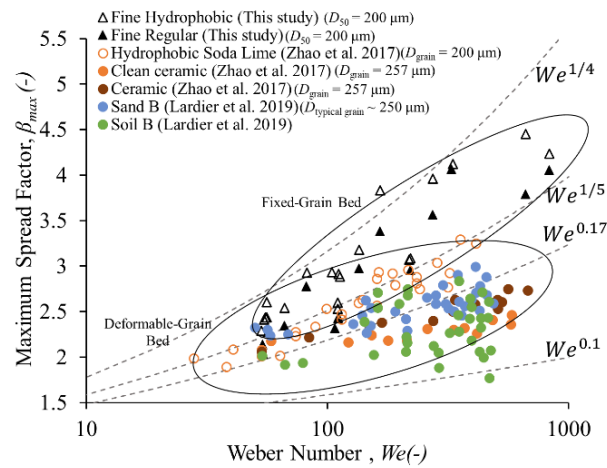
(a)

Figure 3.5 Comparison of maximum spread factor versus Weber number from different studies

(b)   (c)
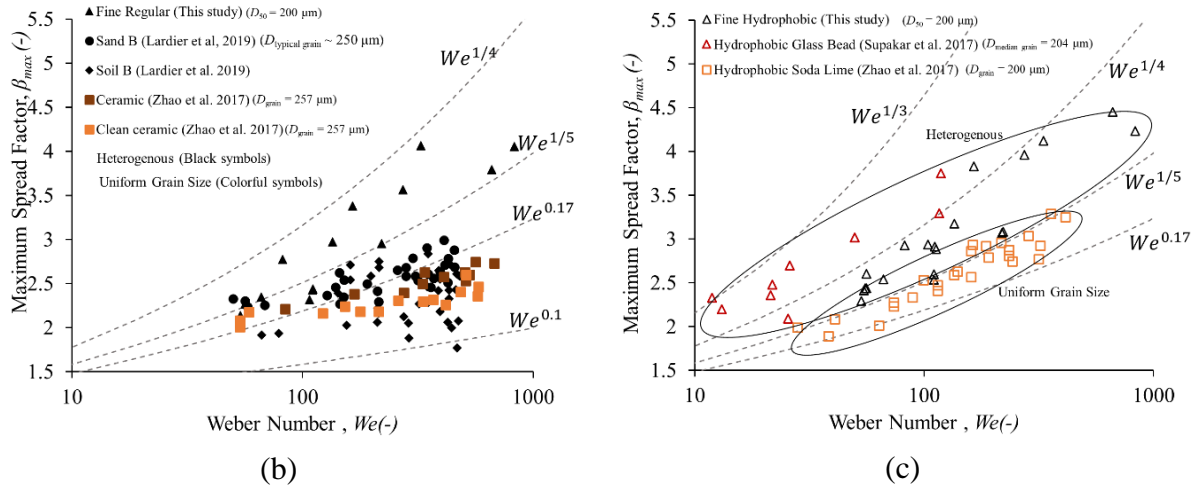
Figure 3.5 Comparison of maximum spread factor versus Weber number from different studies, continued.

Figure 3.6 summarizes the coupled kinetic energy, grain size, and hydrophobicity effects on the maximum spread factor using the We/Oh ratio. The best-fitted line to the results is obtained and illustrated for hydrophobic and hydrophilic grains. The results show the experimental maximum spread number can be fitted to a line that follows a power law of $\beta_{\max} \approx a \left(\frac{We}{Oh} \right)^b$.
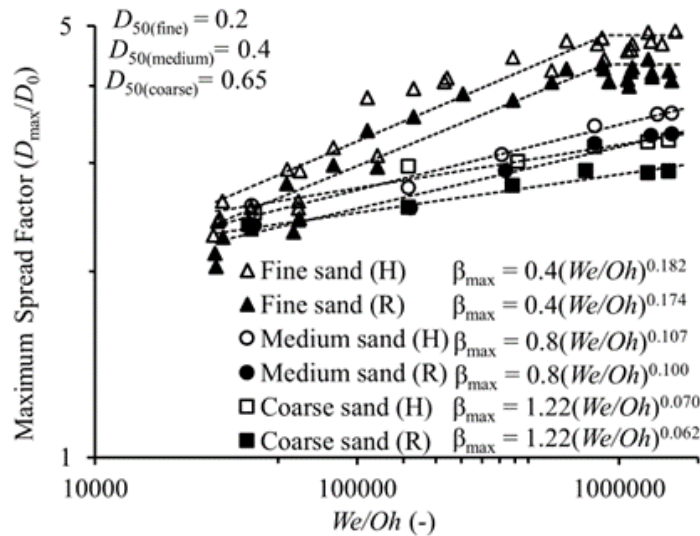
Figure 3.6 Maximum spread factor versus We/Oh for fine, medium, and coarse hydrophobic (H) and hydrophilic (R) soils. The best fit logarithmic correlation for each soil is shown on the graph.

The fitting parameters *a* and *b* vary for different grain sizes. For fine-grain sand, the fitted line applies to the results with *We*<1000. For *We*>1000, the maximum spread diameter is almost constant at 4.88 for hydrophobic and 4.3 for hydrophilic grain. According to Tang et al. (114), surface roughness affects the maximum drop spread. Tang et al. (114) reported different fitting parameters (*a*, *b*) at different roughness and with multiple impacting liquids. In this study, the *a* and *b* parameters are fitted to experimental results based on grain size, wettability, and maximum spread for each soil and compared with some of the empirical models obtained in previous studies (Table 3.3, Figure 3.6). The results show that a coupled effect of the hydrophobicity and the grain size controls the correlation between the maximum spread factor and the *We* number. Furthermore, the fitting parameter *a* is affected by the median grain size (D_{50}) and increases by increasing the grain size and roughness regardless of hydrophobicity. The fitting parameter *a* is approximated to be $2 \cdot D_{50}$ for the obtained results. The fitting parameter *b* seems to change under the combined effect of roughness and wettability and decreases by increasing the grain size. For the same grain size, the value of parameter *b* reduces by about ~0.007 for hydrophilic soil compared to the hydrophobic soil.

Figure 3.7 (a-c) show the comparisons of the measured and predicted non-dimensional maximum spread numbers using each of the references in Table 3.3. The results are separated into three subcategories: fine (Figure 3.7 (a)), medium (Figure 3.7 (b)), and coarse (Figure 3.7 (c)) sand. Results show that Bayer and Megaridis (71) and Tang et al.Tang et al.'s (114) models best agree with the experimental results for fine-grain soil. In contrast, Clanet et al. (69) Roisman et al. (113), and Wildeman et al.'s (74) models overestimate the maximum spread factor, with an error higher for hydrophilic grain types. The same models show higher errors for medium and coarse soils. Therefore, Tang's model with different fitting parameters for each soil agrees best

with the experimental results as stated earlier. By comparing various models with experimental data of the three different grain size soil, it can be concluded that the spread number is affected by a coupled effect of the grain size and the resulting surface roughness. However, the results indicate that grain size has more impact than wettability.

Table 3.3 Fitting parameters (a, b) for fine, medium, and coarse hydrophilic and hydrophobic grains

(a, b)	Fine (We< 1000)	Medium	Coarse
Hydrophilic	(0.4, 0.174)	(0.8, 0.100)	(1.22, 0.062)
Hydrophobic	(0.4, 0.182)	(0.8, 0.107)	(1.22, 0.07)
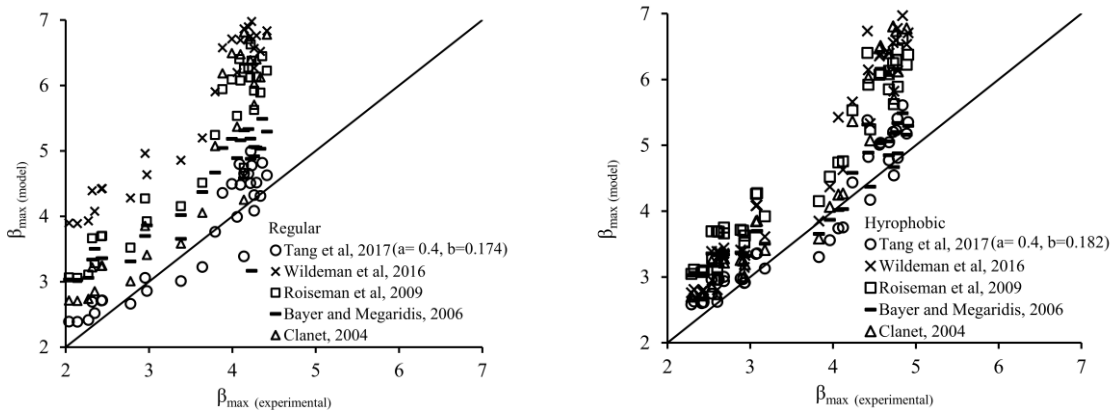
(a) Hydrophilic (left) and hydrophobic (right) fine sand

Figure 3.7 Comparison of experimentally measured β_{max} from this study to the predicted β_{max} from different empirical models in Table. 3.3

(b) Hydrophilic (left) and hydrophobic (right) medium sand

(c) Hydrophilic (left) and hydrophobic (right) coarse sand
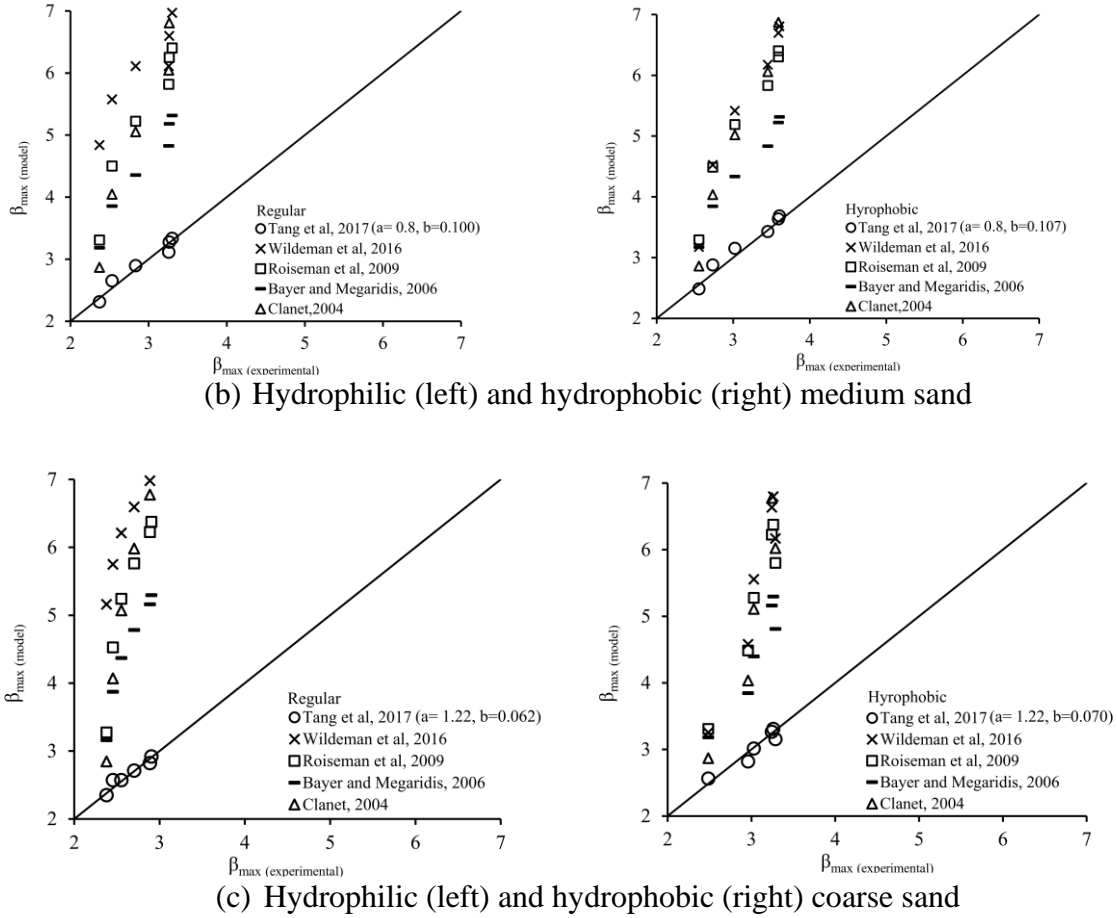
Figure 3.7 Comparison of experimentally measured β_{max} from this study to the predicted β_{max} from different empirical models in Table. 3.3, continued.

3.3.2   Post-impact splash behavior on horizontal surface

The drop splashes into many tiny droplets on fine hydrophobic sand, while in medium and coarse, the drop remains in fingers post-splash (Figure 3.8 to Figure 3.10). Thus, the effect of hydrophobicity on splash is bolder in fine-grain sand compared to medium and coarse grain sand. Figure 3.11 (a), (b), and (c) show the splash parameter versus the Reynolds number to delineate the effect of hydrophobicity on the splashing threshold. Although Nefzaoui and Skurtys (80) established the splashing threshold as K_s=120 for dry hydrophilic granular substrate, our research shows the splashing threshold depends on grain size and hydrophobicity. Figure 3.11 (d), shows

that the grain size affects the splash threshold in hydrophilic sand, with coarse sand exhibiting the lowest value for the splash threshold. However, the grain size effect on the splash threshold is negligible when the sand turns hydrophobic. The fine sand splashing threshold decreases almost four times with hydrophobicity. On the contrary, coarse sand retains a similar splash threshold regardless of hydrophobicity.
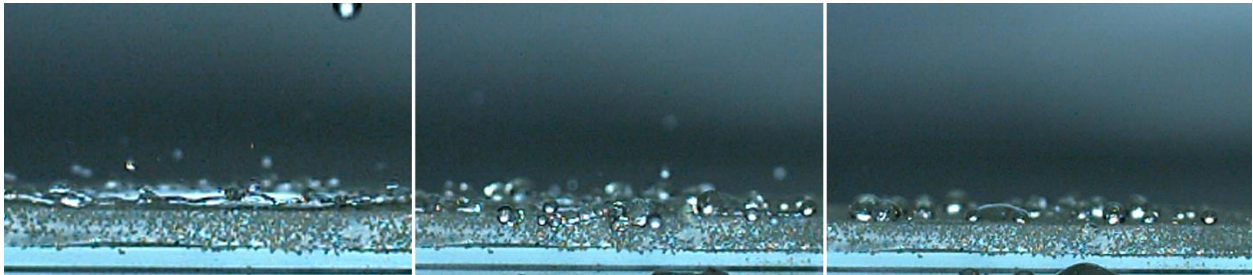
Figure 3.8 Post-impact splash behaviour in fine-grain hydrophobic sand with v_i=1.4 m/s.
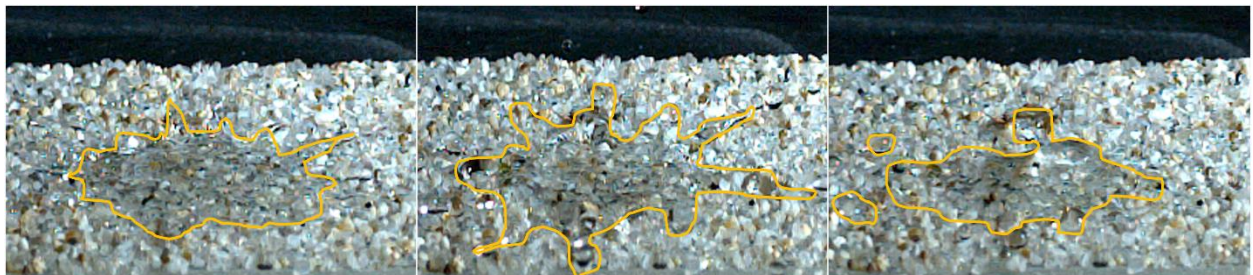
Figure 3.9 Post-impact splash behaviour in medium grain hydrophobic sand with v_i=1.4 m/s.
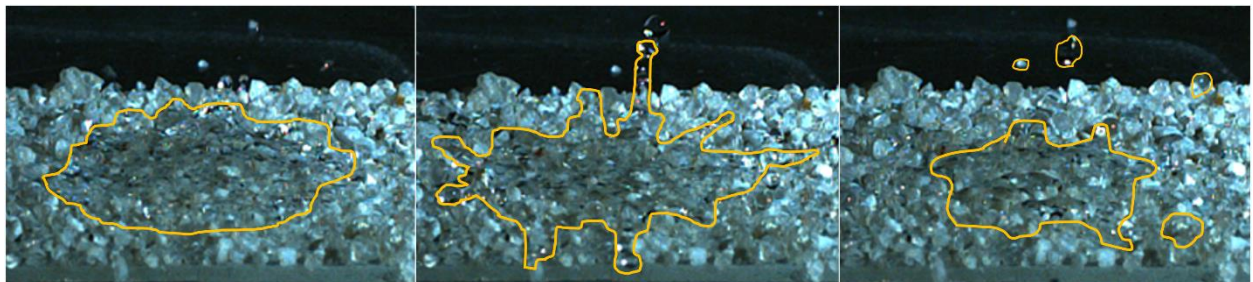
Figure 3.10 Post-impact splash behaviour in coarse grain hydrophobic sand with v_i=1.4 m/s.
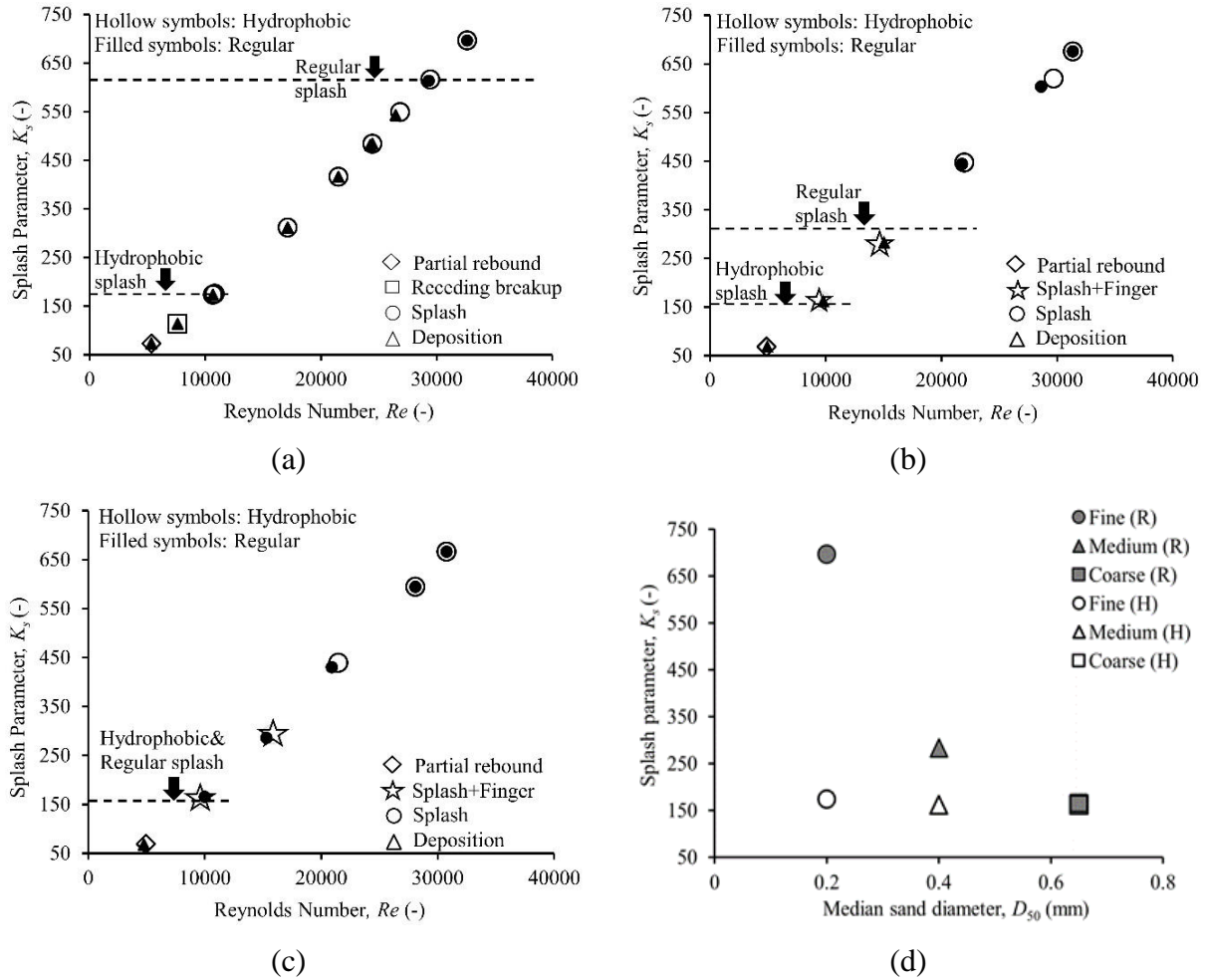
Figure 3.11 Splash factor (K_s) versus Reynolds number (Re) for (a) fine, (b) medium, and (c) coarse grain sands, and (d) splash factor (K_s) versus median sand diameter

Outcomes of all drop tests are shown for hydrophobic and hydrophilic surfaces as two deposition and splash regimes in Figure 3.12. In an earlier study by Palacios et al. (117), a correlation is obtained for the splash threshold on dry glass surfaces with different liquids. A correlation represented by $We_{splash} = 5.75Re^{0.5}$ perfectly separates the two regimes of splashing and deposition for all hydrophobic grain tests in our study (Figure 3.12 (a)). However, in hydrophilic grain tests, this correlation only accounts for the splashing threshold in medium grain.

49
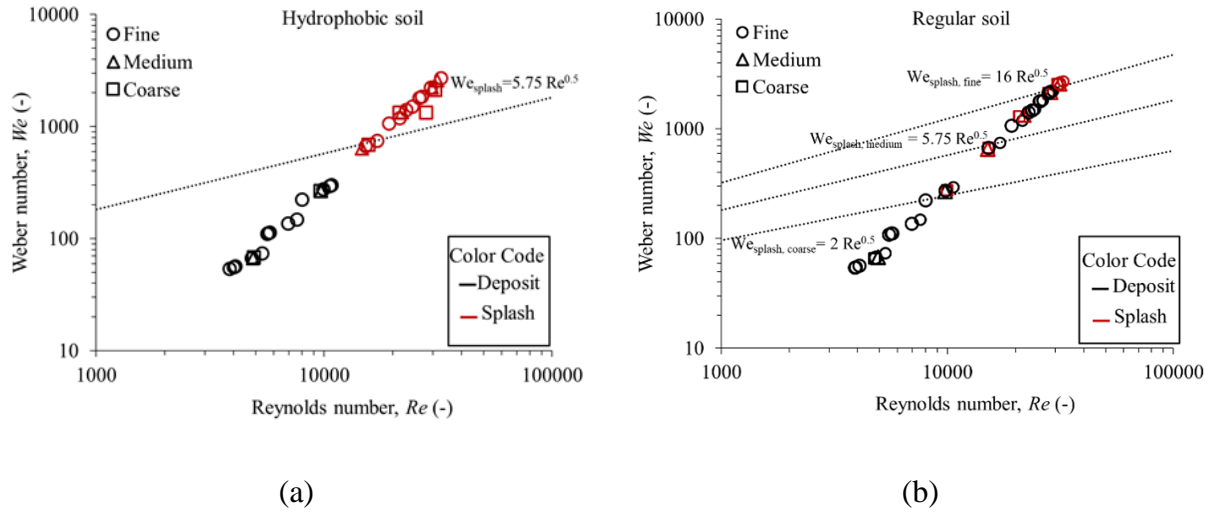
Figure 3.12 Splash versus deposition outcomes for (a) hydrophobic and (b) hydrophilic fine, medium, and coarse soil (red symbols indicate the splashing behavior, and black symbols indicate deposition.

Figure 3.13 shows the excess rebound energy obtained through energy conservation relations between maximum spread and recoil/rebound of the droplet and normalized for the drop's surface energy (Eq. 3.7). Ideally, the excess rebound energy equals the surface energy if the drop fully recovers its spherical shape. The rebound criterion estimates post-spread drop contraction and available remaining energy for downslope mobility. The positive normalized excess rebound energy, or when the rebound energy is more than surface energy, quantifies the droplet rebound potential. Negative values, when the rebound energy is less than surface energy, occur in cases of drop deposition.

Results show that the fine hydrophobic sand has the highest tendency to rebound, which decreases on medium and coarse hydrophobic sands (Figure 3.13). The splashing drops are shown with red symbols for both hydrophobic and regular sands in Figure 3.13. Although the splash parameter threshold (K_s) in hydrophobic sands is roughly the same, a higher rebound criterion of fine sand at the splash threshold leads to a more intense splash.
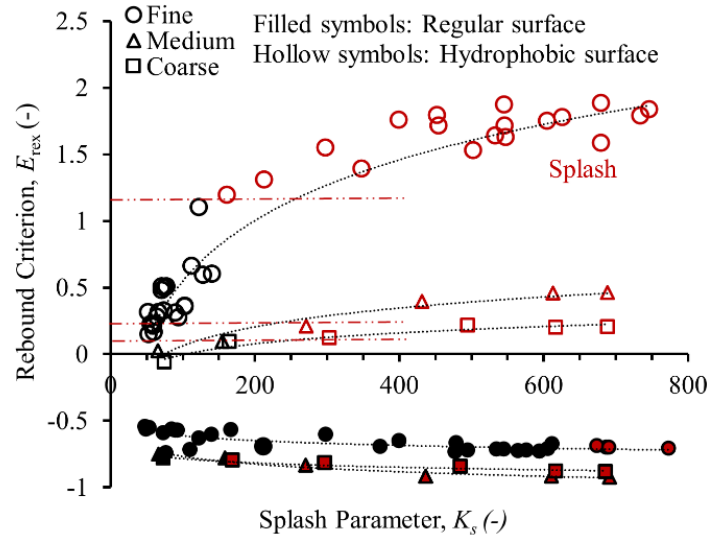
Figure 3.13 Excess rebound energy criteria versus maximum spread factor for different sand surfaces.

3.3.3 Effect of surface roughness on drop downslope mobility on inclined surface

We assess the surface wettability and drop type behavior on hydrophobic sands using theoretical models to evaluate the pore geometry and particle packing on the drop motion. Wenzel and Cassie- contact angles are calculated for each sand sample. Table 3.4 shows that the measured contact angle for coarse sand for hydrophobic samples is close to the calculated Wenzel contact angle. In contrast, the observed contact angle is more relative to the contact angle calculated by the Cassie-Baxter equation in medium grain and fine sands. The Cassie-Baxter contact angle is related to the fraction of the surface that is in contact with the liquid.

Table. 3.4 Contact angle measurements from Eq. 3.8, 3.9 and experimental observations

Soil	Experimental	θ_e	r	φ_s	Theoretical	
Fine	115°		3.6	0.62	115°	Cassie-Baxter
Medium	100°	91°	4.5	0.82	100°	Cassie-Baxter
Coarse	96°		5.87	-	95.9°	Wenzel

51

For each soil sample, the roughness factor and solid fractions are calculated using the scanned surface profiles with Filmetrics Profilm3D Optical Profiler. The roughness factor is obtained by dividing the total surface area of the scanned sample by the total projected area. The solid fraction represents the wetted area by the total projected area ratio.

The observed contact angles for coarse ($\theta=96°$) is very close to the theoretically calculated Wenzel contact angle ($\theta_w=95.9°$). The contact angles of medium hydrophobic soil ($\theta=100°$) and fine hydrophobic soil ($\theta=115°$) are larger than the calculated Wenzel angles for each soil ($\theta_w=95°$ for medium and $\theta_w=94°$ for fine). Thus, the observed contact angles are more relative to Cassie-Baxter regime. The fraction of wetted solids was assessed by back-calculating its value from the measured contact angle and a total developed surface area of each sand. The fraction of wetted solids (φ_s) is 0.82 in hydrophobic medium soil and 0.62 in fine hydrophobic soil, respectively. Furthermore, the experimental observations, which will be discussed in later sections and analysis, such as drop mobility (Figure 3.14) on fine and medium hydrophobic surfaces, support the above-mentioned theories.

Drop on finer hydrophobic sand has more mobility and jumps. Drop impact and post-impact velocities are tracked on $\delta=30°$, $40°$, and $45°$ slopes. An average downhill velocity of the drop increases nonlinearly in steeper hydrophobic slopes, including sliding and rolling (Figure 3.14). Thus, the drop oscillates and reforms between a flatter shape and a sphere. The drop tends to slide more when it is in a flatter shape, while it starts rolling when it goes back to its spherical shape. While the downhill velocity of drop increases in steeper hydrophobic slopes, the drop remains in place for all hydrophilic slopes. On hydrophilic slopes, regardless of their steepness, the drop spreads and stretches for a negligible distance and finally deposits and stabilizes on the surface. The results clearly show that drop has a higher downhill velocity on the fine-grain slope

on all slopes compared to medium and coarse slopes. The medium and coarse soil show lower and similar velocities in lower angles; however, by increasing the steepness, the velocity gap between the medium and coarse slopes becomes more prominent. Overall, it can be concluded that hydrophobicity has a significant role in increasing drop mobility, and this effect is even bolder by decreasing the grains' size. Further, the fine and medium hydrophobic sands surface resembles the Cassie-Baxter contact, which eases the fluid movement on the surface. On the contrary, coarse-grain sand has the Wenzel regime.
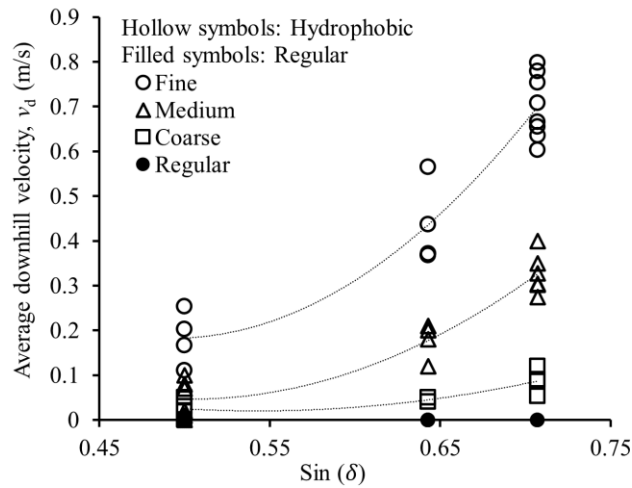
Figure 3.14 Average downhill velocity of the drop versus the slope angle for hydrophobic and hydrophilic surfaces.

Figure 3.15 illustrates the drop paths on the fine, medium, and coarse hydrophobic grain slopes with impact velocities of $v_i = 0.98$ m/s and 1.4 m/s. Drop post-impact jump is more prominent at lower impact velocity, fine-grained sand, and steeper slope where jumps are longer in Figures 3.15 (c) and (d). General downslope drop mobility increases with smaller grain sizes and steeper slopes. As it is compared in Figure 3.15 (a), on a 30° slope, the drop rolls and slides downward and stops after traveling a short distance on the coarse hydrophobic slope. The traveling distance increases in medium slope, and in the case of the fine-grain slope, the drop travels the

whole slide length. A similar trend can be observed on a steeper slope; however, the traveled distance has slightly increased for coarse and medium soils due to the gravity effect (Figure 3.15 (c)).
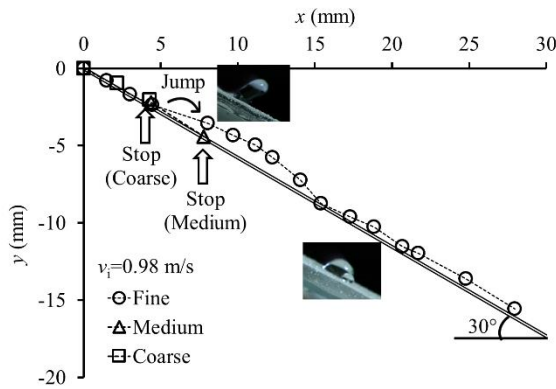
a) Drop falling on 30° slope, v_i=0.98 m/s
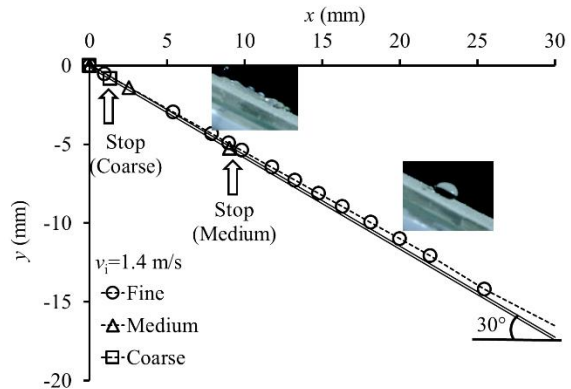
b) Drop falling on 30° slope, v_i=1.4 m/s
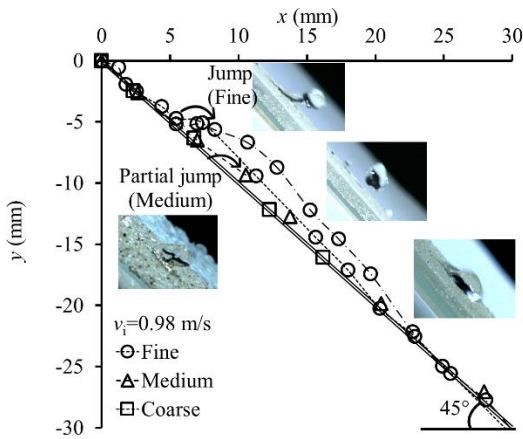
c) Drop falling on 45° slope, v_i=0.98 m/s
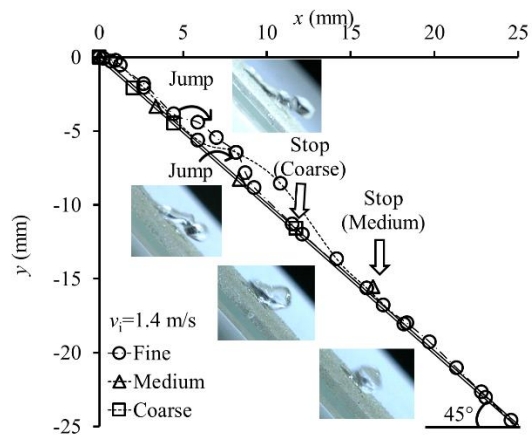
d) Drop falling on 45° slope, v_i=1.4 m/s

Figure 3.15 Drop trajectories on fine, medium, and coarse grain slopes.

Figure 3.16 shows the snapshots of drop impact and post-impact moments for fine to coarse hydrophobic and hydrophilic slopes. In a 45° fine hydrophobic slope, after the drop reaches the maximum spread, it rebounds and has a secondary partial jump (Figure 3.16 (a)) with a tail

formation that reduces the drop speed. Frequently, the tail detaches, and the drop slides and rolls down. The drop tends to jump on the medium hydrophobic slope, and a tail forms but slides with a lower velocity than the fine-grain surface (Figure 3.16 (c)). However, the drop spreads and moves slightly on the coarse hydrophobic slope, stretches, and deposits (Figure 3.16 (e)). Finally, on all the hydrophilic sand inclined surfaces, the drop spreads, retracts slightly, extends, and deposits on the slope with no further movement (Figure 3.16 (b), (d), and (f)).
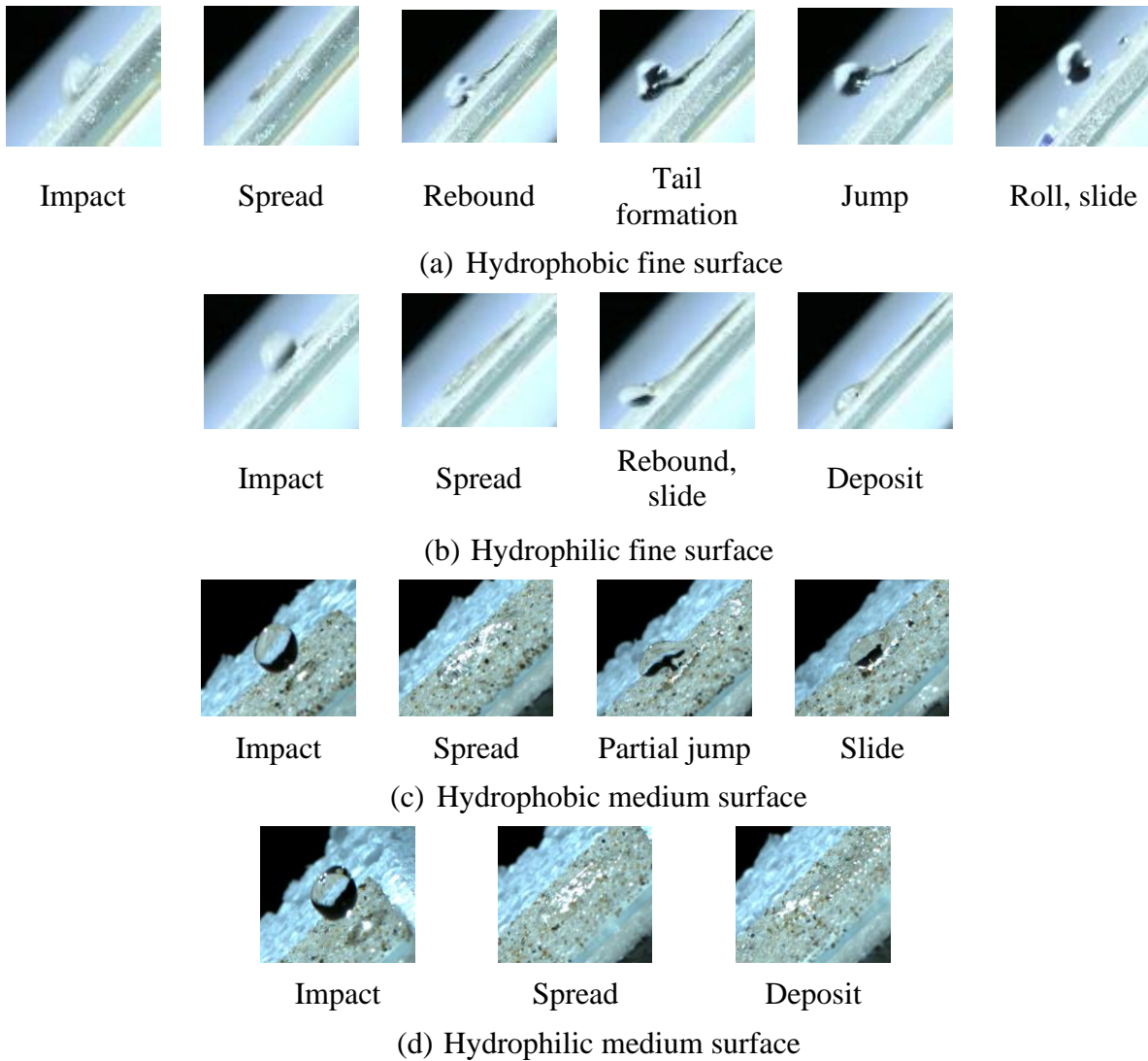
| Impact | Spread | Rebound | Tail formation | Jump | Roll, slide |

(a) Hydrophobic fine surface

| Impact | Spread | Rebound, slide | Deposit |

(b) Hydrophilic fine surface

| Impact | Spread | Partial jump | Slide |

(c) Hydrophobic medium surface

| Impact | Spread | Deposit |

(d) Hydrophilic medium surface

Figure 3.16 A drop falling on 45° slope with v_i=0.98 m/s.

Impact   Spread   Deposit

(e) Hydrophobic coarse surface

Impact   Spread   Deposit

(f) Hydrophilic coarse surface
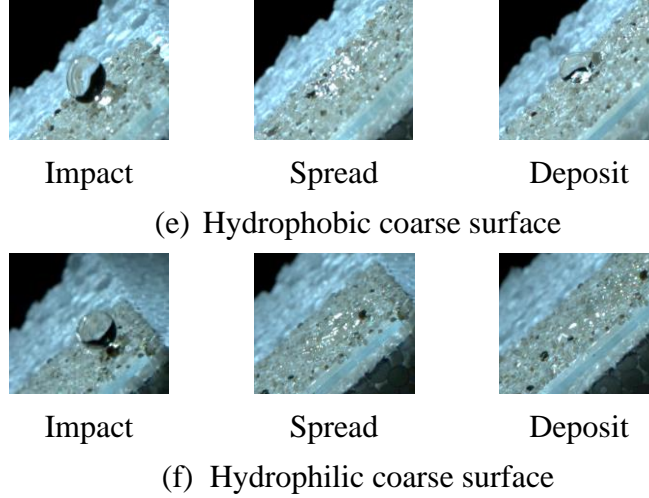
Figure 3.16 A drop falling on 45° slope with v_i=0.98 m/s, continued.

Figure 3.17 categorizes the outcome of drop impact on 30, 40 and 45° slopes with fine, medium and coarse sand based on the normalized spread coefficient (S/γ_{LV}). A normalized spreading coefficient indicates the sand-liquid interaction (118). The Gibbs free energy change ($\Delta G = -S = \gamma_{LS} + \gamma_{LV} - \gamma_{SV}$) (119) characterizes the spreading coefficient (S) during the spreading process. Where γ_{LS} is interfacial energy between liquid and solid, γ_{LV} is the interfacial energy between liquid and vapor, and γ_{SV} is the interfacial energy between vapor and solid. For static contact angles $\theta > 0$, by dividing the spreading coefficient (S) by γ_{LV} and using Young's equation (96) the normalized spread coefficient (S/γ_{LV}) is equal to ($cos\theta - 1$) .

The normalized spread coefficient is shown versus the normal Weber number ($We_N = \frac{\rho \, v_i cos\delta \, D_0^2}{\sigma_s}$) which is obtained using the normal component of the impact velocity on the inclined surface with different slope gradients (δ). The impact outcomes are categorized as partial bounce, fragmentation, and deposition. As it is shown in Figure 3.17, the drop partially bounces (green symbols) on fine hydrophobic sand at We_N< 60. At higher We_N the drop breaks up (fragmentation) to smaller drops that are shown with orange symbols in the figure and the partitioned drops roll

down the slope. In medium hydrophobic sand, the drop partially bounces at $We_N < 50$ and

fragmentation occurs at higher We_N. Drops deposit at $We_N < 30$ in medium sand and before

transiting to partial bounce. Partial bounce is not observed in coarse hydrophobic sand tests. In the

coarse hydrophobic sand tests drops deposit and starts to break up with no further movement at

$We_N > 50$. In all hydrophilic sand tests, regardless of the grain size, the only outcome of the test

was deposition.
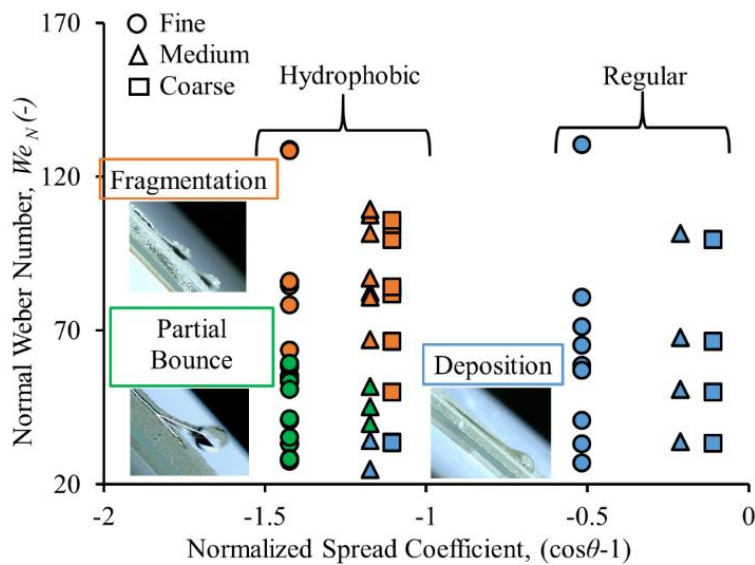
Figure 3.17 Normal Weber number (We_N) versus normalized spread coefficient for fine,
medium, and coarse hydrophobic and hydrophilic sands. The color code of the graphs indicates
the partial bounce with green symbols, fragmentation with orange symbols and deposition with
blue symbols.

The displacement of the drop mass center versus dimensionless time is shown in Figure

3.18. The movements at the impact moment, spreading phase, and subsequent motion are tracked

for the drop's center point. Displacement-time curves show a two-phase behavior, spreading and

mobilizing, on hydrophobic and hydrophilic surfaces. Figure 3.18 (a) shows the effect of three

slope angles on drop movement on fine-grain hydrophobic and hydrophilic sand slopes. Due to

gravity, steeper slopes cause more drop mobility overall on the hydrophobic sand. However,

hydrophilic fine, medium, and coarse sand surfaces did not permit significant drop-down-slope

mobility. Although the slope steepness significantly affects the drop mobility on both hydrophilic and hydrophobic fine-grained sand, the angle effect diminishes towards coarser sands (Figure 3.18 (b) and (c)). The drop behaves similarly on the hydrophilic and hydrophobic coarse sand, which means the grain size effect suppresses the hydrophobicity effect.

(a) Fine grain slopes, v_i=0.98 m/s

(b) 30° slope, v_i=0.98 m/s

(c)
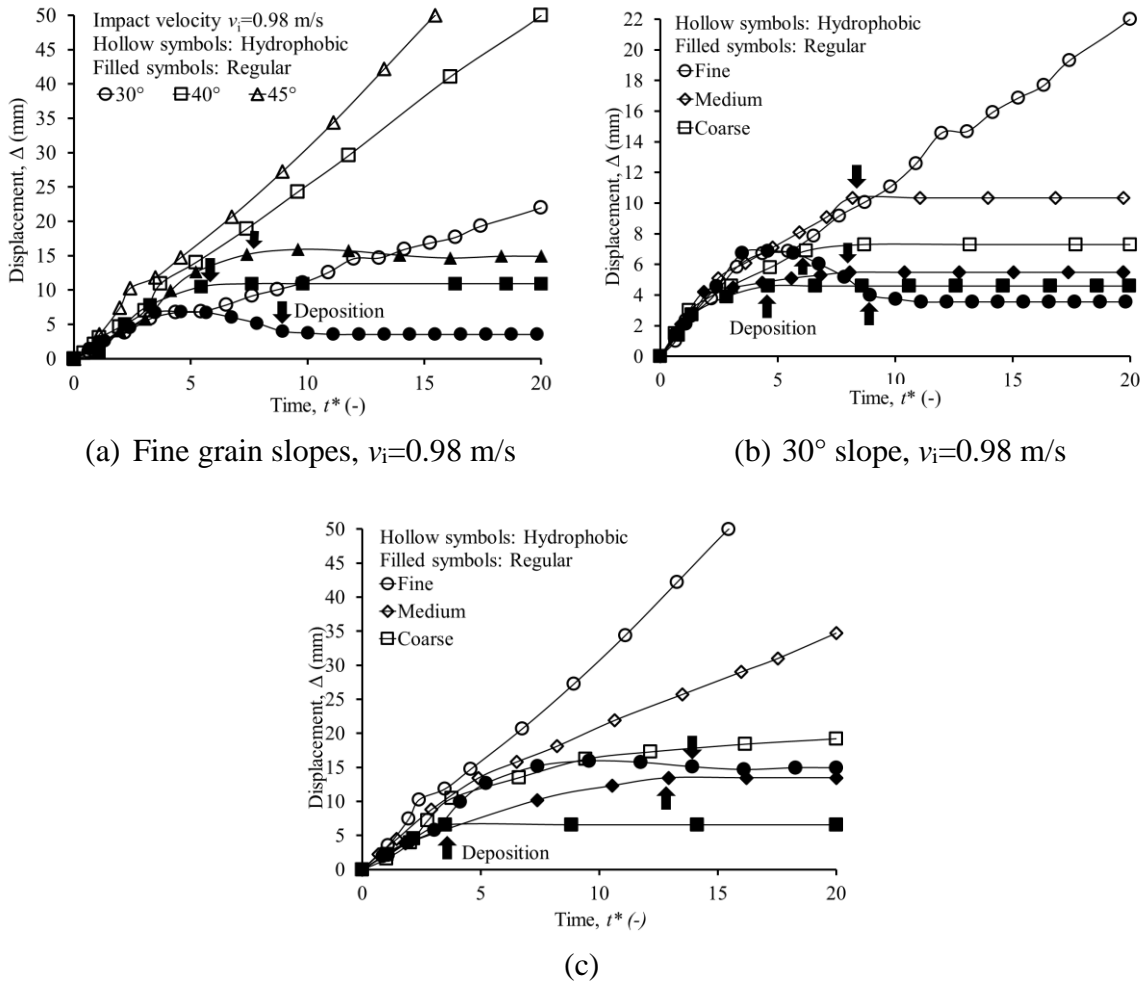
Figure 3.18 (a) slope effect (b) and (c) grain size effect on drop movement during the impact on the slope until it stops or traverses the whole slide length. Hollow and filled symbols show the hydrophilic surface and hydrophobic surfaces, arrows indicate deposition

3.4 Conclusions

This paper investigates how the grain size and hydrophobicity govern a water drop impact and post-impact spread and splash behavior on a fixed-grain flat and tilted sand surface. Surfaces lead to distinct drop behaviors, drop deposition, or drop splash behavior that is further analyzed. The motivation for this research comes from poor understanding or extensive slope erosion following raining events in wildfire burned areas which forms hydrophobicity in a thin surficial layer. This article contributes to a better understanding of why erosion occurs easier in hydrophobic fine-grained sands by showing drastic enhancement of raindrop splash in hydrophobic sands and as a result, explains the high mudflow severities in hydrophobic hills compared to unburned. The study found significant differences in the drop post-impact behavior for fine hydrophobic sand, compared to medium and coarse sand that were not anticipated before. Specifically, post-impact drop phases on horizontal hydrophobic sand surfaces differ from hydrophilic surface in terms of the existence of partial rebound and oscillation phases. Additionally, drop has more tendency to rebound on finer than coarse hydrophobic sand. The higher tendency to rebound is attributed to the higher contact angle and closely packed grains in fine-grain sand, and in medium sands, resulting in more air-entrapped grooves as in the Cassie Baxter model.

While hydrophobicity dominates over the roughness during the drop's post-impact spreading time, the grain size becomes a more prominent factor in hydrophilic sand spreading time. The maximum spread factor is also affected by the coupled effect of hydrophobicity and grain size. The maximum spread factor obtained from experimental results are fitted to the model proposed by Tang et al. (114) with different fitting parameters for each sand. The results show that both hydrophobicity and grain size affect the fitting parameters, with grain size playing a more

59

significant role in maximum spread diameter. We have found that the median grain size (D_{50}) can be applied to the model proposed earlier by (114). It is also indicated that the previously obtained *We-Re* numbers correlations only match with hydrophobic sample results and not with the hydrophilic sand in which grain size affects the correlation.

The splashing behavior of drop is affected by kinetic energy of the drop, and the coupled effect of hydrophobicity and fine sand particularly promotes drop splashing, which initiates at very low drop impact velocities in hydrophobic sands compared to hydrophilic. As the grain size increases, the splashing threshold gap decreases between hydrophobic and hydrophilic sand. Although, regardless of grain size, the splash parameter at which the drop starts to splash is roughly the same for all hydrophobic sand samples, the fine sand has a significantly higher rebound tendency at the splashing threshold compared to medium and coarse grain sands. Thus we concluded that the splash on finer hydrophobic sand is more intense and can lead to higher erosion rate. As it is shown in Figure 3.13 (a), the correlation obtained by Palacios et al. (37), for splash threshold on dry glass surfaces, perfectly separates the two regimes of splashing and deposition for all hydrophobic grain tests in our study. However, in hydrophilic grain tests, this correlation only accounts for the splashing threshold in medium grain and is not valid for fine and coarse sands.

Sloped surfaces promote partial bounce, fragmentation and deposition for hydrophobic sands, while only deposition is observed in the hydrophilic sand tests and drop mainly remains static or stretches slightly. We have shown that the grains size inversely affects the drop mobility in hydrophobic samples. The Wenzel wetting regime of the hydrophobic coarse sand is identified as an opposing factor to the mobility of drop on this surface. Time-displacement graphs further

quantify the post-impact drop motion on different slopes and surfaces made of different size grains, indicating longest and fastest motion down the steep hydrophobic surfaces with fine grains.

Overall, the results lead to the conclusion that the coupled effect of hydrophobicity and grain size plays a significant effect on drops post-impact spread, splash erosion and mobility. It is concluded that the susceptibility of coarse sand to splash erosion is not dominated by the effect of hydrophobicity, while in fine-grain sand hydrophobicity plays a dominant role in the splash erosion threshold and the splash threshold of fine sand decreases significantly when it is hydrophobic. This shows that change in wettability characteristics of finer grain sand can cause more dramatic changes in drop post-impact behavior and thus formation of hydrophobic layer in areas with finer sand can be very dangerous in terms of post-rain events like mudflows. In addition, the higher drop mobility in fine hydrophobic sand contributes to a higher speed of mudflows on this kind of area and results in reduced emergency response time.

Author Contributions

Mahta Movasat: Conceptualization, Methodology, Validation, Formal analysis, Investigation, Writing-Original Draft, Writing – Review and Editing.

Angel Cano de la Cruz: Formal analysis, Investigation.

Ingrid Tomac: Conceptualization, Methodology, Investigation, Resources, Writing – Review, Editing, Project administration, Funding acquisition.

Acknowledgments

4. Effect of spatial variability and granularity of water repellent layer on post-wildfire debris flow initiation mechanism

4.1 Introduction

Water repellency (hydrophobicity) in soil is the reduced affinity of the soil surface to absorb water. When the grain surface free energy dominates the water surface tension, water spreads on the soil surface, and the soil absorbs the water; however, if the grain surface free energy is lower than the surface tension of water, water beads on the soil surface and infiltration does not happen right away (1,6). Soil hydrophobicity leads to preferential surficial fluid flow paths, splash detachment, increased overflow water (1,2,5), and debris flow in post-fire areas (11,120). The Soil water repellency in soils can develop due to various biotic and abiotic reasons. Fatty acids, polar waxes and organic hydrophobic matter produced by fungal activity, plant material, biological activity, and humic acids (1,121,122) are some of the biotic resources of hydrophobicity. Abiotic resources can be wildfires, soil texture, and soil moisture (1,5,123). Factors such as fire severity, exposure duration, organic matter, and vegetation type affect the soil hydrophobicity severity (7). Post-wildfire hydrophobicity has become an important matter since the frequency and duration of wildfires have increased in the past few decades (3). The recently burned areas are more susceptible to debris flow when a rainfall event happens following the wildfire. In addition to hydrophobicity, other factors such as loss of fine roots (124), destruction of expensive clay particles (125), and elimination of soil-stabilizing bacteria and fungi (126) contribute to the increased amount of the erosion. Post wildfire debris flows cause significant economic and environmental loss and can be life-threatening. One of the main reasons that make these incidents even more hazardous is that the debris can trigger in a few minutes after the rainfall starts (127), and also much less rainfall can trigger the debris flow in burned areas compared to the unburned areas (24). In Monterey, CA, a post-wildfire debris flow destroyed at least 20 homes and injured

63

homeowners in January 2021 after the River fire burned east of Salinas in 2020 (128). In San Bernardino national forest, CA, the mudflow was reported as deep as five feet in some areas stranding the cars and leading to highway closures. These areas were earlier burnt with Silverado and Bond fires in 2020 (129). Similar incidents happen in Lake Elsinore, CA which was burnt with Holy fire in 2018. One of the deadly debris flows happened in Montecito, CA in January 2018 after Thomas fire burned the Santa Ynez Mountains three weeks earlier in 2017. The triggered debris traveled down the hill with a velocity of 4 m/s and resulted in 23 fatalities and 408 destructed homes (130). Tiwari et al. (2020) (12) studied the properties of debris flow soil from Montecito debris flow after Thomas fire in California. The debris flow triggered with a short but concentrated rainfall. Loss of vegetation and its replacement with a layer or ash, low permeability and residual shear strength of ash layer are considered the main contributors to the debris flow in this case. Vieira et al (2015) (25) studied 109 records of wildfire and prescribed fire on soil erosion and post fire runoff. The meta-analysis show that fire occurrence is an important factor in erosive process of soil.

Hydrophobic layer thickness, depth, and severity differ from site to site and are a function of fire intensity and duration, the heat produced during a fire, amount of available oxygen during burning, soil water content, and soil physical properties (7,131). Many hydrophobicity scenarios can happen depending on the conditions prior to fire and during a fire. Developing a strong hydrophobicity by burning the former weak hydrophobic layer at or near the soil surface is one of the scenarios observed in pine forests in the western USA. Another scenario observed in hot chaparral fires in the western USA, is the destruction of a strong or weak hydrophobic layer by high surface heating while creating increased hydrophobicity a few centimeters below the surface (132). Scholl et al. (1975) (133) reported that the hydrophobic layer forms in deeper layers during

hot fires, while relatively cooler fires produce a hydrophobic layer in the surficial layer. In addition, experimental studies indicate that pre-fire dry soil leads to a thicker and more serve hydrophobic layer than wet soils (132). Robichaud and Hungerford (2000) (134) observed that under laboratory conditions for Rocky Mountain soil samples at typical wildfire soil profile temperature, hydrophobicity occurs at shallow depth (<2 cm) in dry soil while the hydrophobic layer forms in greater depth in wet soil, which represents the soil conditions in prescribed fires.

A recent study compared the depth and variation of hydrophobicity of samples from two post-fire sites in Virginia and North Carolina over a one-year period (135). While in the lower burn intensity site, hydrophobic soil was prevalent in the surficial layer (0-2 cm depth). In the higher burn intensity location, the hydrophobic layer was found in the sub-surficial layer (2-5 cm depth). Another study in the western USA, Montana (136), reported that about 80 % of a moderate to severe hydrophobic layer was formed up to a depth of 3 cm in relatively dry soil in the burned areas and 1-2 cm below the surface in unburned areas.

Furthermore, rainfall intensity duration thresholds that trigger mudflows are proposed for different areas such as California and Colorado (24,137). Small infiltration-triggered sand slips, progressive entrainment of hillslope material into a runoff, and reduction in shear strength of sand are some of the previously identified mechanisms that lead to post-wildfire mudflows (9,12,13,138,139). Soil erosion models have also been widely used to estimate soil erosion by water. Some of these models, such as Universal Soil Loss Equation (USLE) (140), RULSE (141), Morgan–Morgan–Finney erosion models (MMF) (142), used empirical relations to estimate the erosion, while some other models are physically derived such as READI (143), LandSoil (144) and PESERA (145). However, the post-wildfire erosion is different from a normal agricultural site, and researchers have mostly modified and adapted the above-mentioned models to post-wildfire

areas (146–148). Some of these modifications include the implication of soil burn severity, soil water retention, and increased erosion factor. A thorough study by Lopes et al. (2021) (149) indicates that a minor percentage of the post-wildfire soil erosion models are validated with field data and assessed for uncertainties. Therefore more effort is needed to have a more reliable and general model for post-wildfire areas.

Study on mechanical properties of hydrophobic soils has been performed in a limited number of studies, which yielded consistent conclusions. Results from a ring shear test show that the residual shear strength of ash deposit was less than one-third of the residual shear strength of the soil matrix. Polymer-coated sand shear strength was recently investigated in triaxial tests, which proved the reduction in shear strength (26,27). Additional relevant studies of the mechanical properties of hydrophobic soils used glass beads and artificially made hydrophobic soils (28–30). Byun et al. (2012) (31) investigated the shear strength and stiffness of hydrophobized glass beads by doing a direct shear test and shear velocity test and showed that the shear strength of the hydrophobic sample is lower than the regular glass beads. Shear wave velocity remained constant in the hydrophobic dry sample while increasing in the hydrophilic sample due to the increased interlock of particles during the shear test. In addition, hydraulic properties such as water retention (29,150) splash erosion (81), and water entry pressure (51,150) of hydrophobic soils are studied. Some other studies investigated the hydrological response of the slope over a variety of wettability (151,152). For example, Lourenco et al. (2015) (151) identified different infiltration, with two extremes, water repellent and wettable having the opposite responses. The main processes were identified as retrogressive slides for infiltration-initiated mechanism in wettable sand and erosion and surface runoff for water repellent sand.

Post-wildfire soil properties vary across the soil types and depend on the hydrophobicity level induced by fire types and fuel (7,153). Besides, the change in micro-biological activities and its relation to soil moisture makes hydrophobicity a dynamic property in time and space (14–16). Water repellency destruction due to high temperatures is also reported in some cases in surface layer after fire, contradicting to repellency enhancement in post-fire areas (154). In this study, we focus on the spatial variability and grain size effect of hydrophobic sand on slope processes and the failure mechanism of the slope during rain events with different intensities.

4.2 Materials and Experimental setup

In this study, a three-dimensional acrylic box is built with dimensions of 30x120x20 cm and divided into two flumes. A few holes are drilled in the bottom of the box with a diameter of 0.5 cm and a spacing of 10 cm to help the drainage of the water. At the end side of each flume, an acrylic runoff funnel is attached to collect the water and sand particles. 15 cm out of 20 cm depth of each flume from the bottom is used to prepare the sand layer, and 5 cm remaining part is allocated for runoff observation. Prior to filling the box with sand, the whole box is sprayed with water repellent spray to avoid the preferential flow towards and alongside of the walls. The acrylic box is supported by dynamic steel frames to produce a slope. The frames can be adjusted to increase or decrease the gradient of the slope.

A laboratory-scale rain simulator is designed and built to resemble rainfall and study soil erosion and debris flows. Rain intensity, flow rate, and spatial uniformity are considered the most important factors for controlling rain simulations and investigating surface erosion mechanisms. A 0.95 cm diameter tube connects the nozzle to the pumping system. The pump is a 1/2 horsepower multipurpose electric pump and pumps up to 6.7 m^3/hr and can boost line pressure up to 345 kPa.

A water pressure regulator with a control range of 0-1100 kPa is connected to the pump outlet to control the pressure. The pumping system pumps the water from a 0.160 m^3- capacity tank.

The nozzle used for this experiment is *BETE-WL1* full cone nozzle with a 90° spraying angle. The nozzle is tested for spatial uniformity by locating four rain gauges in the testing area with promising results. The single nozzle sits on a PVC support frame above the center of the acrylic box at 1.2 m. The mean impact velocity of the drops is 4.8 m/s. Rain gauges on both sides of the flumes collect rain from a uniform nozzle spray. A PVC frame is built with 5 cm diameter PVC pipes. The whole system is placed inside the frame. The frame performs as a support for the spraying system. The tube is attached to the frame, and the nozzle is fixed at the center of the frame.

Two layer configurations that are selected for this study (Figure 4.1) aim to show and compare the effect of the hydrophobic layer at the top soil surface and below the soil surface. We focused on the 0-2cm from the soil surface and selected two layouts within this thickness based on the reviewed literature. In the first layout, the hydrophilic base soil is covered with a 2cm hydrophobic soil at the surface (Figure 4.1 left flume in the picture). In the second layout, a 1-cm layer of hydrophobic sand is sandwiched between the hydrophilic base sand and a layer of 1-cm thick hydrophilic sand on the top (Figure 4.1 left flume in the picture). We used 1 cm of the hydrophobic layer thickness for experiments because we assessed this thickness relates to the literature and field data and is not too high regarding the experimental constraints for hydrophobic sand preparation. Furthermore, we hypothesize that 1 cm would suffice to observe erosion, which was confirmed in the first few experiments. For the thickness of the hydrophilic layer on top, we also choose 1 cm to be consistent with the first set of experiments. In addition, we expected the

infinite slope failure in the second setup since the infinite slope has the same factor of safety regardless of the layer thickness.

For future reference, first layout is named hydrophobic top-layer (H-Top) layout. In the second layout, a 1-cm thick hydrophobic layer is at the subsurface layer (1-2cm depth) overlain by a 1cm thick hydrophilic soil at the top surface. This layout is named hydrophobic subsurface-layer (H-Sub) layout. The equal thickness of hydrophobic and hydrophilic also removes the effect of thickness variation in readings of water content sensors. In both layouts, the base hydrophilic sand thickness is 13 cm. In all tests, the left-side flume is filled with the H-Top layout, and the right-side flume is filled with the H-Sub layout. Two water content sensors are embedded in each flume. Two of the sensors are placed under the hydrophobic sand layers (2 cm below the surface), and two other sensors are embedded 1 cm below the soil surface. The sensor layout is shown in Figure 4.1 with small rectangle shapes numbered from 1-4. Later in the results section, water content graphs will follow the same labeling.
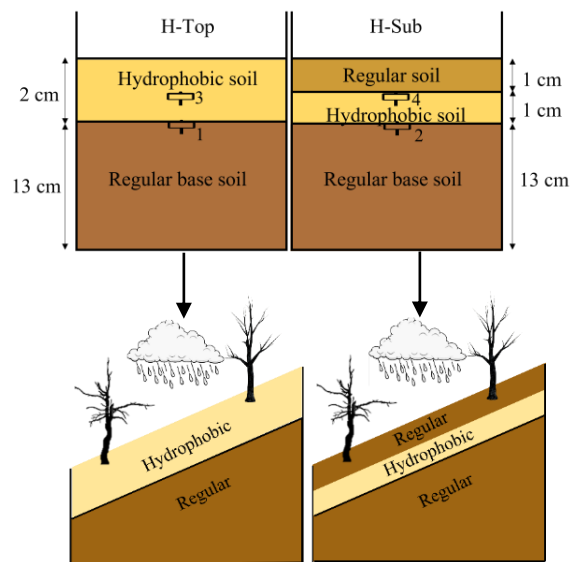
Figure 4.1 Layout of the two flumes, Left flume represents H-Top layout, right flume represents H-Sub layout. Figures in the bottom resemble the H-Top and H-Sub layer layouts in natural hills. The sensors are shown with little rectangular boxes in the sketches.

The experimental setup shown in Figure 4.2 is located in the Geomechanics laboratory of the University of California San Diego. Mudflow investigation in different regions has led to empirical rainfall intensity duration thresholds (137,155,156). Some of the western United States regional rainfall thresholds are gathered in a study by Staley et al. (155). Some of the 15-min thresholds for regions in California, Ventura and Santa Barbara counties (24), Santa Ana Mountains (157), Orange and San Diego counties (155) are reported as 21.8, 18.6, and 30.5 mm/hr, respectively. Right before the triggering of Montecito debris flows, the rainfall intensity reached 50 mm/hr (12). The triggering intensities vary, and it is challenging to determine a threshold; in addition, some field conditions, such as reoccurring rainfalls and windstorms during rainfall, differ from laboratory conditions. In this study, we have selected three rain intensities (18, 70, and 120 mm/hr) and two slope gradients of 20° and 30°. The 18 and 70 rain intensities are selected based on the thresholds, and a higher rain intensity of 120 mm/hr is chosen as an extreme condition. Sensor layout and embedment depths are shown in Figure 4.3.
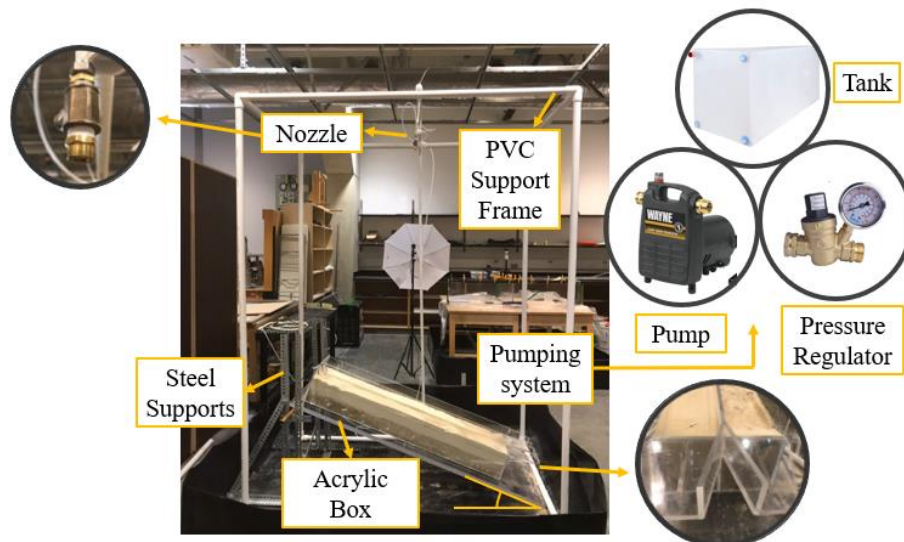
Figure 4.2 Experimental setup of the rain simulation experiment.
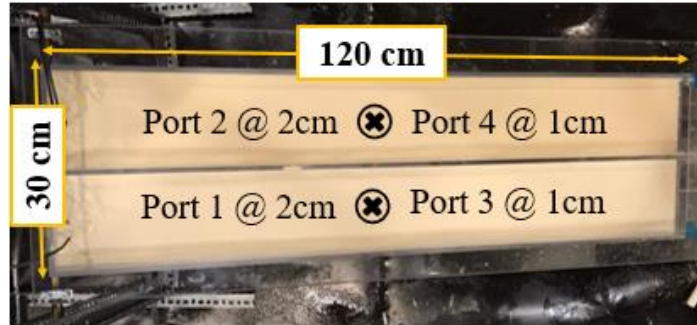
Figure 4.3 Sensor layout

Three different batches of sand with different grain sizes are used to observe the effect of grain size in the experiments. The grain size distribution of each fine, medium and coarse grain sand is shown in Figure 4.4. The fine sand is Ottawa F-65 silica with round particles, and the medium and coarse sands are sub-angular clean silica.
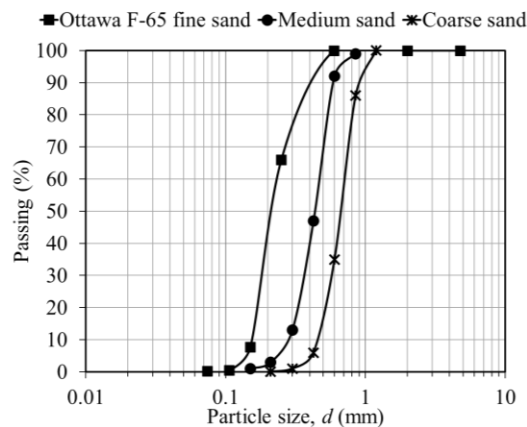
Figure 4.4 Grain size distribution of fine, medium, and coarse sands

4.3   Results and discussion

The duration of each rainfall experiment is sixty minutes. Each flume's discharge and eroded soil are collected in 10-minute intervals to understand better the onset and time evolution of erosion and slope failure. The four main variables in the experiments are grain size, hydrophobicity, rain intensity, slope gradient, and layer layout. The water content is recorded and monitored at four points during the tests.

71

4.3.1 Hydrophobic top-layer (H-Top) layout:

The soil surface and erosion process are monitored during the experiments in both flumes. In this section, the results for the flume with H-Top layout will be discussed. The surficial evolution is shown in Figure 4.5 for three fine, medium, and coarse grain sands under 120, 70, and 18 mm/hr rain intensities (*RI*). Figure 4.5(a) and (b) show the surficial evolution of the three fine, medium, and coarse sand with rain intensities of 120 and 70 mm/hr, respectively. In both rain intensities, the erosion process starts immediately on fine slope after the rain begins. Small sequin shape patches erode from the surface of the fine hydrophobic sand as soon as raindrops hit the surface, and gradually as rain continues, these small erosion patches coalesce.

On the contrary, in medium and coarse hydrophobic flumes, the observable surficial patterns start to form later than in fine sand, and channels form on the surface instead of sequin shapes. The channels are more visible and wider in coarse than medium soil. The channels provide a preferential path for surficial water flow. In lower rain intensity (Figure 4.5 (c)), the erosion pattern in medium and coarse sand is like fine sand, and the surface erodes as small sequin-shaped spots. These patterns are less visible in coarse sand, and the surface looks bumpy at the end of the test.

(a) *RI*= 120 mm/hr
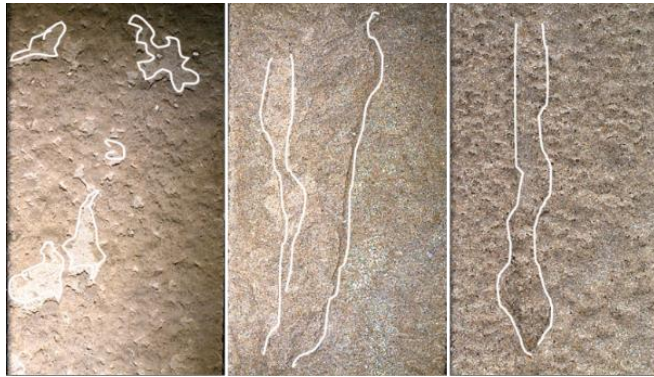
(b) *RI*= 70 mm/hr

(c) *RI*= 18 mm/hr

Figure 4.5 Surficial evolution in fine (left), medium (middle), and coarse (right) hydrophobic sand, where *RI* is the rain intensity.

4.3.1.1 Rain intensity and slope gradient effect on water discharge

Figure 4.6 and Figure 4.7 show the discharge measurements for three hydrophobic sands in H-Top layout. Three rainfall intensities (*RI*) of 120, 70, and 18 mm/hr are performed on flumes with 20° and 30° gradients, and the overflow water and eroded soil mass are collected in 10-minute

73

intervals. The water discharge (q) is the collected overflow water per projected unit area of the flume per minute. The water content of the sand is also recorded with water content sensors and shown on the graphs as solid lines along with the discharge amounts. Figure 4.1 and Figure 4.3 shows the sensor layout. This section shows the data from sensor 3, which is placed beneath the hydrophobic layer.

Overall, the discharge in each sand type decreases by decreasing the rain intensity. The water content values are very low in experiments due to the impediment of water by the surficial hydrophobic layer. The peak discharge for all fine, medium and coarse sand happens in the first 10-minute interval in tests with the highest rain intensity ($RI = 120$ mm/hr).

Figure 4.6 (a) and Figure 4.7 (a) show the water discharge and water contents for rain intensity of 120 mm/hr for slopes with gradients of 30° and 20°. In the 30° slope, the fine sand has about 30% higher discharge amount ($q=2.0$ lit/m^{2}min) in the first 10-minute interval compared to medium ($q=1.53$ lit/m^{2}min) and coarse ($q=1.475$ lit/m^{2}min) sands. The amount of discharge decreases gradually as rain continues, and water starts to infiltrate as soil erodes from the surface as sequin shape patches. The water content increase is negligible at the beginning of the test; however, the values start to increase after 20 minutes and rise to 8% at the end of the test. It can be concluded that at the beginning of the test, the fine sand has an intense resistance to infiltration and has a high discharge; however, after the surface starts to erode, water infiltrates, and water content increases (a black arrow on the graph shows this shifting point). In the medium sand test, water discharge decreases gradually after the first 20 minutes, and the water content starts to increase after 10 minutes and reaches 7% at the end of the test (Fig 4.6(a)). The water content in coarse sand increases to 5.3% in the first 10 minutes of the rain. Although the water contents are very low values, it is worth mentioning that infiltration starts faster in coarse sand than medium

74

and fine sand, which can be attributed to larger pores and lower water entry value. However, the fine and medium sand water content increase later after the overflow erodes the surficial sand grains.

In the 20° slope, the same trend of infiltration is observed. The fine and medium sand has the highest discharge in the first 20 minutes of the test, and this amount decreases after 20 minutes (Fig 4.7(a)). The infiltration starts earlier in coarse sand and goes up to 3.5%. The infiltration in medium and fine sand starts later and increases suddenly, which is related to the eroded soil particles from the surficial layer. The erosion in fine sand begins as small patches from the surface and continues homogenously until patches coalesce, while in medium sand, channels form on the surface, and water reaches the bottom of the layer faster since a preferential path is developed. The observed morphological patterns explain the delayed infiltration in fine compared to the medium sand in the tests. In addition, fine sand has a higher water entry value, and it is shown in former studies (158) that a higher suction air entry is required for finer grains.

In tests with a rain intensity of 70 mm/hr (Figure 4.6 (b) and Figure 4.7 (b)), the peak water discharge is between 0-10 min for fine and medium sand and 30-50 min for coarse sand. In addition, the amount of water discharge changes smoothly during the intervals for both 20° and 30° slopes, and no abrupt changes are observed. The water contents of each sand at 20° and 30° slopes are approximately the same. In coarse sand, water contents reach 3% right after the rain starts. In medium and fine sand, water content increases in two steps, where the first increment is negligible, and the second increment is more noticeable. The second increment occurs faster in medium sand than in fine sand and follows the same trend as discussed for the 120 mm/hr rain intensity.

By decreasing the rain intensity to 18 mm/hr, the water discharge is less affected by the grain size, such that the amount of water discharge is almost steady throughout the experiment for all sand types. The water contents for 30° and 20° slopes (Figure 4.6 (c) and Figure 4.7 (c)) are about 2.5~3% for coarse and 1.3~1.8% for medium and fine sands. This indicates that no significant erosion has happened during the tests.

(a)

(b)

(c)
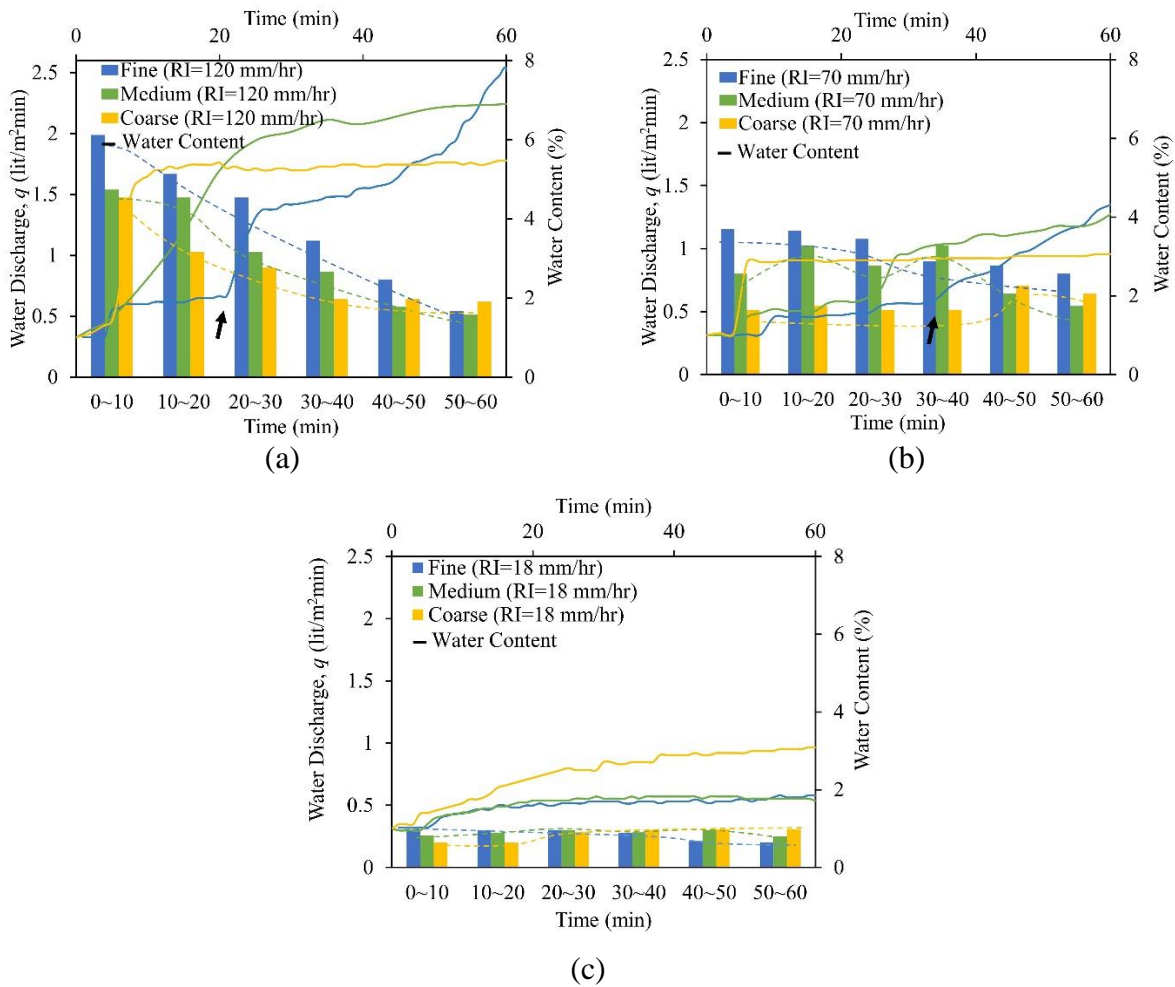
Figure 4.6 Water discharge versus time and water content graphs for (a) 120, (b) 70, and (c) 18 mm/hr on 30° slope. The black arrow indicates the major change in water content.
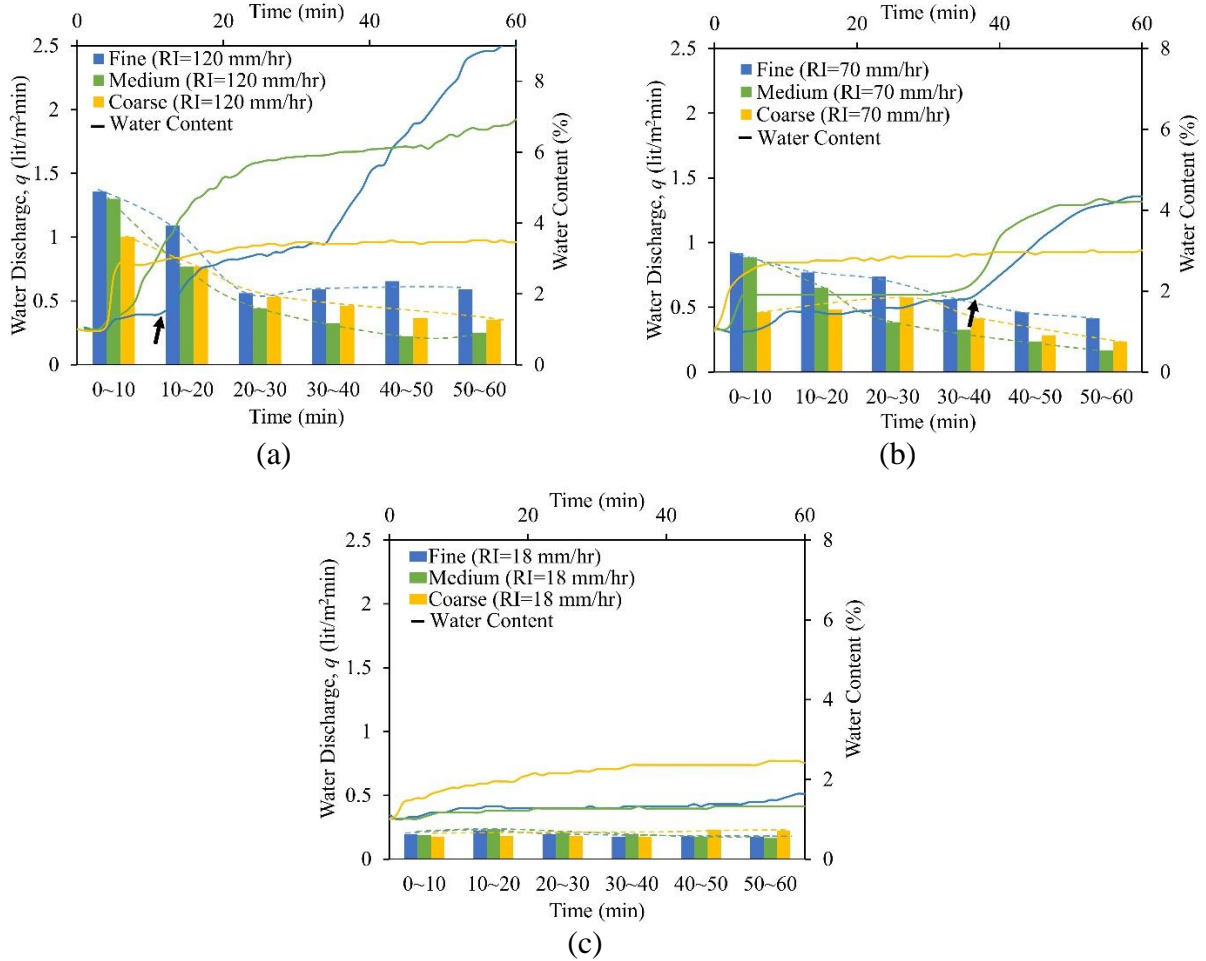
Figure 4.7 Water discharge versus time and water content graphs for (a) 120, (b) 70, and (c) 18 mm/hr on 20° slope. The black arrow indicates the major change in water content.

Figure 4.8 shows the cumulative discharge for different rain intensities for 60 minutes. In both 30° and 20° slopes for higher rain intensities (120, 70 mm/hr), the 60-minute cumulative water discharged from the fine-grain flume is more considerable than water discharge from medium and coarse grain tests. By decreasing the rain intensity to 18 mm/hr (Figure 4.8 (c)), the effect of grain size diminishes, and all three sands have similar total cumulative discharge at the end of the 60-minute experiment. It is concluded that in higher rain intensities, a coupled effect of grain size and slope gradient affects the discharge, while in lower rain intensity, the slope gradient dominates the grain size effect.

77
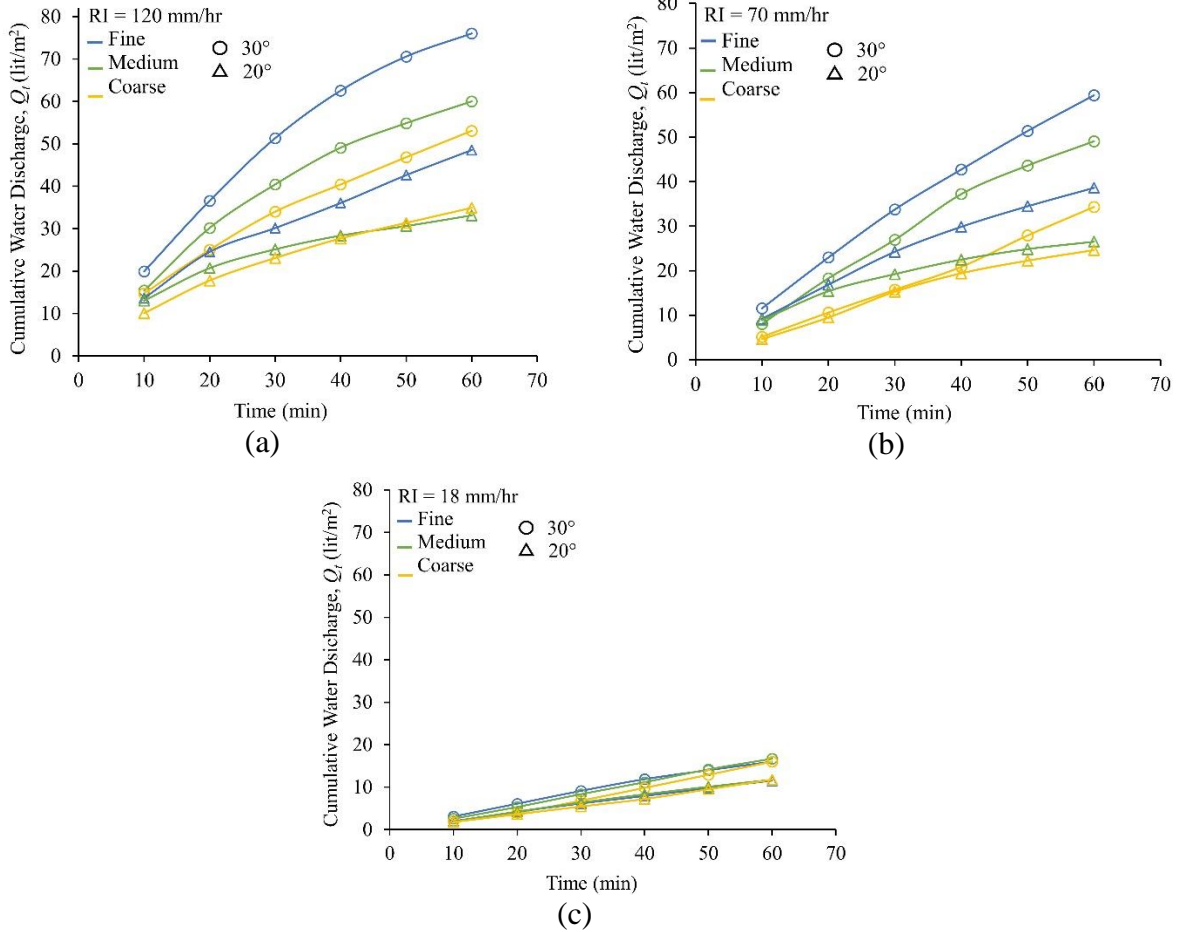
Figure 4.8 Cumulative water discharge versus time graphs for (a) 120 mm/hr (b) 70 mm/hr and (c) 18 mm/hr rain

The water discharge (q) and cumulative water discharge (Q_t) amount results are discussed for different rain intensities. At each time interval, the water discharge (q) is normalized with respect to the total amount of received rain and named normalized water discharge (q_n). The remaining percentage is the percentage of infiltrated water. The graphs in Figure 4.9 show the discharged and infiltrated portion of the total rain and the overall sand behavior while eliminating the quantitative amounts.

In fine sand, all normalized discharge curves have a negative slope (Figure 4.9 (a)) and overall have a higher discharge in the 30° than 20° slope. On the 30° slope, the normalized

discharge in fine sand is approximately 97% at the beginning of the test, regardless of the rain intensity, and approximately between 61-75% on the 20° slope. In conclusion, the fine sand has the highest discharge irrespective of the rain intensity in the first 10-minute interval. The normalized discharge is almost close to 100% in the 30° slope, which indicates almost all the received rain flows over the surface. The normalized discharge reduces gradually during the test; however, in low rain intensity RI=18 mm/hr the reduction is imperceptible, and a higher steady normalized discharge is received throughout the test compared to higher rain intensities on the same slope.

In medium sand, the initial normalized discharge is between 70-80% for the 30° slope and 60-70% for the 20° slope (Figure 4.9 (b)). The initial normalized medium sand discharge decreases for the 30° slope compared to fine sand, while the change is subtle for the 20° slope. The same high and steady normalized discharge trend is also observed in medium sand at the lowest rain intensity. Both fine and medium sand have the most declivity in normalized discharge amount when rain intensity is 120 mm/hr. Although the amount of received rain is low in low rain intensity, a higher and steady percentage of the received rainwater flows as discharge, and infiltration is low throughout the test. In higher rain intensity, the overall amount of discharge is high due to the higher amount of rainwater received by the flume; however, by normalizing the discharge amount with respect to the total received rainwater by the flume, it is shown that a higher percentage of received water discharges from the surface at the beginning of the test, and it declines extremely afterward.

In coarse sand, an upward trend is observed for low and medium rain intensity RI=18 and 70 mm/hr, while normalized discharge gradually reduces in high rain intensity (RI=120 mm/hr) (Figure 4.9 (c)). At the same rain intensity, normalized discharge is higher for the 30° slope.

Overall normalized discharge at the beginning is lower in coarse than medium and fine sand tests at the same rain intensity and slope. Similarly, the water contents in coarse sand increase immediately as rain starts, and remain constant after a while.

(a)

(b)

(c)
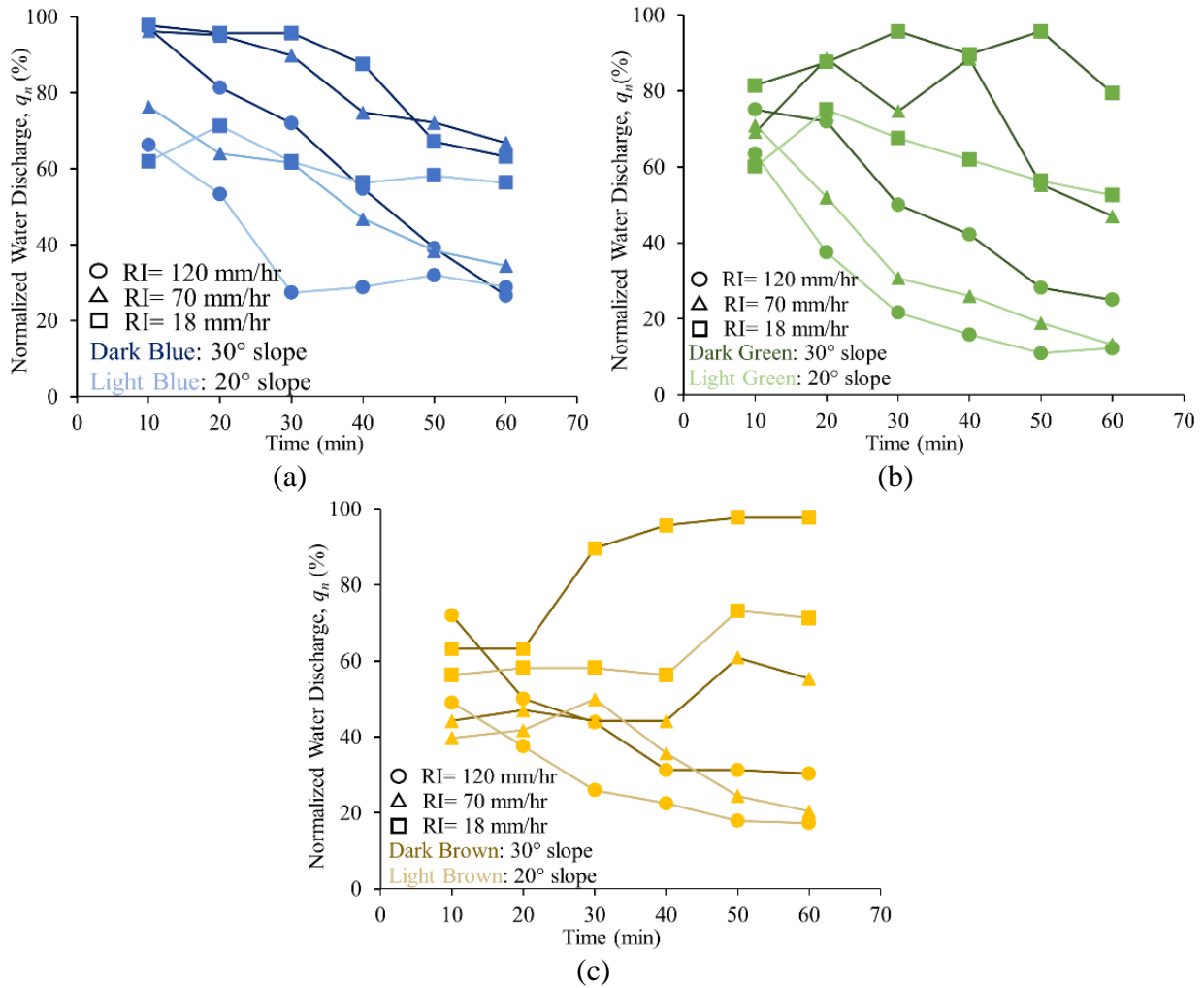
Figure 4.9 Normalized water discharge for (a) fine, (b) medium and (c) coarse sand

Figure 4.10 (a,b) show the peak (q_p) and total discharge (Q_t) for different rain intensities. It is shown that the peak and total overflow are almost the same for all three grains at the lowest rain intensity and increase by increasing the rain intensity. Figure 4.10 (b) indicates that as rain becomes more intense, the fine sand experiences the most increase in total discharge. It is

concluded that the grain size plays an essential role in the amount of discharge water, and this effect becomes more prominent at higher rain intensity.

The time to peak discharge for different rain intensities are compared in Figure 4.10 (c). In higher rain intensity, the peak discharge occurs in the first ten-minutes of the test regardless of grain size. Time to peak discharge increases by lowering rain intensities, especially in medium and coarse sands. In Figure 4.11 the effect of slope gradient on the peak overflow in different grain sizes is noticeable in fine sand, while it is not as effective in medium and coarse sands.

(a)

(b)

(c)
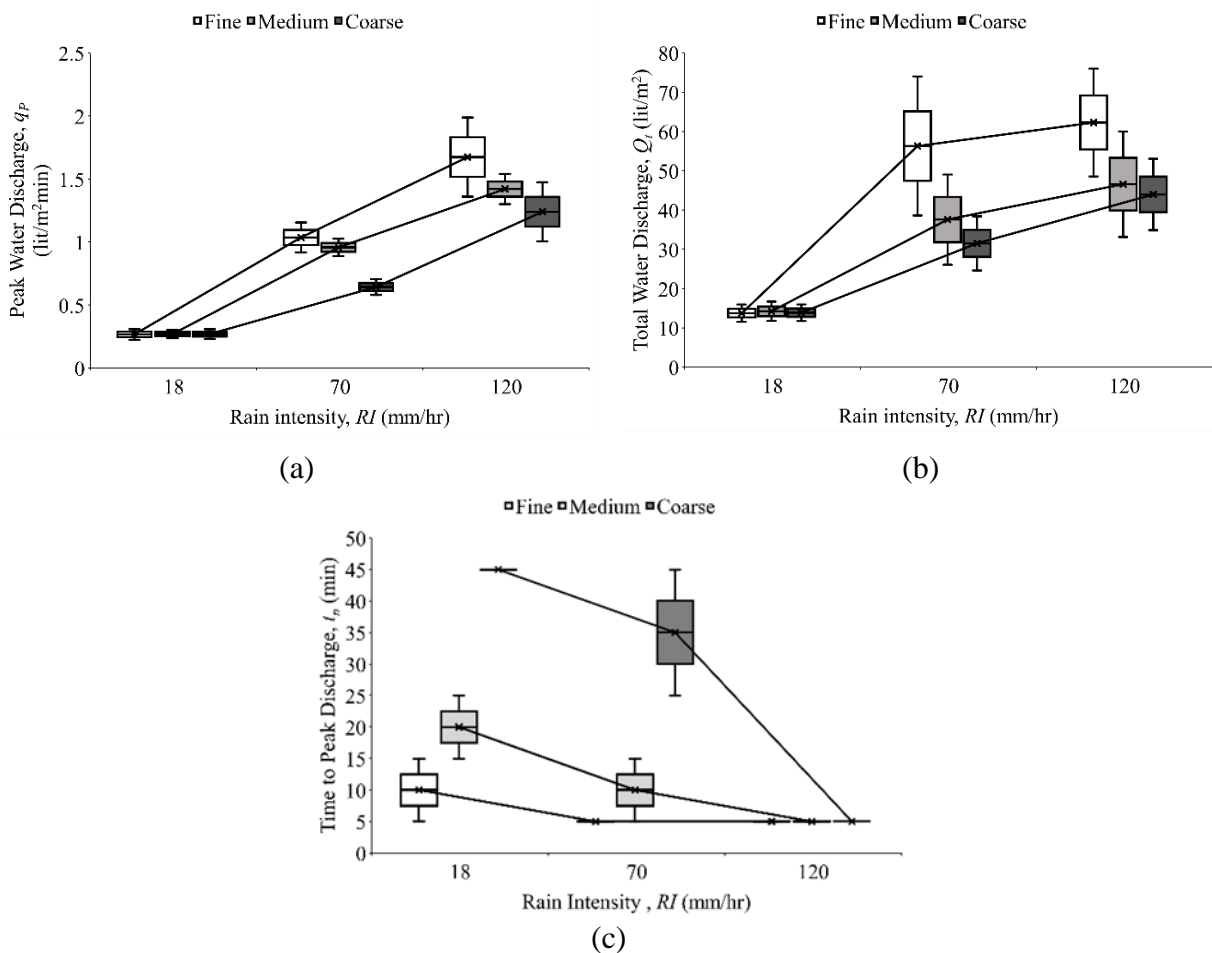
Figure 4.10 (a) Peak water discharge, (b) total water discharge and (c) time to peak water discharge versus rain intensity for fine, medium and coarse sand
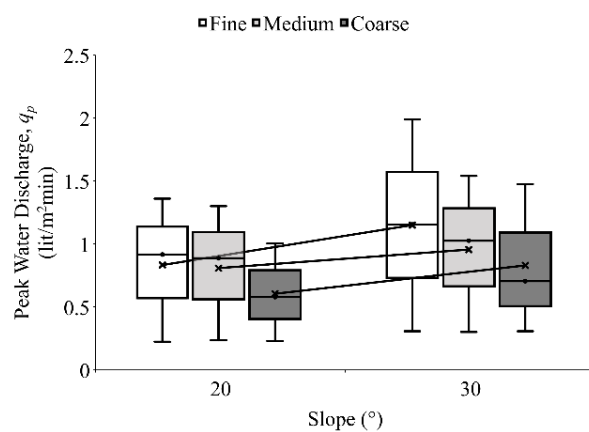
Figure 4.11 Peak water discharge versus slope gradient graph for fine, medium, and coarse sand

4.3.1.2   Rain intensity and slope gradient effect on particle erosion

Figure 4.12 and Figure 4.13 show the erosion rate of sand for 10-minute intervals. The erosion rate is calculated per minute by dividing the amount of the eroded sand in each 10-minute interval by the projected unit area of the flume. It is observed that the amount of erosion is subtle in coarse sand compared to fine and medium sand tests. The highest erosion rate of coarse sand is collected within the first 10 minutes of the tests with 120 mm/hr rain intensity, which is about 90 gr/m^{2}min and 54 gr/m^{2}min in 30° and 20° slopes, respectively (Figure 4.12 (a) and Figure 4.13 (a)). The water content for coarse sand (Figure 4.6(a) and Figure 4.7(a)) is about 5.4% and 3.5 % for 30° and 20° slopes. The 50% increase in water content of the 30° slope could be related to the 30% higher amount of eroded soil in the first 10-minutes of the test.

In all tests, the erosion rates decrease steadily as rain continues. However, in the tests with rain intensities of 120 and 70 mm/hr, a sudden drop in erosion rate occurs in the medium sand after 20~30 minutes of rain (Figures 4.12 and 4.13 (a,b)). This abrupt change can be attributed to the channel formation in medium grain sand during this period. After the channel forms, water prefers to flow in the channel, and the erosion rate reduces since the water starts to flow in the channel,

and the whole surface is not impacted as if the channel did not exist. In fine sand, the erosion rate steadily decreases during the rain, and an overall higher cumulative eroded sand is collected at the end of the test.

(a)

(b)

(c)
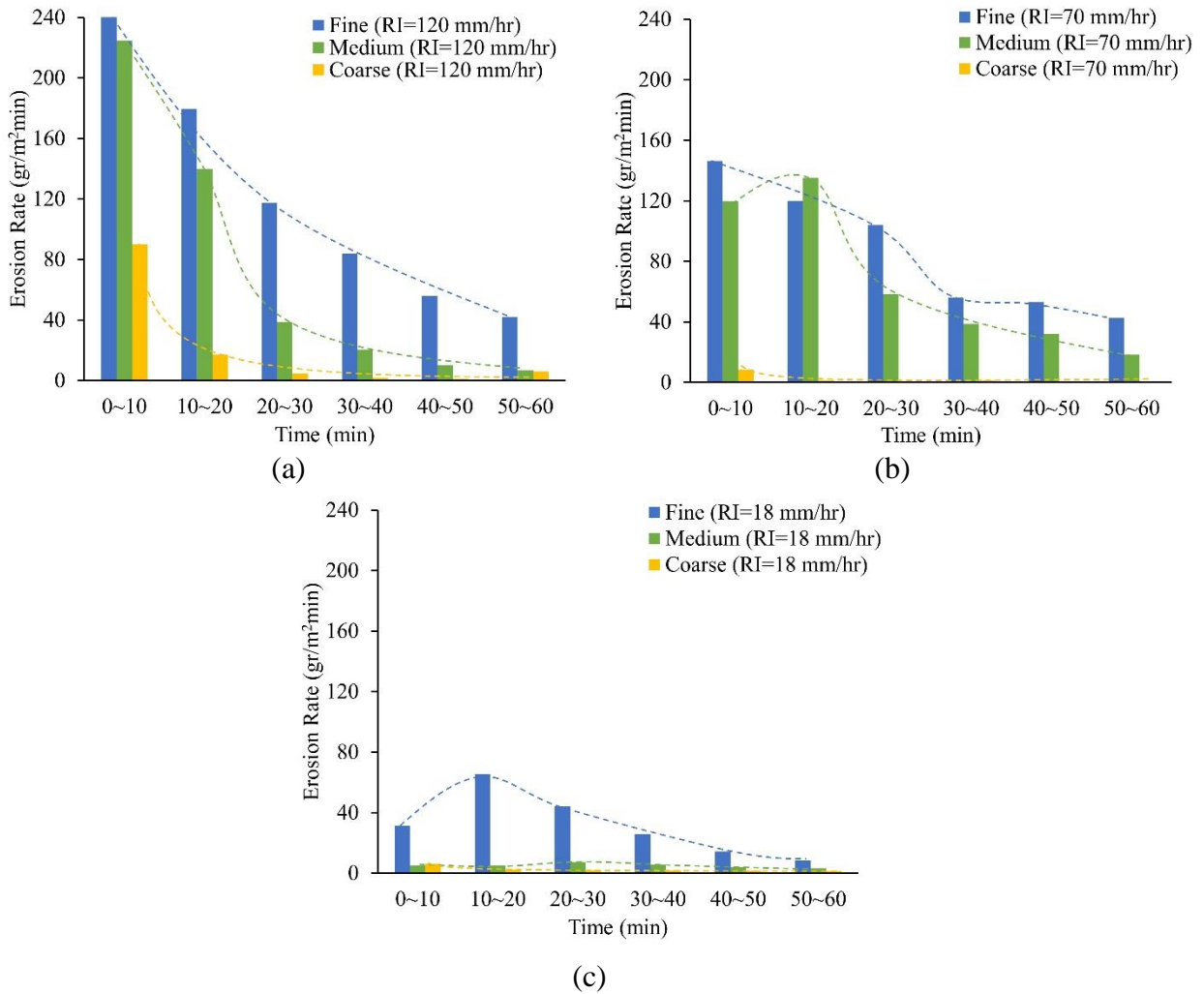
Figure 4.12 Erosion rate versus time graphs for (a) 120, (b) 70, and (c) 18 mm/hr on 30° slope
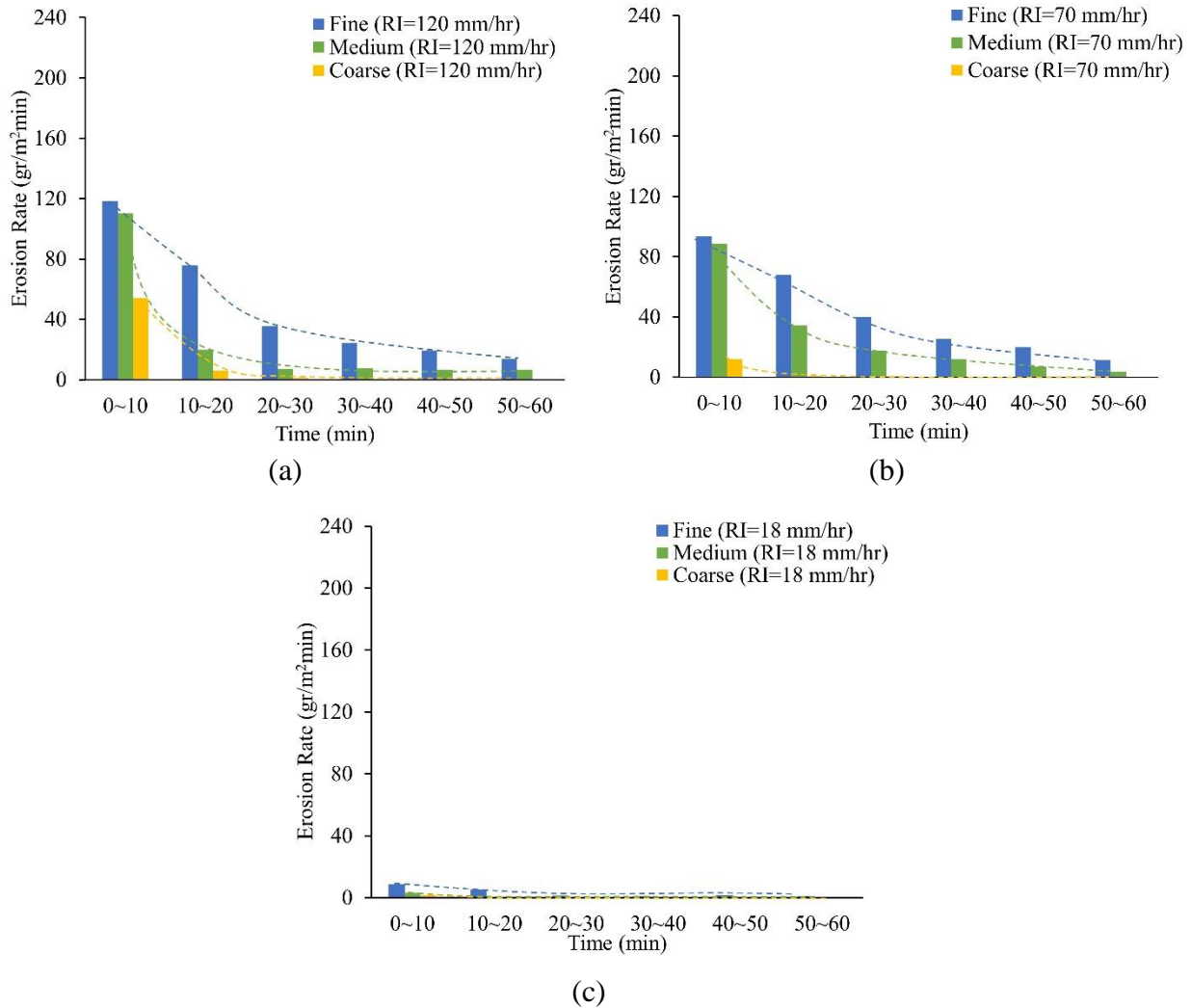
Figure 4.13 Erosion rate versus time graphs for (a) 120, (b) 70, and (c) 18 mm/hr on 20° slope

Figure 4.14 shows the cumulative erosion per projected unit area for different rain intensities during 60 minutes. It is shown that fine sand has the highest amount of erosion than medium and coarse sand on the slope with the same gradient. For the rain intensity of 18 mm/hr, the amount of erosion in both slope gradients is very low regardless of the grain size. Figure 4.14 (a) shows that on a 20° slope, the difference between the cumulative erosion for each sand type is very low, and it is not strongly affected in higher rain intensities (120 and 70 mm/hr). The intensity of rain plays a more significant role in erosion on steeper slopes. By decreasing the rain intensity from 120 to 70 mm/hr, the total final amount of erosion on the 20° slope decreases about 10% and

1% in fine and medium sands, respectively (Figure 4.14(a)). However, this difference increases to 27% for fine and 10% for medium sand when the rain intensity changes from 120 to 70 mm/hr on the 30° slope (Figure 4.14(b)). It is concluded that on the 30° slope, coupled effect of grain size and rain intensity is affecting the erosion intensity. However, the effect of rain intensity diminishes on the 20° slope, and grain size dominates the erosion process.
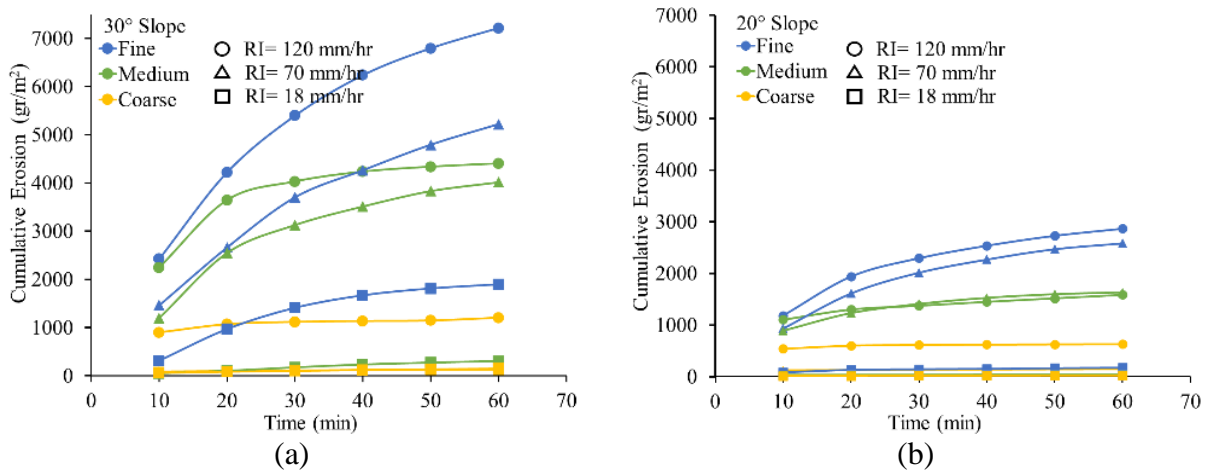
Figure 4.14 Cumulative erosion per projected unit area versus time graphs for (a) 20° slope (b) 30° slope

The peak erosion rate and total erosion is shown for different rain intensities in Figure 4.15. The results indicate that the peak erosion rate increases in all fine, medium, and coarse grain sands by increasing the rain intensity (Figure 4.15 (a)). However, the fine and medium sands are more sensitive to changes in rain intensity. In addition to rain intensity, slope gradient greatly affects the peak erosion rate in fine and medium sand while it has a minimum effect on the peak erosion rate of coarse sand (Figure 4.16 (a)). The total amount of erosion for different rain intensities and slopes are shown in Figure 4.15 (b) and Figure 4.16 (b). The total amount of erosion increases by increasing the rain intensity and slope gradient, and both have a greater impact on the erosion of fine and medium rather than coarse sand. Figure 4.17 shows that the fine sand has the highest total erosion, and it decreases by increasing the grain size.
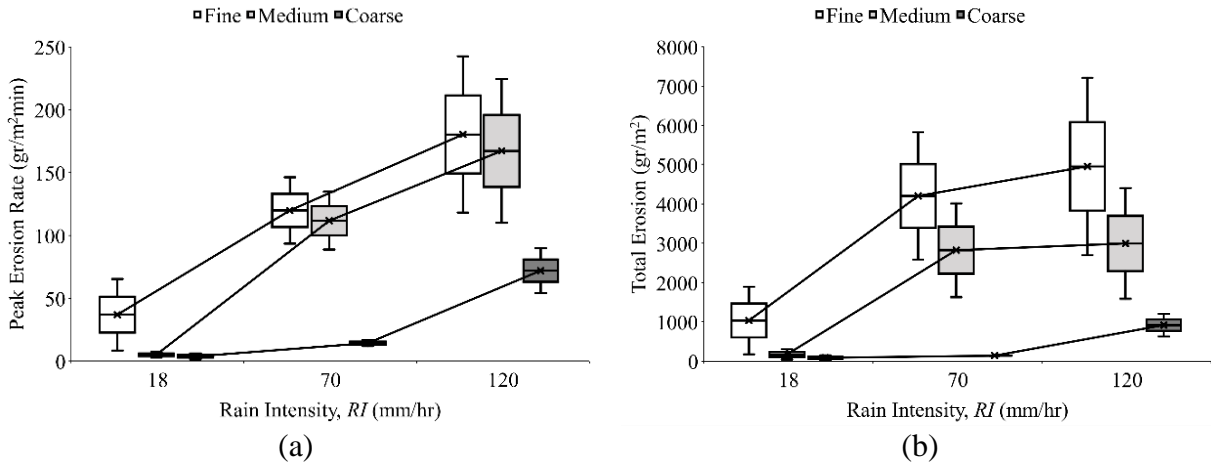
Figure 4.15 (a) Peak erosion rate and (b) total erosion versus rain intensity for fine, medium and coarse sand
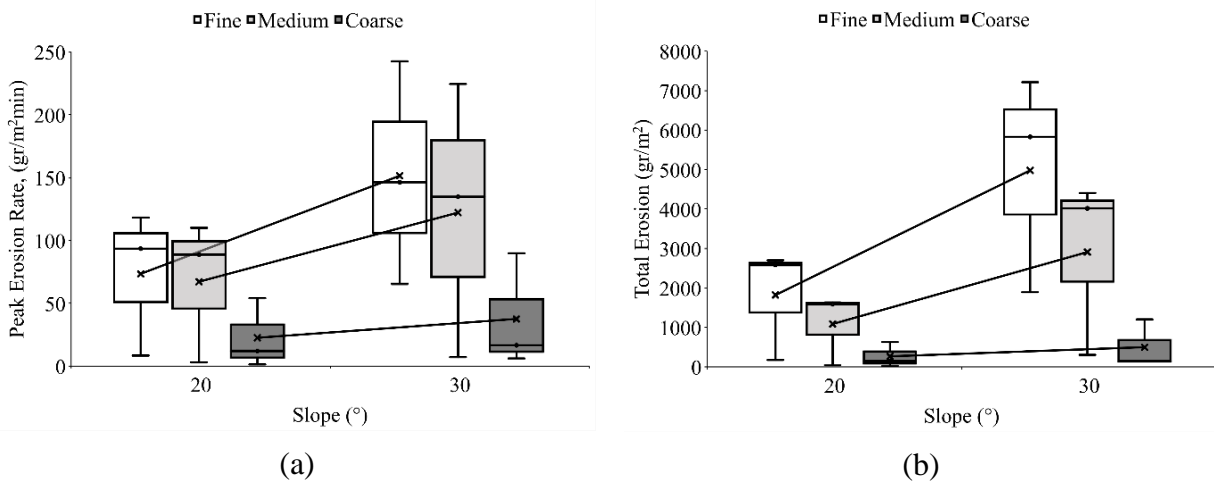
Figure 4.16 (a) Peak erosion rate and (b) total erosion versus slope gradient for fine, medium and coarse sand
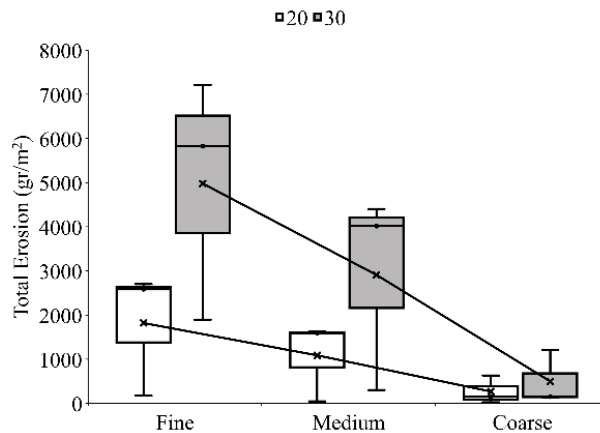
Figure 4.17 Total erosion versus grain size for 20° and 30° slopes

4.3.2 Hydrophobic subsurface-layer (H-Sub) layout:

This section presents the results for the flume with H-Sub layout, in which a 1-cm thick hydrophobic layer of sand rests below the 1-cm thick regular sand. In these experiments, surficial erosion is no longer the dominating process, and infinite slope failure is identified as the main failure mechanism. Figure 4.18 (a) shows fine, medium and coarse sand flumes during the rain and the failure moment for fine and medium slopes. Figure 4.18 (b) shows the failure boundary with red lines for fine and medium slopes after the failure occurred. The infinite failure occurs once the top sand layer slides down the fine and medium sand slopes, while the coarse slopes did not fail during the experiments.

| Fine | Medium | Coarse | Fine | Fine | Medium |

(a)   (b)
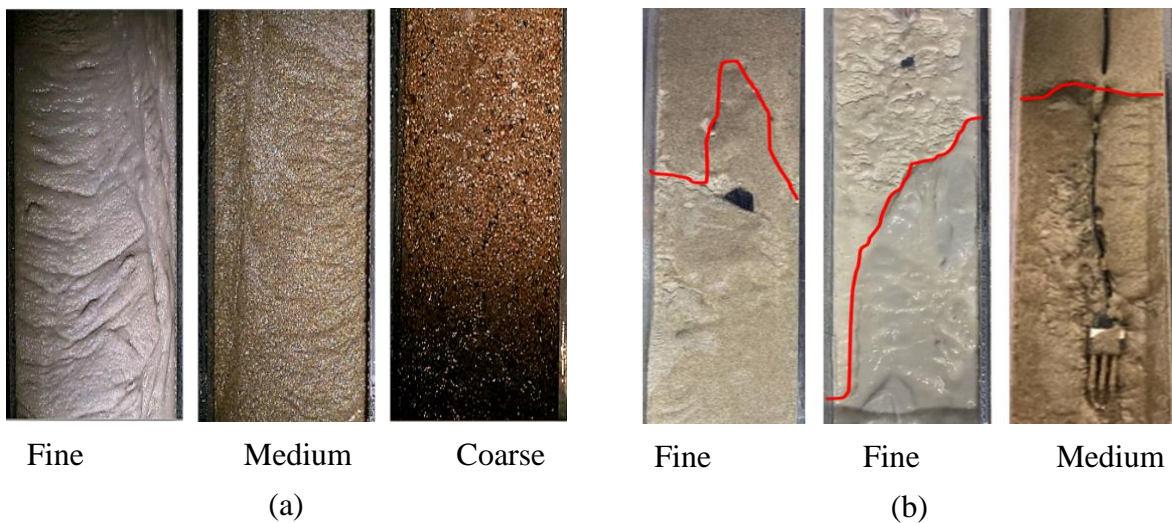
Figure 4.18 Failure mechanism in H-Sub tests, (a) fine and medium slopes fail while in coarse slope no failure occurs (b) More pictures of the failed fine and medium slopes.

4.3.2.1 Rain intensity and slope gradient effect on discharge and particle erosion

Figure 4.19 and Figure 4.20 summarizes the water discharge and water content of fine, medium, and coarse sand for 20° and 30° slopes, respectively. The water content values for two sensors (4 and 2) are shown with solid lines. Sensor 4 is placed right under the regular sand (shown with darker shade solid lines), and sensor 2 is placed under the hydrophobic layer (shown with

lighter shade solid lines). Water discharge amounts increase with increasing the rain intensity and the slope gradient. The water content amount increases by increasing the rain intensity. Overall, the water contents are slightly smaller at 30° slope, which can be due to the steeper slope and higher discharge at 30° slope. In addition, the water content values of sensor 4, which is right at the boundary of regular and hydrophobic layers, show slightly higher values for fine sand; on the other hand, sensor 2, shows slightly lower values for fine than medium and coarse sands. The hydrophobic fine sand layer is more resistant to water infiltration than medium and coarse sand, and this entraps a slightly higher amount of water in the upper regular layer.

In 20° slope, infinite slope failure happens at RI = 120 mm/hr in fine and medium sand slope in the first 10 minutes of rain (Figure 4.19 (c)). The water content at which the failure triggers (indicated with stars on the water content graphs) is about 4% in fine and 9% in medium sand. In 30° slope tests, the infinite failure happened in fine sand for all rain intensities. The failure triggers when the water content at the bottom of the regular fine sand layer reaches 11% at rain intensity of 18 mm/hr, and 4% and 3.5% at rain intensities of 70 and 120 mm/hr, respectively (Figure 4.21 (a-c)). The infinite failure for medium sand at 30° slope occurred at 70 mm/hr and 120 mm/hr rain intensities with 12.5 and 8.5% water contents, respectively. The coarse sand did not fail under any tested rain intensity or slope gradient.

The water content results show that the failure triggers at low values. We also observe an increase in the water content values of sensor 2, after the infinite slope failure initiates in the upper layer, which means the hydrophobic layer starts to erode after the collapse of the upper layer. The sudden increase of the water contents beneath the hydrophobic layer suggests that the infinite failure could also affect the underlying hydrophobic layer and possibly drag a surficial layer of the hydrophobic layer. Soil erosion rates are shown for each of the tests (Figures 4.20 and 4.22). The

88

coarse sand has a negligible rate of erosion in all tests, and the water infiltrates at the beginning of the raining. The water content of the coarse sand varies between approximately 10~17% by increasing the rain intensity from 18 to 120 mm/hr, which indicates the higher water infiltration in coarse sand without having any failure.
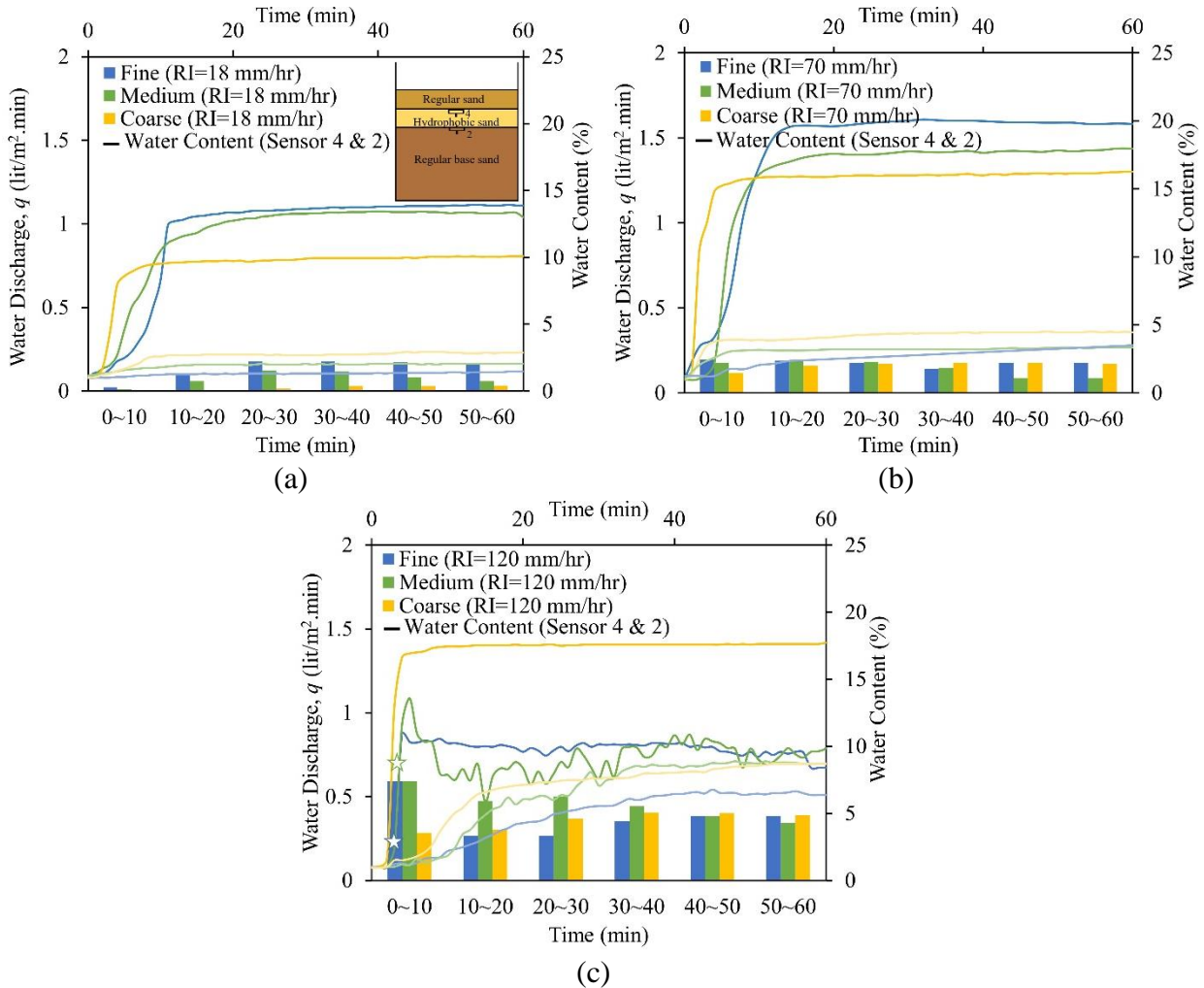
Figure 4.19 Water discharge versus time and water content graphs for (a) 18, (b) 70, and (c) 120 mm/hr on 20° slope. The darker solid lines indicate the water content measured by sensor 4 and lighter lines show the water contents of sensor 2. (Sensor layout is shown in Figure 4.19(a))
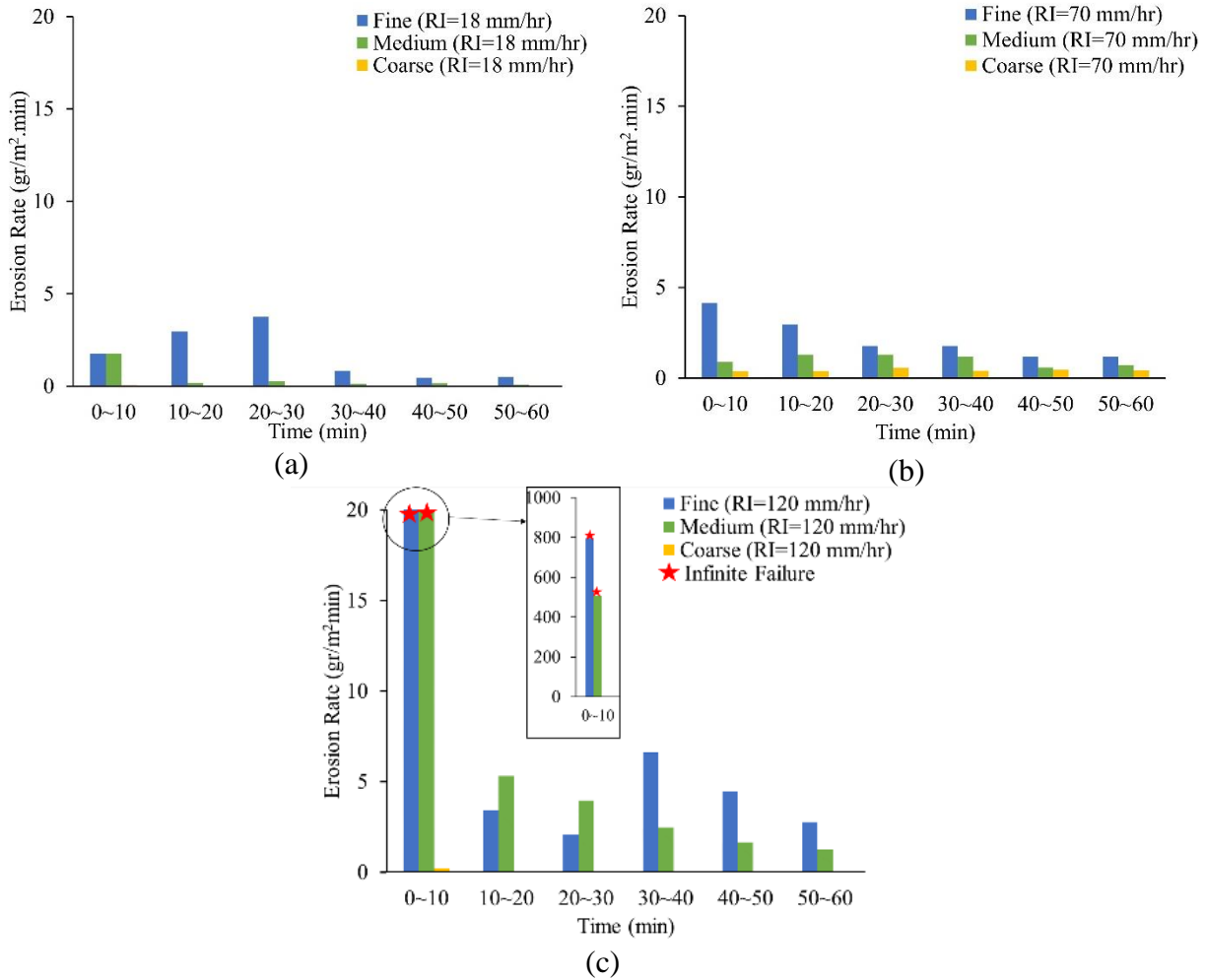
Figure 4.20 Erosion rate versus time for (a) 18, (b) 70, and (c) 120 mm/hr on 20° slope.
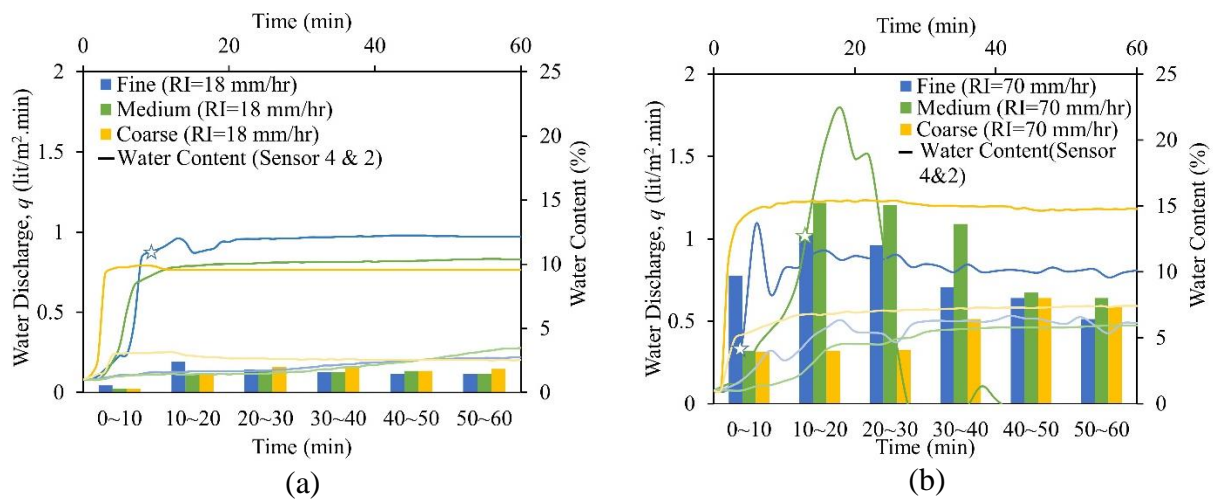
Figure 4.21 Water discharge versus time and water content graphs for (a) 18, (b) 70, and (c) 120mm/hr on 30° slope. The darker solid lines indicate the water content measured by sensor 4 and lighter lines show the water contents of sensor 2. (Sensor layout is shown in Fig.4.19(a))

(c)
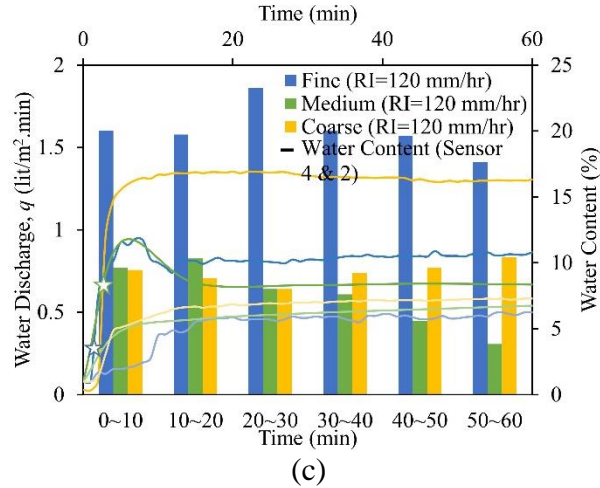
Figure 4.21 Water discharge versus time and water content graphs for (a) 18, (b) 70, and (c) 120mm/hr on 30° slope. The darker solid lines indicate the water content measured by sensor 4 and lighter lines show the water contents of sensor 2. (Sensor layout is shown in Fig.4.19 (a)), continued.

(a)

(b)

(c)
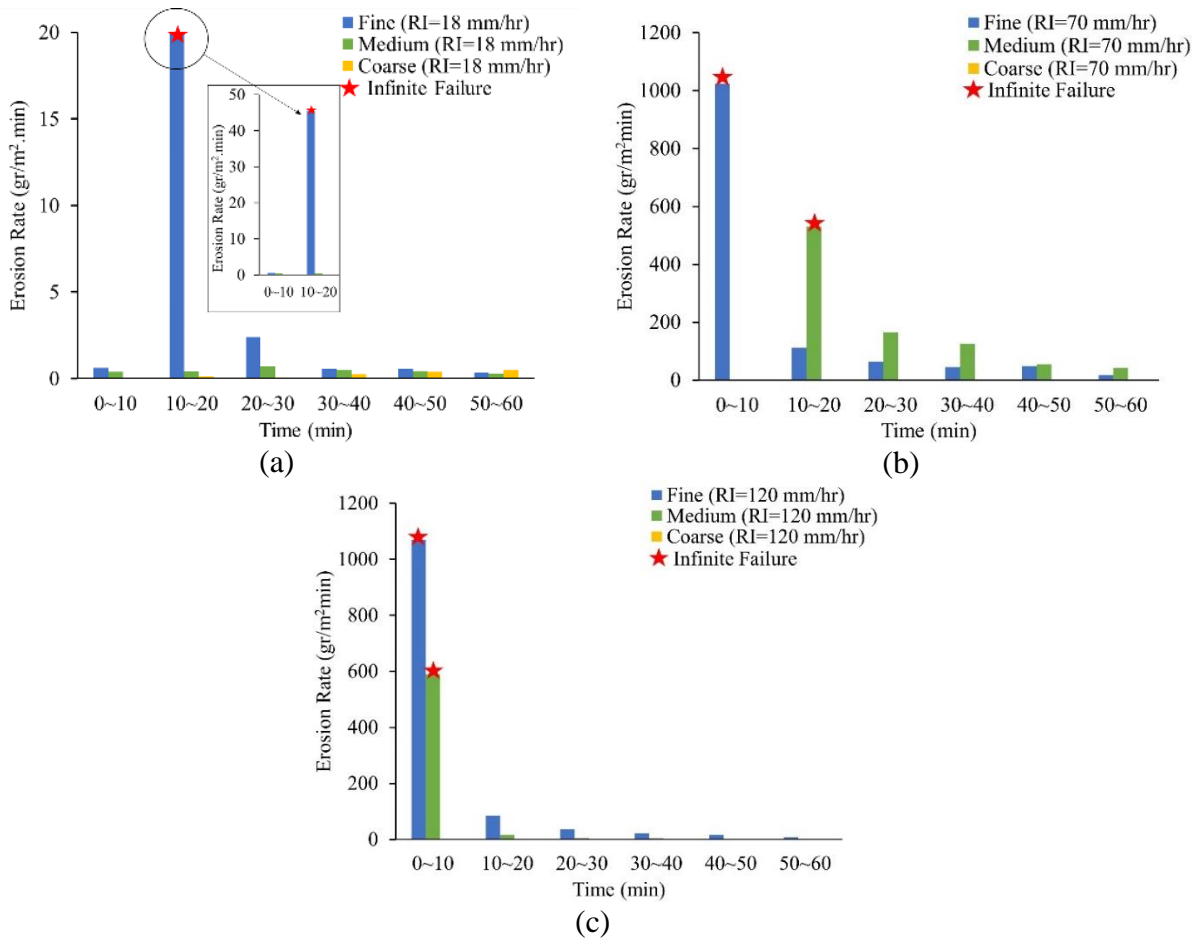
Figure 4.22 Erosion rate versus time for (a) 18, (b) 70, and (c) 120mm/hr on 30° slope.

91

In H-Sub layout, the initial normalized discharge (Figure 4.23) is overall much lower than the H-Top layout cases. The initially two high cases are the fine sand with 120 and 70 mm/hr rain intensity on a 30° slope that fails within a few minutes of rainfall (Figure 4.23 (a)). The red stars show the failure moments on the graphs.

In all sands, when RI=18 mm/hr, in the first 10-minute interval, discharge is 10% of the total received rainfall, and this amount goes as high as 40-50% at the end of one hour for 30° slopes.

(a)   (b)

(c)
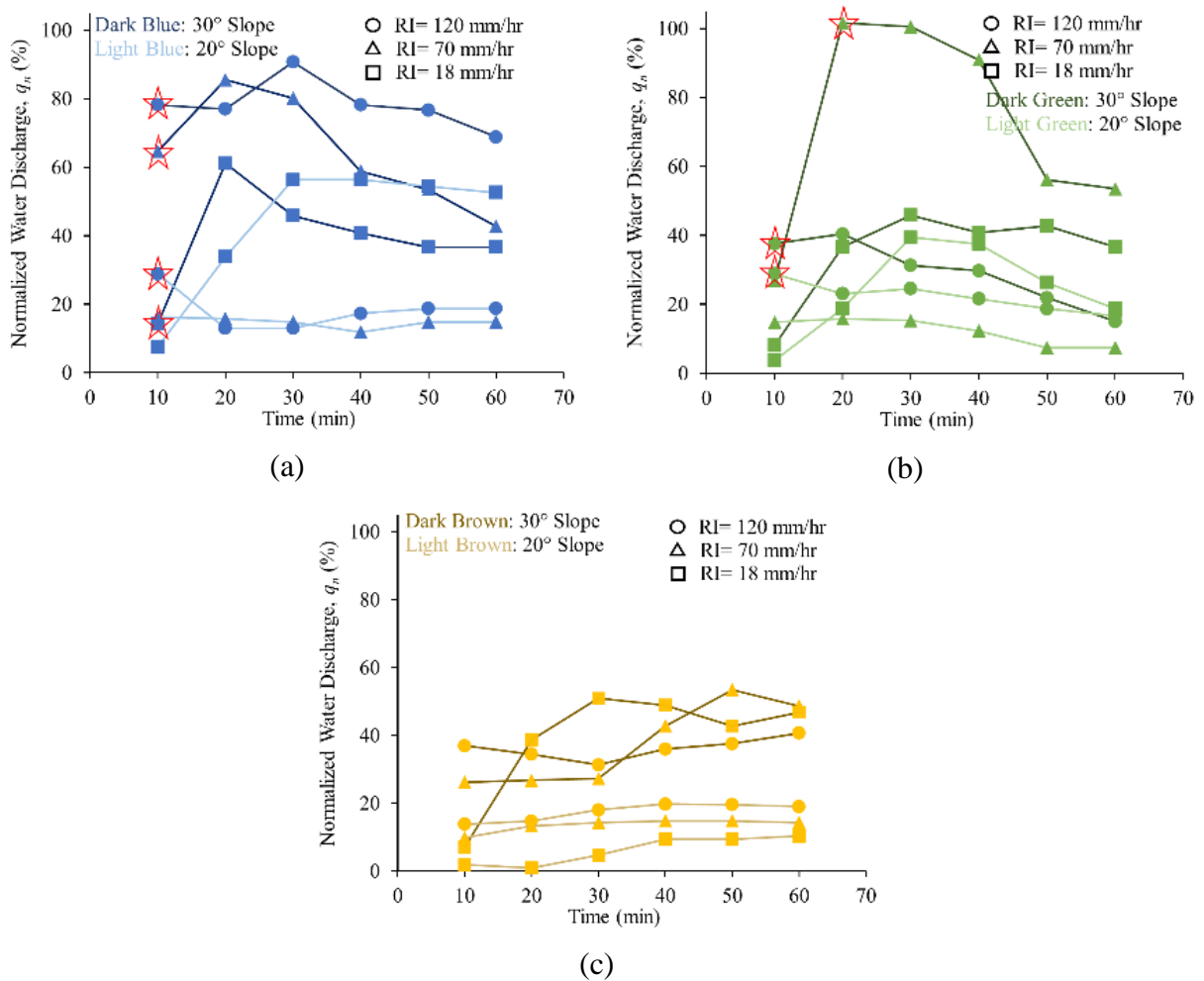
Figure 4.23 Normalized water discharge for (a) fine, (b) medium and (c) coarse sand. Stars indicate the infinite slope failure occurrence.

Figure 4.24 shows the cases where an infinite slope failure occurred. The rain intensity versus the triggering moment of the failure for 20 and 30° slopes are shown. It is indicated that the failure triggers faster in fine sand than in medium sand tests. The failure triggers in less than 2 minutes in fine sand under a 120 mm/hr rain intensity and a 30° slope. The 10° difference in slope gradient does not significantly affect the failure triggering time; however, the rain intensity plays a critical role coupled with the grain size. As mentioned before, the coarse sand tests did not fail under the same circumstances, and this leads to the conclusion that the grain size of sand plays an important role in triggering the infinite slope.
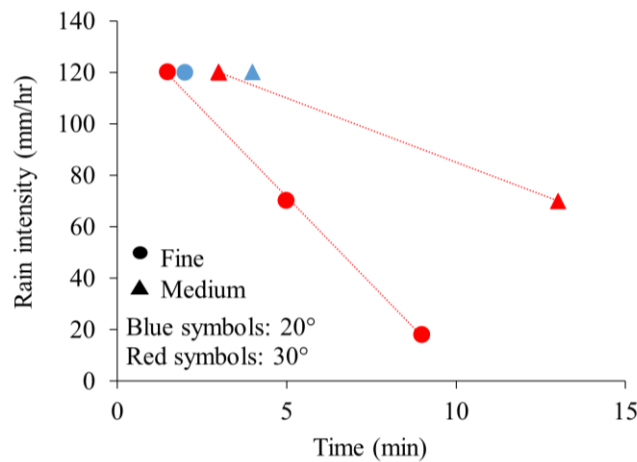
Figure 4.24 Infinite failure triggering time for failed slopes with different rain intensities.

4.3.2.2 Failure mechanism

As shown in Figure 4.18, the failure mechanism in experimental trials, for the case where the hydrophobic layer rests below the regular wettable sand (H-Sub layout), occurs as infinite slope failure. Infinite failure occurs in a plane parallel to the slope surface, and the length of failure is large compared to the thickness of the failure. The factor of safety (F.S.) as an indicator of infinite slope stability is the ratio of the resisting over the driving stresses along the potential slip surface. The slope is susceptible to infinite failure when F.S.< 1. A general form of the factor of safety is

obtained for saturation and seepage conditions (Table 4.1) for a slope at an angle of δ and seepage at the angle of δ^* with respect to the horizontal plane. Three different scenarios are: a) the potential slip surface is in the wettable layer, b) at the boundary of hydrophobic and wettable layer, c) in the hydrophobic layer. The seepage is assumed to be parallel to the slope to simplify the equations. In table 4.1, φ' is the effective friction angle, γ_{sat}, γ_d and γ' are the saturated, dry, and buyout unit weight of soil, z_{inf} and z are the infiltration and failure depth, and h is the wettable layer thickness.

Table 4.1 Infinite failure procedure
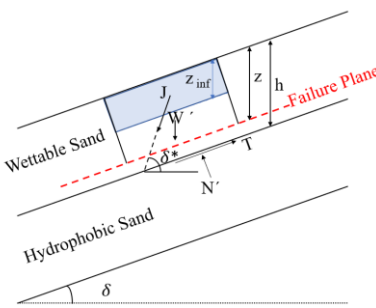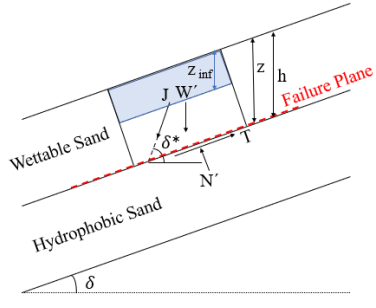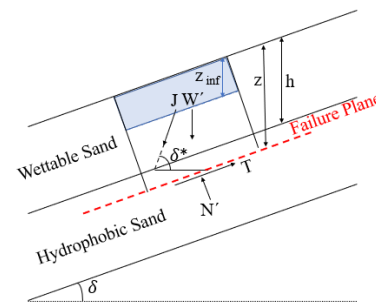
Saturation		
$$F.S. = \frac{tan\varphi'}{tan\delta}$$		
Seepage If seepage is parallel to slope face: $\delta = \delta^*$, $i = sin\delta$ $m_{(t)} = z_{inf}/z$		
a)	b)	c)
If z<h, $$F.S. = \frac{(\gamma' m_{(t)} + \gamma_d(1 - m_{(t)}))}{(\gamma_{sat} m_{(t)} + \gamma_d(1 - m_{(t)}))} \frac{tan\varphi'}{tan\delta}$$	If z=h, $$F.S. = \frac{(\gamma' m_{(t)} + \gamma_d(1 - m_{(t)}))}{(\gamma_{sat} m_{(t)} + \gamma_d(1 - m_{(t)}))} \frac{tan\varphi'}{tan\delta}$$	If z>h, $$F.S. = \frac{(\gamma' m_{(t)} + \gamma_d(1 - m_{(t)}))}{(\gamma_{sat} m_{(t)} + \gamma_d(1 - m_{(t)}))} \frac{tan\varphi'}{tan\delta}$$
If z<h & $z_{inf} = z$ ($m_{(t)}$=1), $$F.S. = \frac{(\gamma')}{(\gamma_{sat})} \frac{tan\varphi'}{tan\delta}$$	If z=h & $z_{inf} = h$ ($m_{(t)}$=1), $$F.S. = \frac{(\gamma')}{(\gamma_{sat})} \frac{tan\varphi'}{tan\delta}$$	If z>h & $z_{inf} = h$ & $m_{(t)} = h/z$, $$F.S. = \frac{(\gamma' h + \gamma_d(z - h))}{(\gamma_{sat} h + \gamma_d(z - h))} \frac{tan\varphi'}{tan\delta}$$

Table 4.2 compares experimental observations of slope stability under 18, 70, and 120 mm/hr rain intensities for the three different sands at 20° and 30° slopes. Overall, results indicate that slopes remain stable for slopes where discharge is much smaller than the infiltration at peak discharge 10-min intervals. For example, at *RI* of 18 and 70 mm/hr, 20° fine, medium, and coarse sand slopes remain stable. Furthermore, the medium sand slope remains stable at 18 mm/hr *RI* and 30° while failing when *RI* increases. Therefore, particle size, which reflects sand permeability, and *RI* play a role in discharge and infiltration dynamics. In finer sand, seepage develops in a thin surficial layer faster than water can infiltrate through the whole layer thickness. Infiltration is inhibited due to smaller pores of finer sand and higher water entry value of the underlying hydrophobic sand. All the coarse sand slopes remained stable during the 60-min experiments. Based on the results of chapter two, hydrophobic coarse sand has a relatively low contact angle and lower water entry value. Furthermore, infiltration occurs sooner in the coarse sand compared to medium and fine sand due to larger pores and rainwater continuously infiltrates through. The water infiltration continues in coarse sand until the water reaches the lower hydrophobic layer. The upper layer also induces a positive water pressure head on the hydrophobic sand layer, thus making it easier for water to infiltrate without any pressure build-up in the boundary of the two layers.

It is important to notice that the ratio of discharge to total received rainwater is lower in low rain intensity, and it increases by increasing the rain intensity. Consequently, the ratio of infiltration to total received rainwater is higher for cases with lower rain intensities, and it decreases by increasing the rain intensity. Meanwhile, the total rainwater received by flume is determined by the rain intensity is also higher in higher rain intensities. Thus, by analyzing the data, we observe that at the same angle of inclination, the total rain that is received by the flume as well as the fraction of total received rain affects the failure.

The normalized discharge reduces after the failure in 20° slope indicating enhanced infiltration and the existence of regular sand (Figure 4.25). On the contrary, the discharge change is subtle after the failure in 30° slopes, which indicates that the underlying hydrophobic layer still prevents the infiltration, and the hydrophobic layer is exposed to rain.

Table 4.2 Values for stability analysis

Soil (Layer thickness h=10mm)	Friction angle, φ' (°)	Rain Intensity, (mm/hr)	Slope gradient, δ (°)	F.S._Saturation	z_{inf} (mm) @ F.S._Seepage=1 (δ*= δ) z= 5 mm	z= 10 mm	z= 12 mm	Water Content (%) @h=10 mm @ t failure	@ 5 min	@ 60 min	Normalized Discharge (%) / Normalized Infiltration (%)	Water discharge, q (lit/m²min)	Infiltration (lit/m²min)	t failure (min)	Test Outcome	
Fine (γ_d ~ 15.6 kN/m³)	30	18	20	1.58	3.6	7.1	8.4	-	2.5	13.9	7.5/92.5	0.023	0.27	-	Stable	-
			30	1	-	<1		11	3.0	-	15/85	0.045	0.25	9	Fail	Seepage
		70	20	1.58	3.6	7.1	8.5	-	5.5	19	15/85	0.2	1	-	Stable	-
			30	1	-	<1		4		-	65/35	0.78	0.43	4	Fail	Seepage
		120	20	1.58	3.4	6.8	8.2	2.9		-	30/70	0.6	1.4	2	Fail	Seepage
			30	1	-	<1		4		-	78/22	1.6	0.4	1.5	Fail	Seepage
Medium (γ_d ~ 15.9 kN/m³)	32	18	20	1.71	4.1	8.2	9.7	-	4.5	13.4	4/96	0.011	0.29	-	Stable	-
			30	1.08	0.7	1.4	1.7	-	3.6	10.4	8/92	0.025	0.28	-	Stable	-
		70	20	1.71	4.1	8.2	9.7	-	7	17.8	15/85	0.18	1.02	-	Stable	-
			30	1.08	0.7	1.4	1.7	13		-	25/75	0.32	0.88	13	Fail	Seepage
		120	20	1.71	4.0	8.1	9.6	8.5		-	30/70	0.6	1.4	3.5	Fail	Seepage
			30	1.08	0.7	1.3	1.7	8		-	38/62	0.77	1.23	3	Fail	Seepage
Coarse (γ_d ~ 16.4 kN/m³)	34	18	20	1.85	4.6	9.2	10.9	-	8.5	9.6	2/98	0.006	0.29	-	Stable	-
			30	1.17	1.4	2.7	3.3	-	9.8	9	7/93	0.022	0.28	-	Stable	-
		70	20	1.85	4.6	9.2	10.9	-	15.3	15	10/90	0.12	1.08	-	Stable	-
			30	1.17	1.4	2.8	3.4	-	14.5	15	25/75	0.3	0.9	-	Stable	-
		120	20	1.85	4.6	9.2	10.9	-	16.9	17	14/86	0.28	1.72	-	Stable	-
			30	1.17	1.4	2.8	3.4	-	15.7	16.2	37/63	0.75	1.25	-	Stable	-
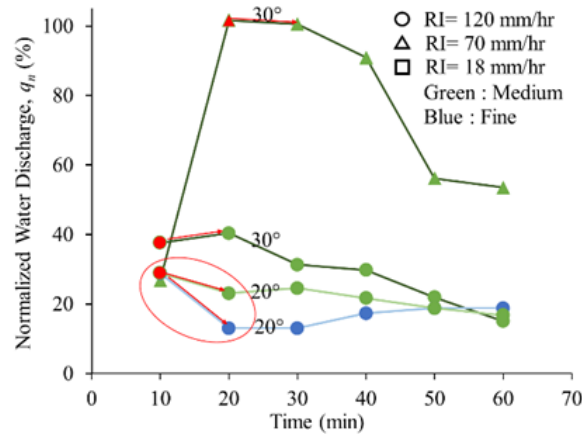
Figure 4.25 Normalized water discharge of failed cases under seepage conditions

4.4   Conclusions

The scope of this study is to investigate the impact of grain size and spatial variability of the hydrophobic layer on slope processes. We varied the slope gradient, rain intensity, and grain size for two different layouts of the hydrophobic sand layer. Rain intensities of 18, 70, and 120 mm/hr are performed on 20° and 30° flumes filled with fine, medium, and coarse grain sand. In the first layout, the hydrophobic sand is at the top surficial layer, while in the second configuration, the hydrophobic layer is 1 cm below the surficial regular sand layer. Two different mechanisms are identified for each of the above-mentioned layouts. While in the first one, surficial erosion dominates the slope process, the second configuration fails as an infinite slope.

In H-Top layout, by varying the grain size, it is shown that the surficial erosion starts immediately after the rain starts in fine sand, while it takes longer for the surficial patterns to form in medium and coarse sand. In the lowest rain intensity, the surficial patterns do not vary significantly, and all slopes erode at very low rates, with small patches formed on the surface. By increasing the rain intensity, the erosion patterns vary and become bolder and start as sequin patches on fine sand and coalesce later. In medium and coarse sand tests, the erosion patterns form

as channels and lead to preferential flows on the surface. Overall, the water discharge amount is higher in fine flume than in medium and coarse flumes. The grain size dominates the discharge amounts in higher rain intensities, while the effect of grain size diminishes by decreasing the rain intensity. Water content results indicate the higher resistance of the fine sand to infiltration, which in response leads to higher surficial erosion. In addition, the fine sand erodes as small patches from all over the surface homogenously until they coalesce, increasing the total erosion. The infiltration starts sooner in medium and coarse sand, and water contents are slightly higher. The channels that form on the medium and coarse sand slopes provide a preferential path for water; thus, the erosion rate decreases on these sands, after the initial erosion, and water flows in the channel and infiltrates the lower layer sooner. These morphological patterns are considered to have a considerable impact on the erosion rate. The gradient of the slope also contributes to the erosion rate and discharge; however, the coarse sand is not greatly affected by steepness. In addition, it is concluded that during high rain intensity, the highest discharge in all grain sizes occurs at the beginning of the test and then declines significantly; thus, no matter how long the rain continues, the first 10-minute interval is the most critical in terms of discharge.

In H-Sub layout, the infinite slope failures occur in fine and medium sand slopes. In this layout, the water infiltrates the wettable sand layer, and once it reaches the hydrophobic layer, the infiltration extremely reduces and the hydrophobic layer acts as a barrier. The fine sand tests show the most vulnerable cases, where infinite failure triggers in as low as 2 minutes of the start of the rain and water contents as low as 4%. The failure time increases by decreasing the rain intensity and increasing the grain size. In coarse sand tests, failure was not observed, and the water contents went up to 17%. In addition, the coarse sand has more infiltration in the hydrophobic layer, which can be related to lower infiltration resistance, lower water entry value, and larger pores. This is

confirmed by the lower water discharge that is collected from coarse sand. The discharge is higher in fine sand flumes, and this amount is significantly affected by rain intensity and steepness. It is worth mentioning that in high rain intensity, the percentage of discharge with respect to total rain received by flume is affected by grain size, such that a higher percentage of water discharges from fine sand compared to coarse sand. However, in lower rain intensity, the percentage of discharged water is not significantly affected by grain size. After the infinite failure happens in the fine and medium sand flumes, the amount of erosion decreases significantly, and the water contents in the lower layer increase.

We concluded that in addition to the effect of wettability on the response of slope during rain, the grain size of the sand plays an important role. The effect of grain size is more significant in higher rain intensities. The results suggest that the fine sand is the most susceptible sand to erosion and failure in both configurations in post-wildfire areas. On the other hand, the coarse sand has the lowest sensitivity to hydrophobicity and did not show a significant change even in the highest rain intensity and steepness tested in this study. Based on the results, the existence of a hydrophobic layer a few centimeters below the surface of a slope can be more destructive than a surficial hydrophobic layer. In these cases, the failure happens in the form of an infinite slope failure, and the movement of the soil mass is very sudden and fast, which is prevalently observed in post-wildfire areas. Seepage-induced infinite failure mechanism with respect to time to failure and overflow dynamics occur at higher ratio of water discharge to infiltration. The post-wildfire areas with finer grain sand can experience these failures in a shorter time span, and more precautions should be taken into account for evacuation plans and emergency response in such areas.

Appendix A

Infinite slope analysis

The infinite slope analysis is derived for a slope with properties of δ as slope gradient, φ' as the effective friction angle of soil, γ_d, and γ_w as dry unit weight of soil and water, z_{inf} and z as the infiltration and failure depth. During rainfall, it is assumed that the water infiltrates into the top wettable soil and the wetting front advances over time. $m_{(t)}$ is defined as the ratio of the infiltration depth to failure depth.
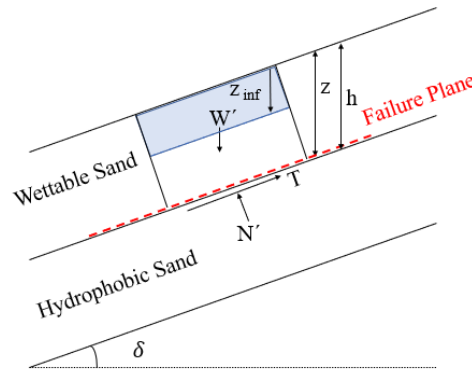
Figure 4.26 Slope with wettable layer over hydrophobic layer (failure plane at the boundary of the two layers)

$$m_{(t)} = z_{inf}/z$$

$$W = (\gamma_{sat}\, z_{inf} + \gamma_d(z - z_{inf}))\cos\delta$$

$$W_T/b = (\gamma_{sat}\, z_{inf} + \gamma_d(z - z_{inf}))\, \cos\delta\, \sin\delta$$

$$W_N/b = (\gamma_{sat}\, z_{inf} + \gamma_d(z - z_{inf}))\, \cos\delta\, \cos\delta$$

$$F.S. = \frac{(\gamma_{sat}\, z_{inf} + \gamma_d(z - z_{inf}))}{(\gamma_{sat}\, z_{inf} + \gamma_d(z - z_{inf}))}\, \frac{\tan\varphi'}{\tan\delta}$$

$$F.S. = \frac{\tan\varphi'}{\tan\delta}$$

The factor of safety for a slice of slope is obtained for a slope subjected to seepage and gravitational forces. The seepage force is expressed as J and can be obtained in normal (J_N) and tangential (J_T) directions. The hydraulic gradient (i) for a flow line with an angle of δ^* with respect to the horizontal surface is calculated across the equipotential lines. The gravitational forces are also shown in normal (W_N) and tangential directions (W_T) with respect to the failure surface slope, and m is the ratio of the depth of infiltration to the failure surface depth.
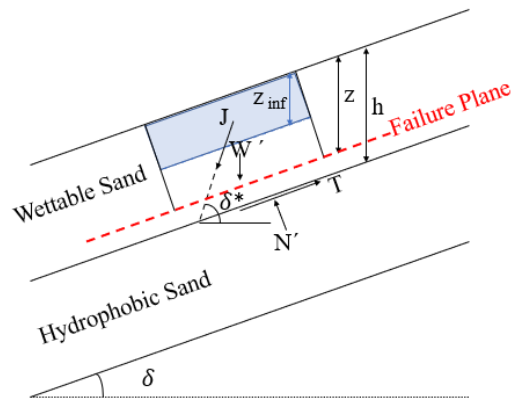
Figure 4.27 Slope with wettable layer over hydrophobic layer (failure plane above the boundary of the two layers)

$$J_T = J \cos(\delta^* - \delta)$$

$$J_N = J \sin(\delta^* - \delta)$$

$$i = \frac{\sin\delta}{\cos(\delta - \delta^*)}$$

$$m_{(t)} = z_{inf}/z$$

$$J_T/b = i\, \gamma_w\, m_{(t)} z\, \cos\delta\, \cos(\delta^* - \delta)$$

$$J_N/b = i\, \gamma_w m_{(t)} z\, \cos\delta\, \sin(\delta^* - \delta)$$

$$W_T/b = (\gamma'\, m_{(t)} z)\, \cos\delta\, \sin\delta + \gamma_d\, (z - m_{(t)} z)\, \cos\delta\, \sin\delta$$

$$W_N/b = (\gamma' \, m_{(t)}z) \, cos\delta \, cos\delta + \gamma_d \, (z - m_{(t)}z) \, cos\delta cos\delta$$

$$\sigma_n = (\gamma' \, m_{(t)}z) \, cos^2\delta + \gamma_d \, (z - m_{(t)}z)cos^2\delta + i \, \gamma_w m_{(t)}z \, cos\delta \, sin(\delta^* - \delta)$$

$$\tau_n = (\gamma' \, m_{(t)}z) \, cos\delta \, sin\delta + \gamma_d \, (z - m_{(t)}z) \, cos\delta \, sin\delta + i \, \gamma_w \, m_{(t)}z \, cos\delta \, cos(\delta^* - \delta)$$

$$F.S. = \frac{((\gamma' \, m_{(t)}z) \, cos^2\delta + \gamma_d \, (z - m_{(t)}z)cos^2\delta + i \, \gamma_w m_{(t)}z \, cos\delta \, sin(\delta^* - \delta) \,)tan\varphi'}{(\gamma' z) \, cos\delta \, sin\delta + \gamma_d \, (z - m_{(t)}z) \, cos\delta \, sin\delta + i \, \gamma_w \, m_{(t)}z \, cos\delta cos(\delta^* - \delta)}$$

If $\delta = \delta *$, $i = sin\delta$ seepge parallel to slope face,

$$F.S. = \frac{(\gamma' \, m_{(t)}z + \gamma_d \, (z - m_{(t)}z))cos^2\delta \, tan\varphi'}{(\gamma' \, m_{(t)}z + \gamma_w m_{(t)}z + \gamma_d \, (z - m_{(t)}z) \,)cos\delta \, sin\delta}$$

In these equations, φ' is the effective friction angle, γ_d is the dry unit weight of soil and γ_w and γ' are the water unit weight and the buyout unit weight of soil, $z_{inf} \, and \, z$ are the infiltration and failure depth.

Acknowledgments

5. Machine learning model for the post-wildfire mudflow onset

5.1 Introduction

With rapid developments in computer technology and advances in data set collection Machine Learning (ML) methods have gained popularity in different fields. Geotechnical problems are characterized by great uncertainties and involve various factors that cannot be directly determined by engineers, which leads to the rapid popularity of machine learning methods (159–161)

ML is the field of study that gives the computer the ability to learn without being explicitly programmed, and a computer program learns from a dataset without the need to code the problem and a procedure to solve it (162). ML algorithms can capture the potential correlations among information without prior assumptions (163,164) and adapt and alter the architecture through repetition and experience. The process of adapting the algorithm to optimally produce the desired outcome when presented with the training inputs can then generalize to produce the desired outcome from new, previously unseen data. This training is the "learning" part of machine learning (162).

This modeling capability and the ability to learn from experience have given ML techniques superiority over traditional modeling since there is no need for making assumptions about what could be the primary rules that govern the problem at hand. ML techniques are being widely used to solve various geotechnical engineering problems, such as in soil classification (165), evaluation of CPT test (166), prediction of the critical factor of safety for slope stability and debris flow likelihood as well as rainfall intensity duration thresholds (137,167,176,177,168–175), prediction of geotechnical properties such as the relations between in-place density using SPT-N

value, compression index, liquid limit and void ratio (178,179), earth dam slope failure probability (160), risk prediction of deep foundations (180) and surface settlement problems (163). Machine learning algorithms include artificial neural networks (ANNs), the support vector machine (SVMs), the random forest (RF), and regression methods (181).

In this research, different ML algorithms are selected to synthesize the results and predict the outcomes of the tests. Logistic regression (LR), multiple regression (MR), and support vector machine (SVM) are used based on their common characteristics that include good predictive performance and prevalent utilization in industry, and the ability to deal with classification and non-linear problems (173). The methods are described in the following section (181).

5.2   Machine learning algorithms

5.2.1   Multiple linear regression

The general purpose of Multiple linear regression (MLR) is to establish a relationship between multiple independent variables and a dependent variable. The general form of the MLR can be shown as following between a dependent (y) and independent (X) variables:

$$y(X) = \lambda_0 + \lambda_1 X_1 + \lambda_2 X_2 + \cdots + \lambda_P X_P \qquad (5.1)$$

where $X_1, X_2, \ldots, X_P$ are the features and $\lambda_0, \lambda_1, \ldots, \lambda_p$ are the optimal coefficients that can be obtained by minimizing the mean squared errors (the difference between the actual and the estimated data).

A variety of statistical techniques exist to quantitatively assess the performance of statistical models. The coefficient of determination R^2 and mean square error (MSE) evaluate how well the model fits the data. R^2 statics measures the proportion of variability in the observed data that is explained by the regression model. The R^2 ranges from 0 to 1, where values close to 0 reflect

situations where the model does not appreciably summarize variation in the outcome of interest, and values close to 1 indicate that the model captures nearly all the variation in the outcome of interest. High R^2 values mean that a high proportion of the variance is explained by the regression model. MSE quantifies the extent to which the predicted response value is close to the true response value for the same observation.

$$R^2 = 1 - \frac{\sum_{i=1}^{n}\left(y_{i(Actual)} - \hat{y}_{i(Predicted)}\right)^2}{\sum_{i=1}^{n}\left(y_{i(Actual)} - \bar{y}_{i(mean)}\right)^2} \quad (5.2)$$

$$MSE = \frac{1}{n}\sum_{i=1}^{n}\left(y_{i(Actual)} - \hat{y}_{i(Predicted)}\right)^2 \quad (5.3)$$

In the above equation, y and $\hat{y}$ are measured and predicted values, respectively, $\bar{y}$ is the mean of the y values, and n is the total number of data. The MSE will be smaller if the predicted and actual true responses are very close. The R^2 varies between 0 and 1, and the higher values mean that the model explains more variance.

5.2.2 Logistic regression

One of the frequently used regression models for modeling the statical likelihood of occurrence of an event is the logistic regression model. This approach uses a logistic curve to define the statistical likelihood of a binary response, such as the likelihood of debris-flow generation. The probability of occurrence of an event (P) ranges between 0 and 1, where approaching 1 means a higher likelihood of the occurrence.

$$P = \frac{e^x}{1+e^x} \quad (5.4)$$

In equation (5.4), P is the logistic function (sigmoid function ($\sigma(x)$)) and indicates the likelihood of the occurrence of the binary response, and x is a linear combination of one or more explanatory variables and is determined by:

$$x = \lambda_0 + \lambda_1 X_1 + \lambda_2 X_2 + \cdots + \lambda_P X_P \qquad (5.5)$$

where $X_1, \ldots, X_P$ are the independent variables that influence the occurrence of the event and λ_0 and $\lambda_1, \ldots, \lambda_P$ are the empirically derived parameters from the training data set. The likelihood function $L(\theta)$ of all samples with labels $y^{(i)} \in \{0,1\}$ can be explained by:

$$L(\theta) = \prod_{i=1}^{m} \sigma(x)^{y^{(i)}} (1 - \sigma(x))^{1-y^{(i)}} \qquad (5.6)$$

Logistic regression model is used frequently in debris-flow likelihood prediction in different studies and regions (168,171,172,176,177,182,183). Some of the variables in these studies include the soil properties such as percentage of the soil clay and liquid limit, average storm intensity, and geospatial properties of the region characterizing the basin morphology such as the gradient of the burnt area with different burnt severities and ruggedness. In this research, we included the water entry value (Ψ_{wev}), median particle diameter size (D_{50}), rain intensity (RI), and gradient of the slope (δ) as our independent variables.

5.2.3   Support vector machine

A support vector machine is an ML algorithm that generalizes a simple classifier called the maximal margin classifier and separates the different classes with a decision boundary with the largest margin possible. The method classifies the samples by finding a hyperplane that produces the optimal separation between classes. For linearly separable classes, the hyper-plane maximizes the margins between the optimum plane and the class-separated vectors in p-dimensional space, where p is the number of influencing variables. Suppose the classes cannot be separated linearly, in that case, a kernel function should be used to map the data to a higher dimensional space to separate the classes by a linear hyper-plane (171).

The maximal margin hyperplane is the separating hyperplane that is farthest from the training data, and it represents the mid-line of the widest 'slab' that we can insert between the two classes. A margin is the perpendicular distance from the closest training observation to the hyperplane. The observations that lie along the width of the margin are known as support vectors and support the maximal margin by controlling the distance. In fact, the maximal margin hyperplane is very sensitive to change in a single observation and may result in overfitting; thus, in the interest of greater robustness to individual observations and better classification of the most of the training data, it could be worthwhile to sacrifice a few training observations and misclassify them. A so-called *soft margin* is when the hyperplane *almost* separates the classes when it is not possible to exactly separate the classes (181). A tunning parameter C is used to control the tolerance of the observations being on the wrong side of the margin. A larger C means a higher tolerance for the observations to be on the wrong side.

For a set of given data $\{x^i, y^i\}_{i=1}^{m}$, where $x^{(i)} = [1, x_1^{(i)}, \ldots, x_p^{(i)}]^T$ with p denoting the number of features, and $y^{(i)} \in \{-1, 1\}$ is the label of the sample $x^{(i)}$, the coefficients $\hat{\lambda} = [\hat{\lambda}_0, \hat{\lambda}_1, \ldots, \hat{\lambda}_p]^T$ of the soft margin hyperplane, and the slack variables are obtained by maximizing M such that:

$$y^{(i)}\left(\hat{\lambda}_0, \hat{\lambda}_1 x_1^{(i)}, \ldots, \hat{\lambda}_p x_p^{(i)}\right) \geq M\left(1 - \epsilon^{(i)}\right) \qquad \forall i = 1, \ldots, m \qquad (5.7)$$

$$\sum_{j=1}^{p} \hat{\lambda}_j^2 = 1 \qquad (5.8)$$

$$\epsilon^{(i)} \geq 0, \sum_{i=1}^{m} \epsilon^{(i)} \leq C \qquad \forall i = 1, \ldots, m \qquad (5.9)$$

where, ϵ is the slack variable that allows individual observations to be on the wrong side of the margin or the hyperplane, and C is a non-negative tuning parameter that acts as a budget to how

many points out of m data points we allow to violate the margin. A testing data $\boldsymbol{x}'$ is classified by checking the sign of $f(x') = \lambda_0, \hat{\lambda}_1 x_1', \dots, \hat{\lambda}_p x_p'$.

Support vector classifiers are used for classifying the classes when they are linearly separable; however, in the case of non-linear class boundaries, support vector machines are used by increasing the feature space using kernels. A kernel is a function that quantifies the similarity of two observations.

5.2.4 Principal component analysis (PCA)

When a large set of variables are available, the principal component analysis can reduce the number of representative variables. PCA is an unsupervised approach that can also be used in data visualization. PCA helps to find a low-dimensional representation of the data set that contains as much possible variation. Each dimension found by PCA is a linear combination of the p features.

The first component of a set of features, $X_1, X_2, \dots, X_p$ is the normalized linear combination of the features that has the largest variance and are combined with loadings of the first component $(\kappa_{11}, \kappa_{21}, \dots, \kappa_{p1})$.

$$Z1 = \kappa_{11}X_1 + \kappa_{21}X_2 + \cdots + \kappa_{p1}X_P \qquad (5.10)$$

The number of components can be determined based on the proportion of the variance explained by each principal component. In other words, we can determine how much information we are willing to lose by projecting the observations onto the first few principal components. The variance explained by mth principal component is:

$$\frac{1}{n} \sum_{i=1}^{n} z_{im}^2 = \frac{1}{n} \sum_{i=1}^{n} \left(\sum_{j=1}^{p} \kappa_{jm} x_{ij} \right)^2 \qquad (5.11)$$

And the proportion of the variance explained (PVE) of the mth principal component is given by:

$$\frac{\sum_{i=1}^{n} \left(\sum_{j=1}^{p} \kappa_{jm} x_{ij}\right)^2}{\sum_{j=1}^{p} \sum_{i=1}^{n} x_{ij}^2} \qquad (5.12)$$

5.2.5   K-means Clustering

Clustering refers to grouping the observations of a data set and separating them into distinct groups, while each group has similar observations. Similarity or difference should be defined based on the knowledge of the data studied.

K-means clustering in which we specify the desired number of clusters *K*, randomly assign a number from 1 to *K* to each observation, calculate the centroid for each cluster, and assign each observation to the cluster whose centroid is closest iterate until the cluster assignments stop changing.

5.3   Model performance criteria

The predictive performance of classification models is evaluated using the confusion matrices, also known as error matrices. The confusion matrix visualizes the model's performance using four classes for quantifying the model performance described in the following paragraph. Event occurrence is either TRUE (occurred) or FALSE (not occurred).

True positives (*TP*) are the samples that the predicted label and the actual label of the sample, both belong to the TRUE class.

False Positives (*FP*), or Type I error are the samples in which the predicted label of the sample is TRUE, but its actual label is FALSE.

True Negatives (*TN*) are the samples that the predicted label and the actual label of the sample, both belong to the FALSE class.

False Negatives (*FN*), or Type II errors are the samples that the predicted label of the sample is FALSE, but its actual label is TRUE.

In this study, the outcome of the experimental results are classified into two classes, the first class refers to the tests that did not fail ("*No failure: 0*"), and the second class refers to the tests in which infinite failure occurred ("*Infinite failure: 1*"). *TP*s correspond to the number of failed tests that are correctly predicted by the model. *FP*s are the number of tests that did not fail in the experiment but were predicted as failed by the model. *FN*s correspond to the tests that failed in the experiment, but the model missed the failure and predicted it as not failed. *TN*s are the number of correctly predicted "*No failure*" by the model which did not fail in the experiment.

Using the four above-mentioned classes, the performance of models is evaluated with precision, accuracy, and threat score (*TS*). Precision measures how accurately the model can detect a correct labeled TRUE class (*TP*) from all those predictions that were predicted TRUE (*TP+FP*). Accuracy measures how accurately the model can detect a true labeled TRUE (*TP*) and a true label FALSE (*TN*) (174). The threat score (*TS*) indicates the model's overall performance by reducing its value for each incorrect prediction (*FP* or *FN*).

$$\text{Precision} = \frac{TP}{TP+FP} \quad (5.13)$$

$$\text{Accuracy} = \frac{TP+TN}{TP+FP+TN+FN} \quad (5.14)$$

$$\text{Threat score } (TS) = \frac{TP}{TP+FP+FN} \quad (5.15)$$

K-fold cross-validation

One of the popular validation methods in classification models is k-fold cross-validation (CV). In this method, the training set is divided into k folds, and the classification model is trained for k-1 folds and then validated using the remaining fold. This process is repeated for k times with different folds set aside as the validation set.

5.4   Technical route

The methods used in this study are described above. Total data consists of the results of 36 experimental tests, which are divided into two groups of H-Top and H-Sub layouts. For the first group, H-Top layout, we attempted to predict the total values of water discharge and erosion rates by applying a multiple linear regression method.

For the second group, H-Sub layout, the goal is to classify the outcomes and determine whether the model experiences a failure in terms of an infinite failure or not. First, a clustering method is used along with principal component analysis to divide the data into two clusters, and a support vector classifier is used to determine the maximal margin hyperplane between the two classes. A logistic regression method is also used to classify the data based on the outcomes and determine the probability and likelihood of the failure with the given parameters.

For both H-Top and H-Sub layout analysis, four influencing features are median grain size (D_{50}) in mm, water entry value (Ψ_{wev}) in kPa, slope gradient (δ) in degrees, and rain intensity (RI) in mm/hr. An outline is shown in Figure 5.1 to summarize the technical route and the applied methods.
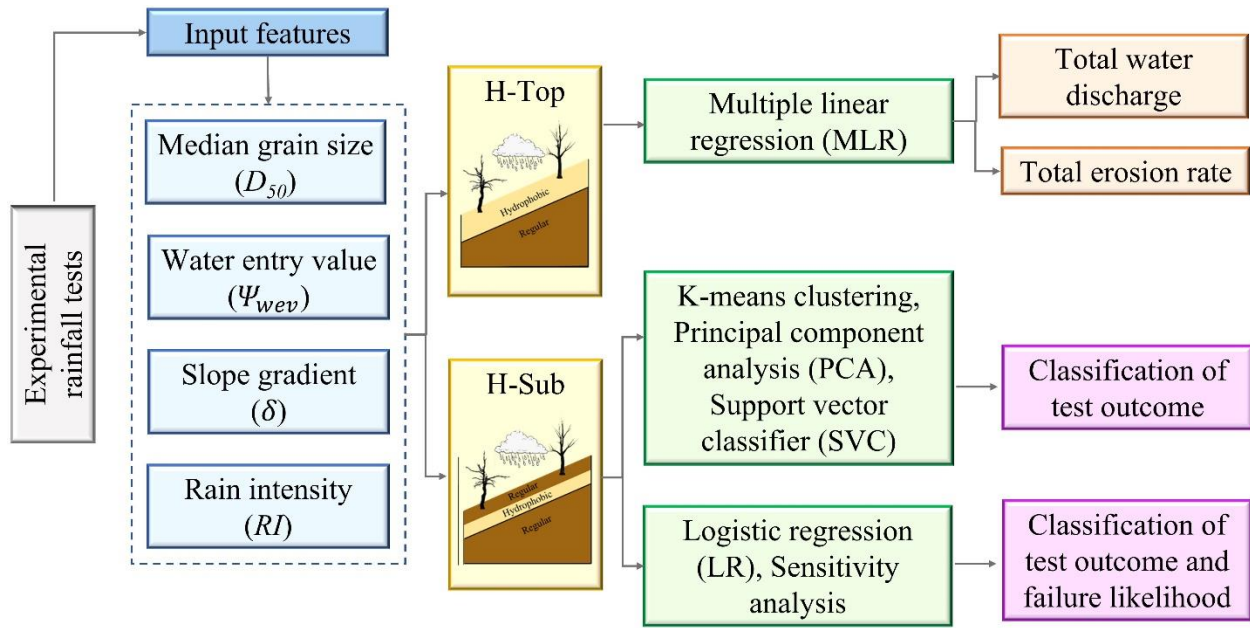
Figure 5.1 Outline of the technical route for this study

5.5 Results

5.5.1 Multiple linear regression (H-Top layout)

In the first part of the study, a multiple linear regression (MLR) model is used to predict the total amount of water discharge and erosion rate. Data includes the 18 experimental results of H-Top layout tests, where a hydrophobic layer of soil rests on the top surface of the flume. The data is divided into two sets of training data; to train the MLR model, and testing data; to test the trained model. The ratio of testing to training data has been set to 35% in order to get an accurate model based on the limited data from experimental results.

Different features such as median grain size (mm) (D_{50}), the effective size of soil (mm) (D_{10}), coefficients of curvature and uniformity of sand (C_c, C_u), contact angle θ (°), friction angle φ (°), water entry value (kPa) (Ψ_{wev}), slope gradient δ(°), and rain intensity (mm/hr) (RI) are introduced to the model, and a correlation matrix is obtained to visualize the correlation of the

112

input features with output results (Figure 5.2). The test outputs such as total cumulative erosion rate (gr/m^2) and total cumulative water discharge (lit/m^2) are shown with *TE* and *TD* symbols in the correlation matrix. In addition, the erosion rate in first, second, …, sixth 10-minute intervals are shown with *1E, 2E, …,6E* (gr/m^2.min) respectively and water discharges are shown with *1D, 2D, …, 6D* (lit/m^2.min). The correlation matrix shows that the contact angle (θ) and water entry value (Ψ_{wev}) have a similar correlation with different outputs, and for that reason, contact angle is removed from the features. The correlation between D_{50} and D_{10} with the discharge and erosion rates is very similar. Basically, the D_{10} values are 1.3~1.4 times smaller than D_{50} values, and this ratio is almost the same for all sands. Since the proportionality of D_{50} and D_{10} values is constant for all sands, the correlations of results are not affected. The coefficient of curvature (C_c) has a similar correlation as D_{10} and D_{50}. The correlation of C_c, $D_{10,}$ and D_{50} is stronger for erosion rate than discharge values.

It is shown that while Ψ_{wev}, δ , and *RI* are positively correlated with discharge and erosion, D_{50} shows a negative correlation. The correlations between the total discharge amount (*TD*) and the input features show that *RI* has the highest absolute correlation value (0.77), followed by δ (0.44). D_{50} and Ψ_{wev} have similar absolute correlation values (0.28) with *TD*. The absolute correlation value of RI (0.5) decreases for total erosion rate (*TE*), while the absolute correlation value of D_{50} (0.59) and Ψ_{wev} (0.52) increases, and the correlation of δ (0.4) stays almost unchanged. The rain intensity (*RI*) correlation with erosion and discharge values shows that overall, the correlation of *RI* is stronger at the beginning of the tests and decreases by increasing the time. The slope angle (δ) shows an almost constant correlation with erosion rate over time while becoming stronger in correlation with discharge as time passes. The correlation matrix is beneficiary in depicting the overall influence of different features on the outputs.

	D_{50}	D_{10}	C_u	C_c	Ψ_{wev}	θ	φ	δ	RI	1D	2D	3D	4D	5D	6D	TD	1E	2E	3E	4E	5E	6E	TE
D_{50}																							
D_{10}	1																						
C_u	0.1	0.077																					
C_c	0.9	0.89	0.52																				
Ψ_{wev}	-0.9	-0.89	-0.53	-1																			
θ	-0.93	-0.92	-0.47	-1	1																		
φ	0.98	0.98	0.28	0.97	-0.96	-0.98																	
δ	4e-3	9e-2	7e-1	5e-2	3e-1	4e-1	8e-1																
RI	4e-2	5e-2	2e-0	2e-2	1e-8	3e-1	8e-1	4e-1															
1D	-0.29	-0.29	0.076	-0.29	0.28	0.29	-0.3	0.22	0.86														
2D	-0.32	-0.32	0.012	-0.28	0.27	0.28	-0.31	0.34	0.83	0.94													
3D	-0.26	-0.26	-0.14	-0.29	0.29	0.29	-0.28	0.5	0.66	0.86	0.93												
4D	-0.27	-0.27	0.056	-0.25	0.25	0.26	-0.27	0.56	0.59	0.76	0.9	0.95											
5D	-0.18	-0.17	-0.28	-0.27	0.27	0.26	-0.22	0.6	0.53	0.65	0.77	0.83	0.88										
6D	0.098	0.09	-0.3	-0.21	0.21	0.2	-0.15	0.59	0.51	0.55	0.69	0.73	0.79	0.97									
TD	-0.28	-0.28	-0.12	-0.29	0.29	0.3	-0.29	0.44	0.77	0.92	0.98	0.97	0.94	0.87	0.78								
1E	-0.44	-0.45	0.082	-0.35	0.34	0.36	-0.41	0.29	0.73	0.91	0.96	0.87	0.84	0.64	0.54	0.91							
2E	-0.59	-0.59	0.0089	-0.51	0.5	0.52	-0.57	0.44	0.43	0.71	0.84	0.83	0.88	0.68	0.56	0.83	0.89						
3E	-0.64	-0.64	-0.21	-0.64	0.64	0.65	-0.66	0.43	0.3	0.65	0.72	0.8	0.81	0.69	0.57	0.77	0.76	0.91					
4E	-0.63	-0.63	-0.2	-0.63	0.63	0.64	-0.65	0.41	0.32	0.69	0.73	0.8	0.8	0.67	0.53	0.77	0.77	0.91	0.99				
5E	-0.63	-0.62	-0.21	-0.63	0.63	0.64	-0.64	0.38	0.29	0.63	0.69	0.78	0.8	0.7	0.59	0.75	0.72	0.87	0.98	0.98			
6E	-0.58	-0.57	-0.25	-0.6	0.6	0.61	-0.6	0.4	0.33	0.67	0.71	0.8	0.78	0.73	0.63	0.78	0.72	0.82	0.97	0.95	0.98		
TE	-0.59	-0.59	0.06	-0.53	0.53	0.55	-0.58	0.4	0.51	0.81	0.88	0.88	0.89	0.71	0.59	0.88	0.92	0.97	0.95	0.95	0.92	0.9	

Figure 5.2 Correlation matrix for H-Top results

A multiple linear regression approach predicts total discharge and erosion rates. The initial six features are reduced to four final features, D_{50}, Ψ_{wev}, δ, and RI, to train the data since the elimination of contact angle (θ), and friction angle (φ) did not affect the results of the predictive capability of the MLP models.

Theoretically, the water discharge and erosion rate should be close to zero if there is no rainfall and intensity (RI) is set to zero. For that reason, all other features, D_{50}, Ψ_{wev}, and δ, are multiplied by RI, so that in the absence of rain ($RI=0$), the output of discharge and erosion rate is close to zero value. Some researchers have recently applied the same approach to post-fire debris-flow likelihood studies (172,176,177). The following equation (Eq. 5.16) shows the multiple linear

regression that is used in this study. In this equation, X_1 is the first feature and denotes $D_{50}.RI$, X_2 denotes $\Psi_{wev}.RI$, and X_3 is $\delta.RI$. The rainfall intensity is based on one hour accumulation.

$$y(X) = \lambda_0 + \lambda_1 X_1 + \lambda_2 X_2 + \lambda_3 X_3 \qquad (5.16)$$

Table 5.1 shows the variables and optimal coefficients of the different variables in the trained model. The models are trained based on 65% of the total data. 35% of the remaining data is used for testing the model. To evaluate the performance of the model, the mean squared errors and R^2 score of each model for training and testing data are shown in the table.

Table 5.1 Summary of coefficient and statistical evaluation parameters for testing and training data of the multiple linear regression models for total discharge (TD) and total erosion (TE)

Features	Coefficients	Total Discharge (*TD*) (Duration=60 min)	Total Erosion (*TE*) (Duration=60 min)
	λ_0	11.3	-15.2
X_1 ($D_{50}.RI$)	λ_1	-0.46	-90.7
X_2 ($\Psi_{wev}.RI$)	λ_2	0.025	-5.2
X_3 ($\delta.RI$)	λ_3	0.025	2.9
Evaluation		R^2 train: 0.96 R^2 test: 0.72 MSE train: 14.5 MSE test: 75.3	R^2 train: 0.87 R^2 test: 0.45 MSE train: 655911 MSE test: 1070667

Figure 5.3 and Figure 5.4 compares the training and testing data collected from experimental data with predicted results from MLR models. The model evaluation is also shown in Table 5.1 for both testing and training predictions. The MLR model captures the total discharge (*TD*) with 0.96 and 0.72 R^2 values for training and testing data. This indicates the lower variation in the output-dependent attribute, which is predicted from the independent input variables. On the other hand, the MLR model for total erosion (*TE*) has an R^2 value of 0.87 for training data, while

it decreases to 0.45 in testing data. This means that approximately 45% of observed variation can be explained by the model's input and shows that the model is likely overfitted.

The general purpose of MLR is to learn more about the relationship between the independent (D_{50}, Ψ_{wev}, δ, RI) variables and a dependent or criterion variable which is the total discharge (*TD*) and total erosion (*TE*) in this case. While the total discharge (*TD*) model captured a good prediction, the total erosion (*TD*) did not perform as well. It is clearly observed in Figure 5.5 (a) that the predicted total discharge amounts are closer to their actual values both in training and testing data points. However, the actual and predicted total erosion data is more scattered around the identity line (Figure 5.5 (b)).
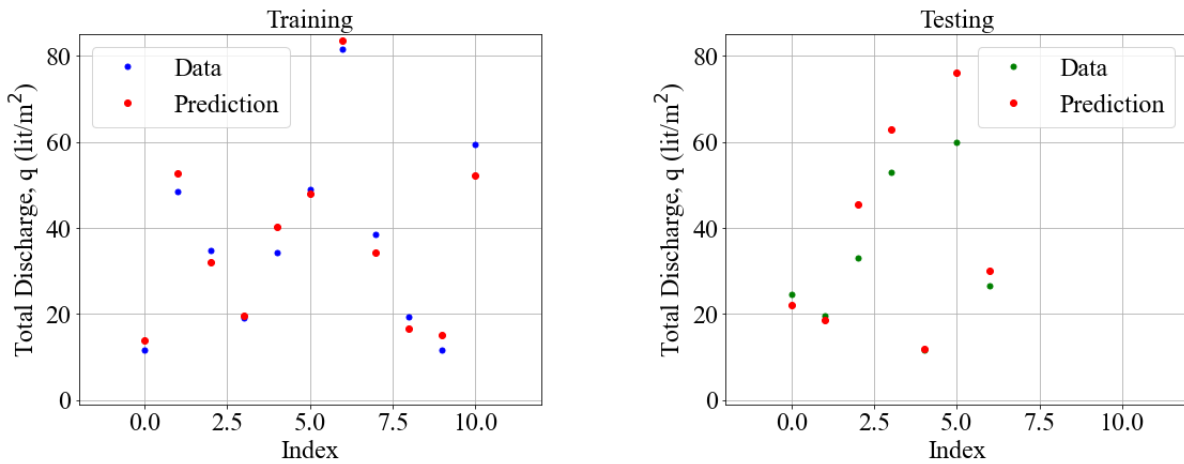
Figure 5.3 Training data (blue symbols) (left) and testing data (green symbols) (right) and predictions (red symbols) of MLR model for total discharge
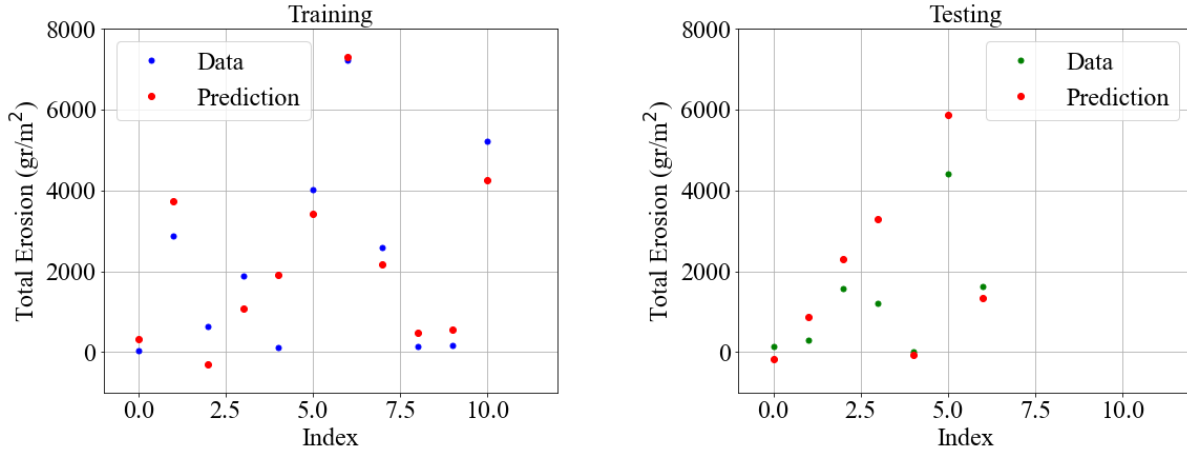
Figure 5.4 Training data (blue symbols) (left) and testing data (green symbols) (right) and predictions (red symbols) of MLR model for total erosion

(a)   (b)
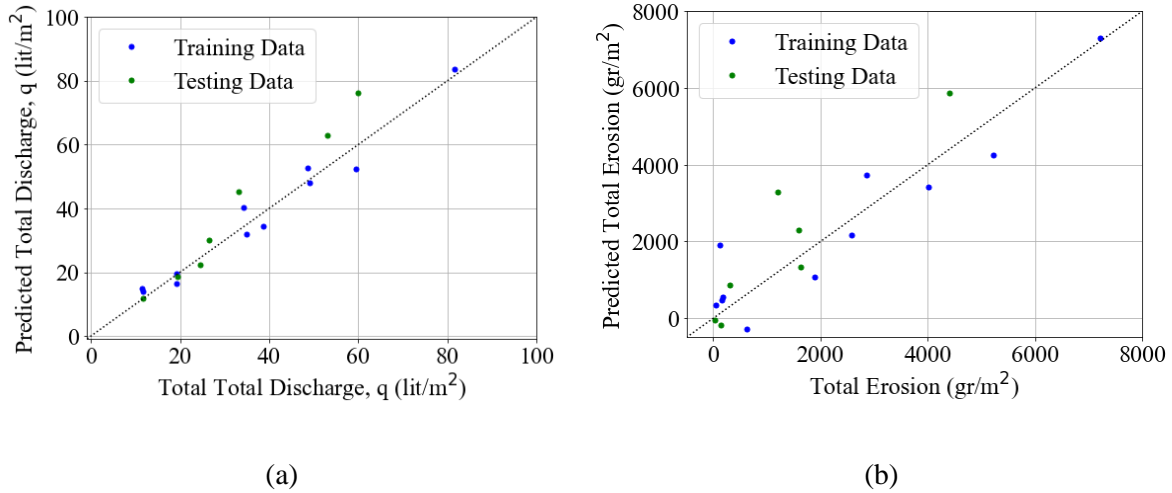
Figure 5.5 Performance of MLR models in predicting the training and testing data for (a) total discharge and (b) total erosion

The lower accuracy of the MLR model for erosion can be related to the small values of the erosion in coarse sand. The values close to zero affect the overall fitting process of the regression and can even lead to negative predictions for the tests with smaller variable values.

5.5.2 K means cluster and principal component analysis (PCA) (H-Sub layout)

The K means clustering method is easy and simple to separate the data set into k clusters. In this study, the k means clustering method is used to cluster the H-Sub layout data into two clusters that demonstrate the experiments that experienced infinite failure and those that did not fail. 18 data sets are available from the experiments. The input variables of the model are median grain size (D_{50}), water entry value (Ψ_{wev}), friction angle (φ), contact angle (θ), slope gradient (δ), and rain intensity (RI).

Prior to the clustering, a principal component analysis is performed (PCA) to reduce the number of the input variables while maintaining the variability in the original set. It is worth mentioning that the variables are all standardized separately by subtracting the mean and dividing by the standard deviation to shift the distribution to have a mean of zero and a standard deviation of one. Figure 5.6 shows the cumulative explained variance corresponding to the number of components. The analysis shows that the first two principal components together can explain 75% of the variance in data. The last four principal components explain only 10% of the variance. We selected two principal components due to the good variance coverage and easier visualization of two components in 2D plots. One of the main objectives of the machine learning analysis for this study is to enhance the visualization and synthesize the results; thus, having two principal components helps us to achieve this goal.
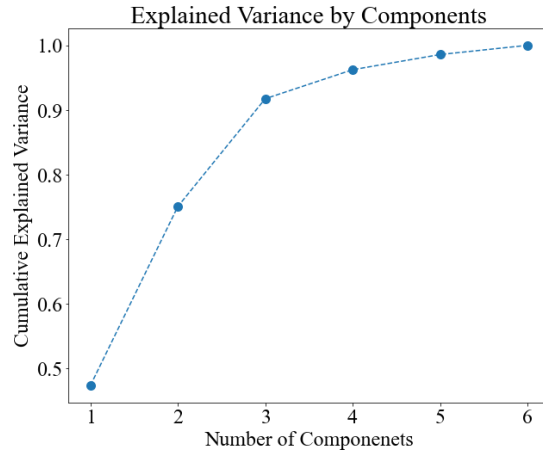
Figure 5.6 Cumulative explained variance versus the number of components

After the PCA analysis and selection of the first and second principal components (Z_1 and Z_2), the k-means clustering is performed for the dataset. Figure 5.7 (a) shows the two clusters with brown ("*No failure*"= 0) and blue ("*Infinite failure*"= 1). The experimental results are also shown in Figure 5.7(b) with two principal components and with the same color codes. The results show that the k-means clustering method has successfully divided the two classes, and only two of the data points are mistakenly clustered as class 0 or "*No failure*" (marked with the red circle) while they failed in infinite failure form in the experiments.

(a) K-means clustering (b) Actual data in binary classification
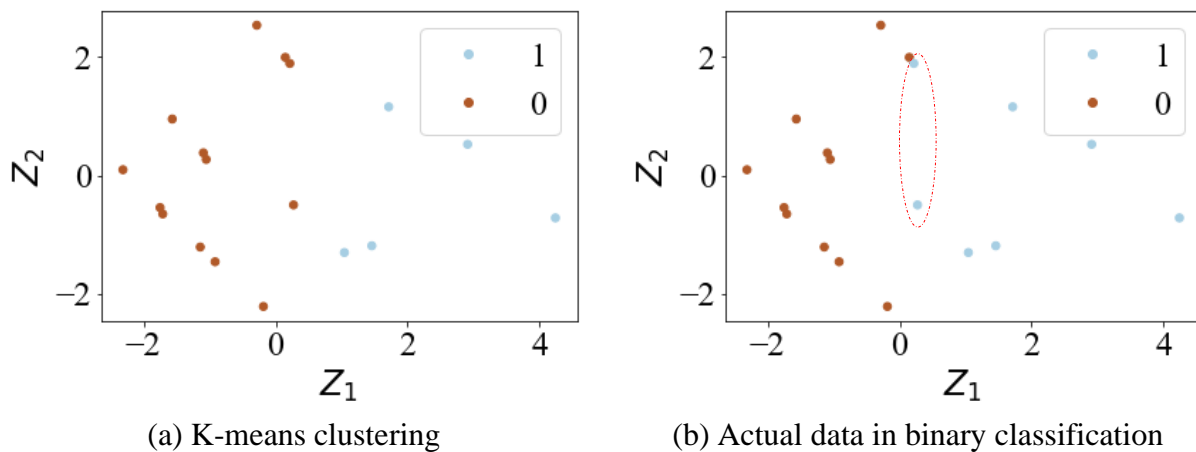
Figure 5.7 Binary classification of experimental outcomes as ("*No failure*"= 0) and ("*Infinite failure*"= 1) with (a) K-means clustering method. (b) Binary classification of experimental outcomes as ("*No failure*"= 0) and ("*Infinite failure*"= 1)

5.5.3 Support vector classifier (SVC)

After reducing the dimension of features with PCA analysis and clustering the data, this time support vector classifier (SVC) algorithm is used to detect a decision boundary to separate the two classes of the outputs. The two classes are labeled as 1 for the cases where the infinite failure occurred and 0 for the cases with no failure. A linear kernel is used for the decision boundary between the two classes. Regularization parameter (C) is used for the penalty parameter of the error term. In other words, it controls the tradeoff between the classification of training points accurately and a smooth decision boundary and suggests the model choose data points as a support vector.

Figure 5.8 (a-c) shows the effect of the parameter C on the width of the margin and the number of support vectors. Support vectors are the data points that support the decision boundary. It is shown that when $C = 10$ (Figure 5.8 (a)), the width of the margin is smaller, and there are 5 support vectors, all from class 0 (brown data points). As C becomes smaller, the margin width the number of support vectors increase, and the model choose more data points as a support vectors, and we get a higher variance and lower bias, which may lead to the problem of overfitting. In the case of large C, we also encounter the problem of underfitting and get a low variance and high bias. For this case, $C=1$ is the most appropriate selection.

(a) C=10   (b) C=1   (c) C=0.1
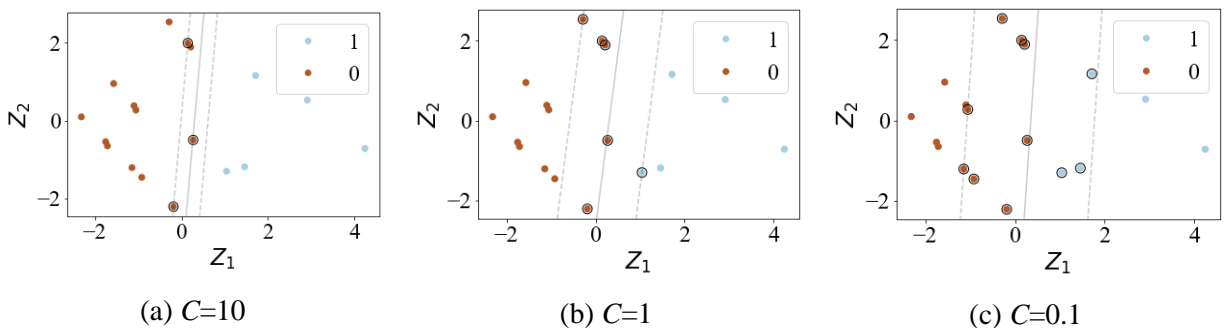
Figure 5.8 Binary classification of experimental outcomes as (“*No failure*”= 0) and (“*Infinite failure*”= 1) with SVC classifier with linear kernel.

Figure 5.9 shows the SVC model with training and testing data split by a ratio of 35% and *C*=1. Confusion matrices in Figure 5.10 for both training and testing data measure the performance of the classified problem and visually summarize the counts from actual versus predicted values. The training precision and accuracy is about 0.8, which means that the model correctly recognizes 8 out of 10 labeled 1s (*Infinite failure*) and can accurately detect 8 label 1s (*Infinite failure*) and label 0s (*No failure*) out of total 10 data points. In the testing data set, the precision is 1, and the accuracy is 0.85. Higher precision in testing data is due to the small amount of data. The testing to training ratio has been modified between 0.2 to 0.5 to check the precision and accuracy of the training and testing data. The accuracy and precision have not varied much, which shows the SVC model is performing well.
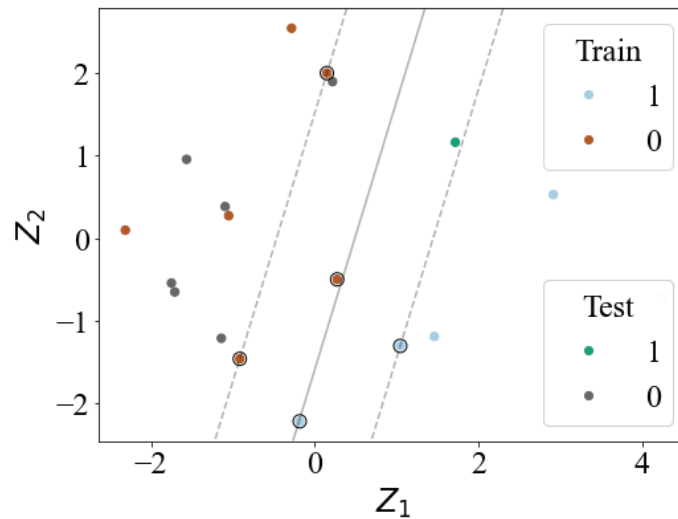
Figure 5.9 Binary classification of the testing and training data with SVC.
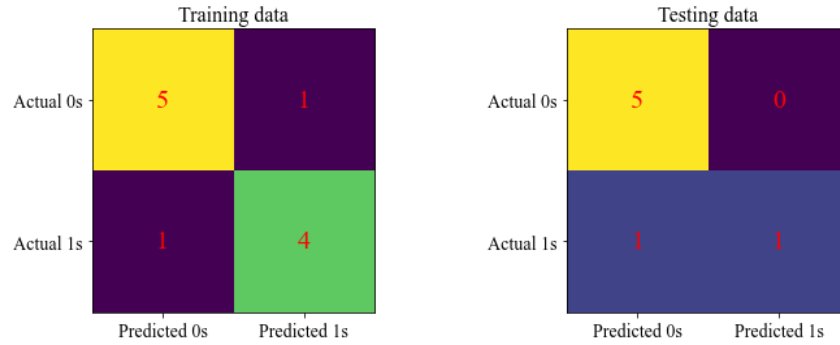
Figure 5.10 SVC Model performance demonstrated with confusion matrices for training and testing data

Finally, K-Fold cross-validation is performed to validate the SVC classification. The goal is to determine how well the statistical learning procedure can be expected to perform on independent data. In this case, 7-fold cross-validation is performed on data and run 5 times, shuffling the data for each run (Figure 5.11). The accuracy for the SVC model with $C=1$ varies approximately between 0.75 and 0.8, which shows the model is reliable and performs well.
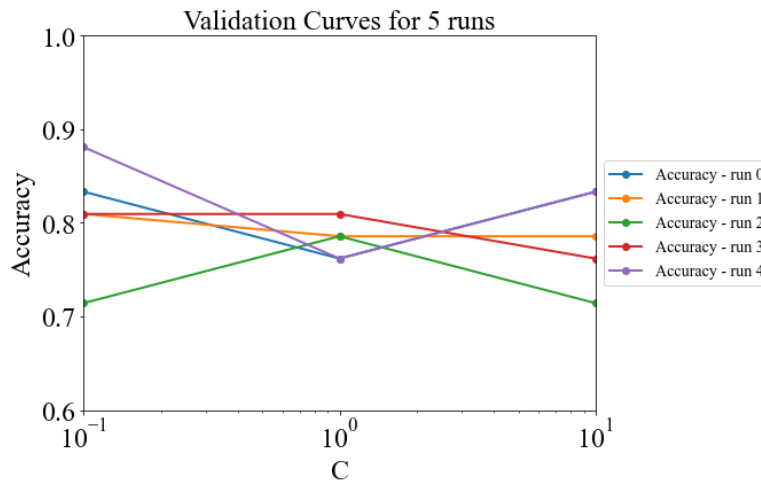
Figure 5.11 7-fold cross-validation with 5 runs for SVC model

5.5.4   Logistic regression

Logistic regression (LR) is applied to estimate the probability of the binary response based on the D_{50}, Ψ_{wev}, δ, and RI variables. The goal is to find the optimal coefficients (λ) that will maximize the likelihood function (Eq.5.6). In order to find the optimal coefficients, the batch gradient descent algorithm (Eq.5.17) is used, and the optimal coefficients are then applied to the likelihood function $\log L(\lambda)$ (Eq.5.6). This is an iterative method that terminates that includes an iteration index (υ) and a learning rate (η).

$$\lambda^{\upsilon+1} = \lambda^{\upsilon} - \eta \frac{\partial \log L(\lambda^{\upsilon})}{\partial \lambda} \qquad (5.17)$$

The four variables are combined in Eq.5.18 such that in the absence of rainfall (RI=0), the probability of the infinite failure occurrence is close to zero:

$$x = \lambda_0 + \lambda_1 D_{50}.RI + \lambda_2 \Psi_{wev}.RI + \lambda_3 \delta.RI \qquad (5.18)$$

$\lambda_1, \lambda_2, \lambda_3$ are the optimal coefficients that are extracted using the gradient batch algorithm that is defined earlier in Eq.5.17 and λ_0 is the intercept of the model. The input variables are all standarized to reduce the variance in the prediction. The optimal coefficients are listed in Table 5.2.

Table 5.2 Summary of variables, coefficient and statistical evaluation parameters for testing and training data of the logistic regression (LR) model

Features	Coefficients	Logistic regression
	λ_0	-2.38
X_1 ($D_{50}.RI$)	λ_1	-2.39
X_2($\Psi_{wev}.RI$)	λ_2	0.53
X_3($\delta.RI$)	λ_3	4.13
Evaluation	Training Precision: 0. 80 Training Accuracy: 0.9 Training *TS*: 0.66	Testing Precision: 1.00 Testing Accuracy: 0.9 Testing *TS*: 0.50

Figure 5.12 (a-b) shows the training and testing data and the probability and prediction by LR model. The prediction is a binary classification of 0s for the cases where failure did not occur ("*No failure*") and 1s for the cases where the infinite failure occurred ("*Infinite failure*"). The value of P=0.5 is set as the threshold of the probability of the occurrence of infinite failure. Suppose the predicted probability is lower than 0.5. In that case, the prediction will be in class 0 or "*No failure*", and if the predicted probability is 0.5 or higher, the prediction will fall into class 1 or "*Infinite failure*". Figure 5.13 shows the confusion matrix that shows the performance of the LR model. The training precision and accuracy are about 0.8 and 0.9, and the threat score (*TS*) is 0.66. The testing precision is 1, the threat score (*TS*) is 0.5, and the accuracy is 0.9. Overall, the model performs well, and it can detect the failed cases from all predicted failed cases with high precision. In addition, the model accurately detects the failed and not failed cases from all data.
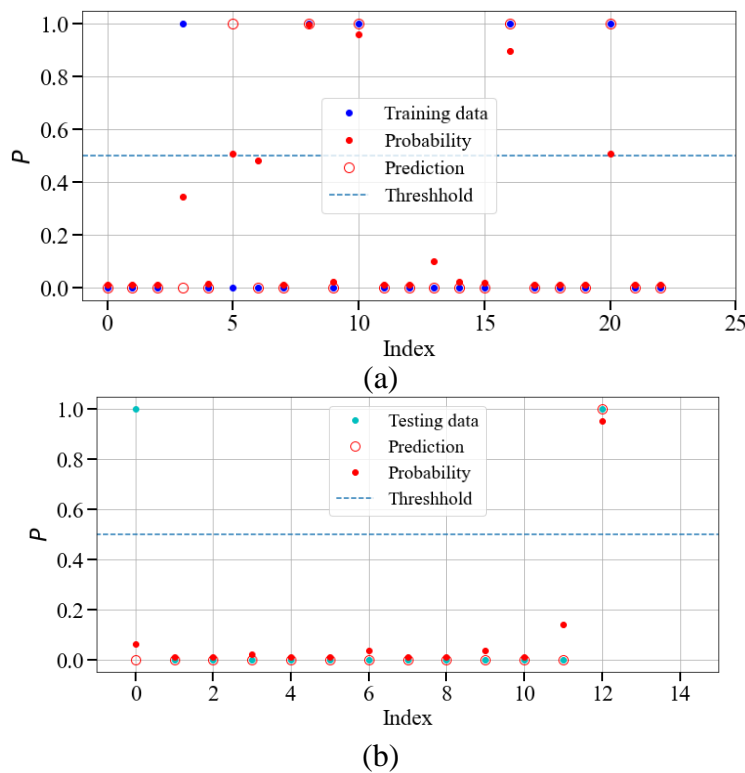
Figure 5.12 (a) Probability (*P*) (red filled symbols) and predictions (hollow red circles) of LR model for (a) training and (b) testing data. The threshold that separates the two classes *P*= 0.5.
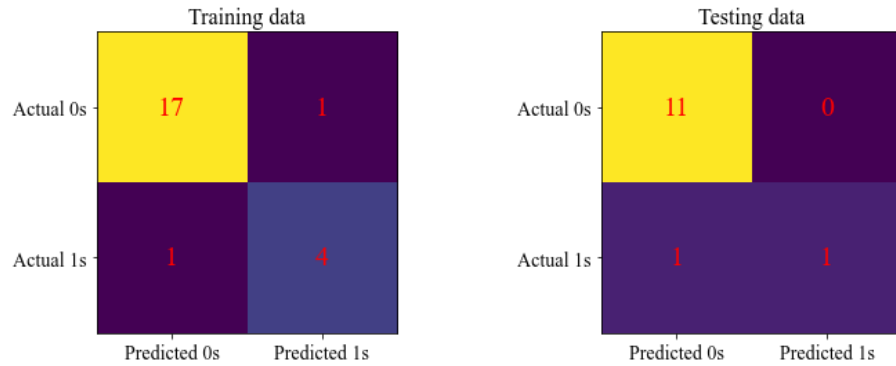
Figure 5.13 LR Model performance demonstrated with confusion matrices for training and testing data

5.5.5   Sensitivity analysis

Sensitivity analysis is performed to demonstrate the model's sensitivity over a representative range of values for an individual variable while the other variables stay constant. The standard deviation method of Friedman and Santi (176,184) has been used to perform the analysis. In this method, the mean value of the three variables is assigned for three of four variables and the fourth variable is varied over a representative range, and the probability analysis is performed. This approach allows us to observe the sensitivity of the model to one specific variable throughout its range. The process has been repeated for each of the variables and all testing conditions. The x-axis of plots shows the standard deviation, and the y-axis shows the probability of infinite failure occurrence. Four variables are shown with blue (D_{50}), red (Ψ_{wev}), green (δ), and purple (RI) colors.

By comparing all tests, it is shown that the effect of rain intensity (RI) fades, and the model becomes less sensitive to RI in tests with coarser grain sand. For instance, by comparing Figures 5.14 (a)- 5.16 (a), the probability of failure decreases from 1 to almost zero when the RI value is in the higher bound of its range. However, the model becomes more sensitive to variation in rain range in 30° slope than 20° slope (see Figure 5.15 (a) and (b)), and this effect is eminently observed

for medium and coarse sands by comparing columns (a) and (b) of Figure 5.15 and Figure 5.16. It is observed that with the same RI data range, the probability of failure for medium soil reduces approximately 50% (from 1 to 0.5) (Figure 5.15 (a,c,e) and (b,d,f)) and, reduces 65% (from 0.65 to 0)(Figure 5.16 (a,c,e) and (b,d,f)) in coarse sand when RI=120 mm/hr. The model remains very sensitive to RI variation in fine sand for both 20° and 30°(Figure 5.14 (a-f)). Overall, fine sand shows high sensitivity to RI under different conditions, and coarse sand shows the lowest sensitivity to RI.

Models with lower rain intensity show the second-highest sensitivity to variation in slope gradient (δ) (Figures 5.14-16 (a,b)), while increasing the rain intensity increases the sensitivity of the model to variation in slope gradient (δ) for all soil types (fine, medium and coarse). Figures 5.14-16 (e) show that in the highest rain intensity, the model is most sensitive to the variation in δ and D_{50} data. However, the D_{50} has a negative correlation with the probability of failure.

Variation in the water entry value range (Ψ_{wev}) shows an overall lower effect on the model sensitivity analysis within the defined ranges. The Ψ_{wev} are only ranged within positive values since the model is based on the results from hydrophobic samples (hydrophobic samples have a positive water entry value).

Shifting the median grain size (D_{50}) shows no effect on the model for low rain intensities for all sand types, as shown in Figure 5.14-16 (a,b). However, the model negatively correlates with grain size (D_{50}) for higher rain intensities, and model sensitivity increases in steeper slopes.

Fine (D_{50}= 0.2 mm, Ψ_{wev}=1.95 kPa)

20°

30°

18 mm/hr

(a)

(b)

70 mm/hr

(c)

(d)

120 mm/hr

(e)

(f)
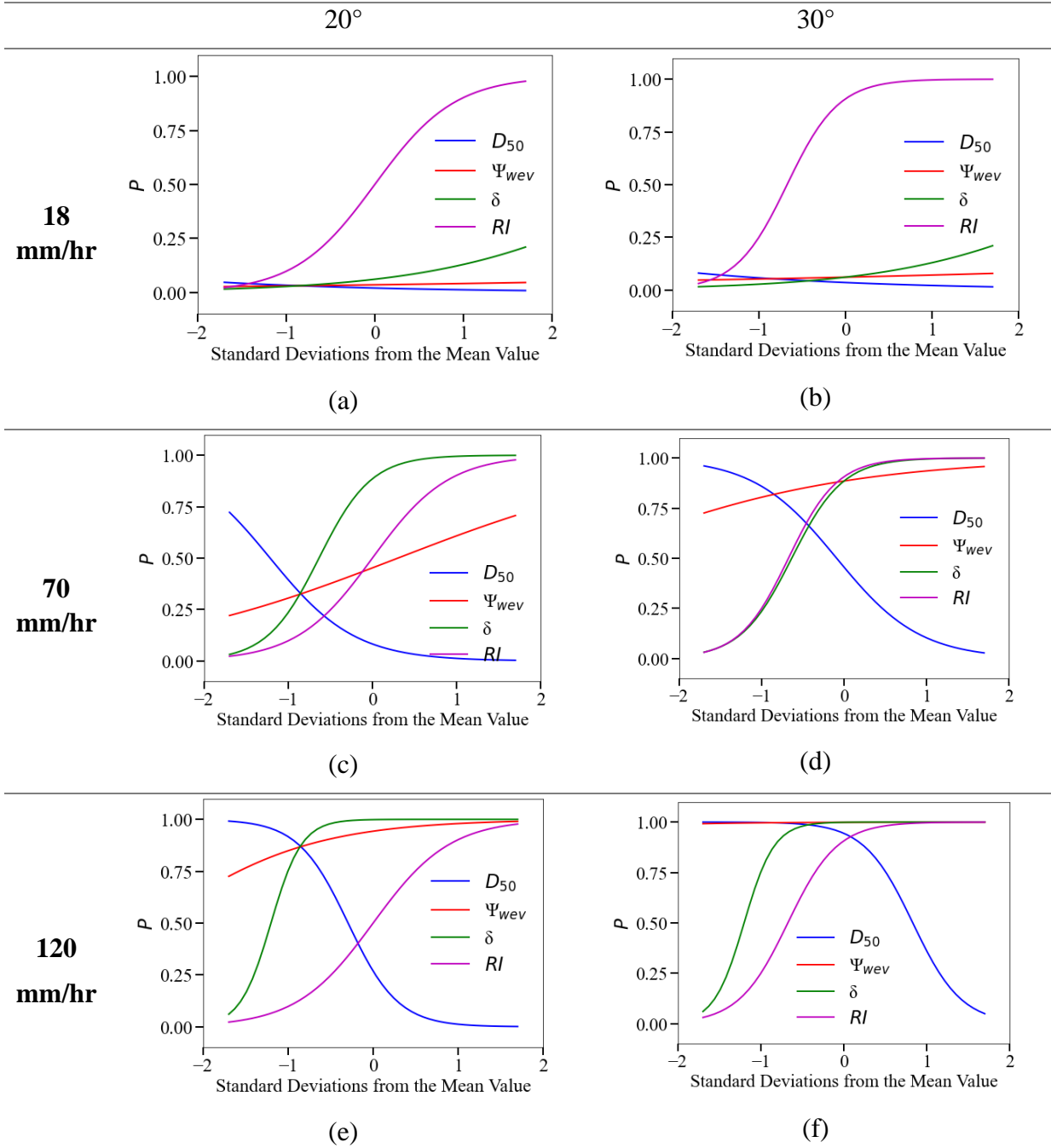
Figure 5.14 Sensitivity analysis results of the tests with fine sand for four features (D_{50}, Ψ_{wev}, δ, RI)

Medium (D_{50}= 0.4 mm, Ψ_{wev}=0.75 kPa)

20°	30°

(a)

(b)

18 mm/hr

(c)

(d)

70 mm/hr

(e)

(f)

120 mm/hr
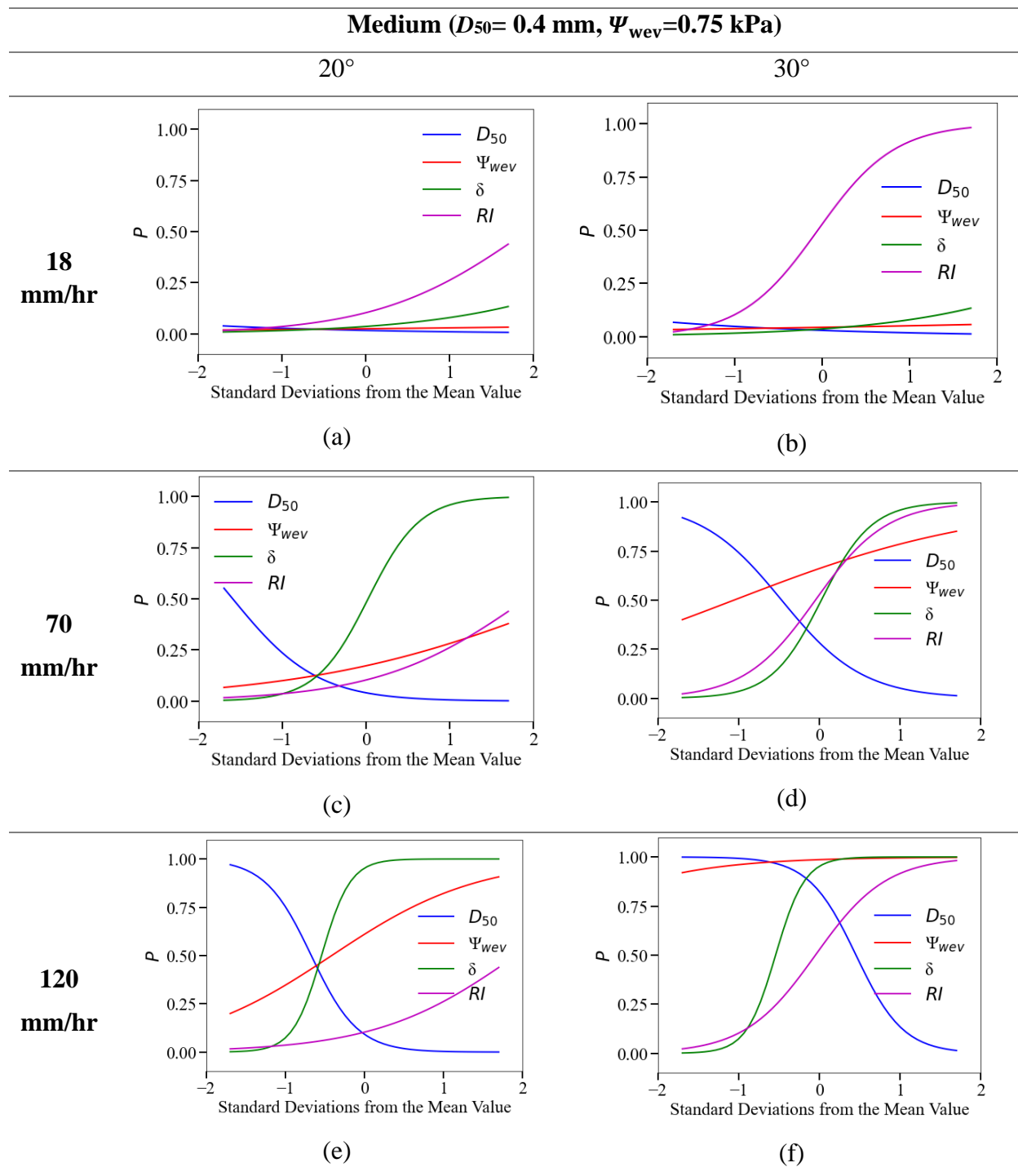
Figure 5.15 Sensitivity analysis results of the tests with medium sand for four features (D_{50}, Ψ_{wev}, δ, RI)

Coarse (D_{50}= 0.65 mm, Ψ_{wev}=0.55 kPa)
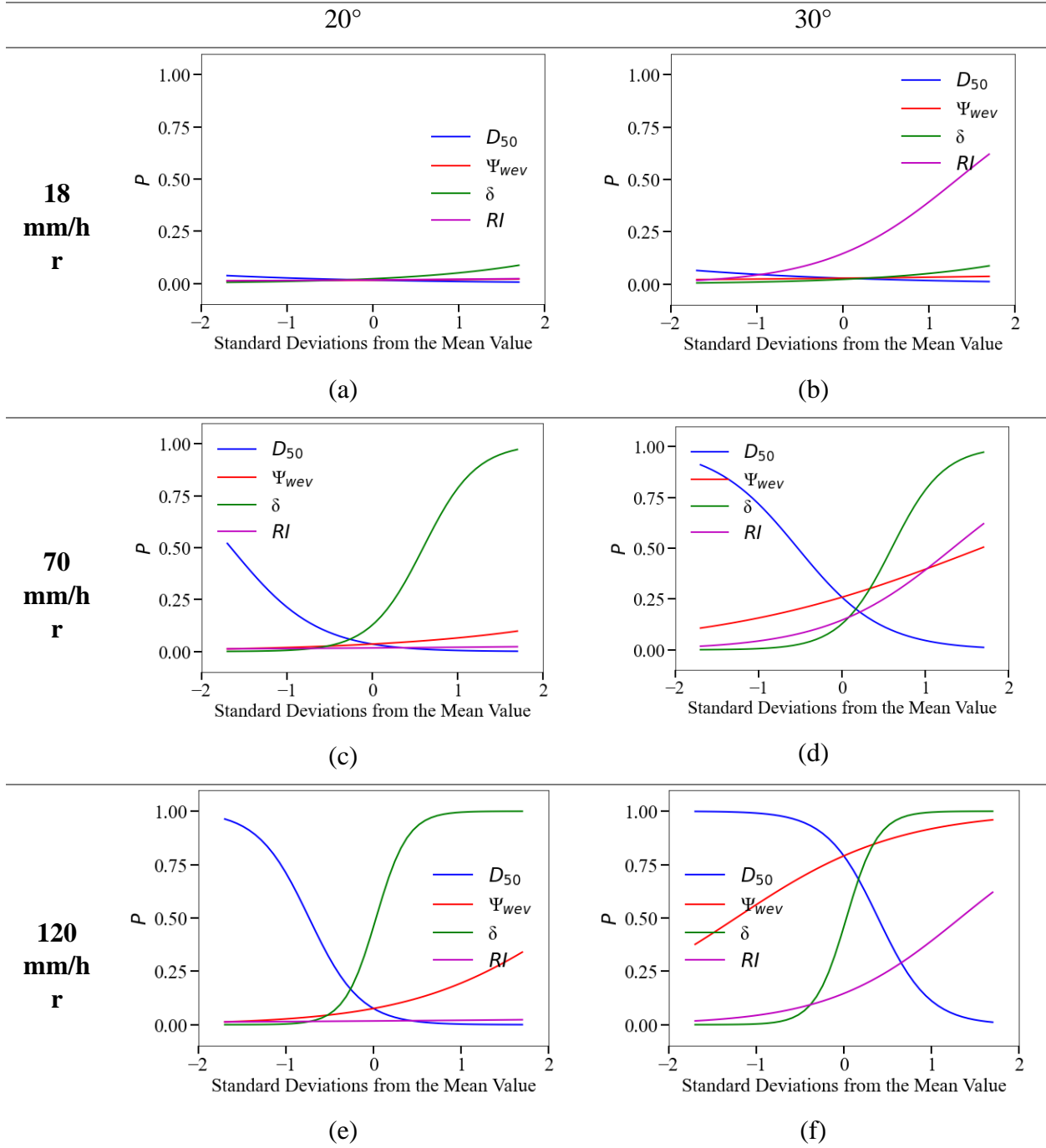
Figure 5.16 Sensitivity analysis results of the tests with coarse sand for four features (D_{50}, Ψ_{wev}, δ, RI)

5.6   Conclusion

In this study, we incorporated different machine learning algorithms and methods to predict and classify the experimental results that were presented in chapter 4 of this dissertation. The experimental results of H-Top layout are used to predict the total erosion and total discharge of the tests under different rain intensities (RI), slope gradients (δ), water entry values (Ψ_{wev}), and median grain sizes (D_{50}). A multiple linear regression (MLR) model was used to conduct the regression. The predictions showed good agreement for total discharge amounts; however, the erosion prediction was less accurate. One of the reasons could be the very low erosion amounts in coarse grain sand and the significant differences in erosion amounts with fine and medium sands.

The experimental results from H-Sub layout are used for binary classification using logistic regression (LR) and support vector classifier (SVC) methods. In addition, the results are clustered by the K-cluster method, and the dimension of input variables was lowered by principal component analysis (PCA). Reducing the dimension of variables improved the visualization of the data while clustering them. Data were clustered into two clusters; cluster 1 for "*Infinite failure*" and cluster 0 for "*No failure*". The clustering results were promising, and the clustered data were in good agreement with experimental outcomes. The support vector classifier (SVC) was developed with a linear kernel and C=1. The model constructed a decision boundary between the two classes of the outcomes. The model was validated using a 7-fold cross-validation approach and run for 5 times to evaluate the model accuracy. SVC model showed a decent performance and could be a good approach to classify a problem with a low amount of data set.

Finally, a logistic regression (LR) model investigated the probability of infinite failure by incorporating four variables rain intensity (RI), slope gradient (δ), water entry value (Ψ_{wev}), and median grain size (D_{50}). The results show that LR model gives promising predictions despite a

small dataset. The sensitivity analysis is performed for each test, and the results show how the four features independently affect the probability of the LR model. Sensitivity analysis is a very efficient method of analyzing the overall effect of the variables on the model outcome. In this study, sensitivity analysis gives a general overview of the results and helps interpret the results more efficiently. For example, we can interpret what the overall effect of rain intensity is and which tests are most affected by it. These interpretations are hard to see in experimental results, and sensitivity analysis highlights the effect of different variables on the data.

The main goal of the machine learning framework in this section is to find a better way to visualize the data and increase the interpretability of the results. The experimental results that were presented in chapter 4, show a coupled effect of rain intensity, slope gradient, and grain size. The ML framework presented in this chapter aims to classify and cluster the experimental data based on these variables and predict the outcome of the experiments and identify the importance of each variable. Although the dataset for ML predictions is very small, and the models could overfit the data, the ML models can help in a wiser selection of the variables and achieving more critical situations.

6. Thesis Conclusions

The scope of this study is to investigate the onset mechanism of debris flow and erosion in post-wildfire areas. The study consists of three stages of experimental work, including the assessment of physical and mechanical properties of naturally and artificially hydrophobic soil, post-impact spread and splash behaviors of a single drop on hydrophobic and regular sand, and finally, rainfall experiments on hydrophobic slopes with varying factors such as slope gradient, layer configuration, rain intensity, and grain size. In addition, a machine learning framework for the experimental data complements the experimental data.

It is concluded that soil water retention curves (SWRC) for hydrophobic samples are highly affected by waiting time and can be an unreliable measure for post-wildfire assessment due to delayed infiltration of water in hydrophobic samples, while flash-floods on inclined hydrophobic surfaces occur fast and no waiting time is expected. On the other hand, water entry tests can be used as an immediate soil measure and show a positive water entry potential for hydrophobic soil that is linearly related to contact angle and inversely related to median grain size (D_{50}). In addition, it is concluded that artificially hydrophobic soil can be used as an alternative to natural post-wildfire hydrophobic soil if the aim is to study the hydrophobic soil right after the fire.

Drop post-impact behavior is affected by the coupled effect of wettability and grain size. Post-impact phases on hydrophobic sand samples include retraction, rebound, oscillations, splash, and fragmentation into droplets, while on regular sand, the drop does not show rebound behavior and has slight retraction. The rebound criterion also shows that rebound tendency is higher in finer hydrophobic sand than in medium and coarse hydrophobic sand samples.

The maximum spread factor (maximum spread diameter/initial drop diameter) is overall higher in all hydrophobic sands compared to the regular samples of the same grain size. The maximum spread factor versus the dimensionless group of *We/Oh* follows the power law of

$\beta_{\text{max}} \approx a \left(\frac{We}{Oh}\right)^b$. The fitting parameter a increases with increasing D_{50} and is approximately $2 \times D_{50}$, while b decreases by increasing D_{50} and could be affected by a combined effect of roughness and wettability.

The non-dimensional splash number versus Re shows that the splashing onset threshold decreases by hydrophobizing the sand. In addition, hydrophobicity caused the most drastic drop in splash initiation threshold in fine sand, while splash in coarse sand is dominated by grain size and not hydrophobicity.

The drop on the inclined surface shows higher mobility in hydrophobic sand than regular sand. Furthermore, the drop on finer hydrophobic sand shows higher mobility, and partial bounces are observed. We conclude that the grain size effect on drop mobility is attributed to Cassie-Baxter and Wenzel wetting regimes, where higher drop velocities and partial bounces are observed in the case of Cassie-Baxter model on fine sands and the velocities dropped about 6.5 times in the case of Wenzel model on coarse sand.

The macro investigation of the effect of hydrophobicity on slope processes is conducted through rainfall experiments on slopes with varied factors related to soil, rainfall condition, and geospatial conditions. It is concluded that the spatial variability of the hydrophobic layer affects the post-wildfire slope processes greatly, such that surficial erosion processes dominate when hydrophobic layer is at the top surface while infinite slope failure mechanism dominates the areas with hydrophobic layer forming a few centimeters below the surface.

Grain size controls the surficial erosion and patterns, from sequin-shape patches in fine sands to channel erosion in coarser sand. Thus, the water discharges in a more controlled condition in a larger grain slope compared to fine sand and imposes less danger. In addition, the surficial erosion in slopes with finer sand starts immediately after rain, while by increasing the grain size,

the erosion process is delayed. Water discharge and erosion rates are higher in finer slope, but the sand particle effect vanishes at low rain intensity. The slope gradient also affects the discharge and erosion rates; however, the coarse sand is not significantly affected by steepness. The water content sensors indicate that the infiltration in fine sand is delayed in higher rain intensities, while the water contents increase immediately in coarser sand. Delayed infiltration leads to a higher discharge and erosion rate in fine sand slopes.

Seepage-induced infinite slope failure is observed in fine and medium slopes with respect to time to failure, sediment discharge, water infiltration, and overflow dynamics. In cases where discharge is much smaller than the infiltration at peak discharge 10-min intervals, slopes remain stable. The infinite failure in finer sand is more critical because the failure can happen in as fast as 2 minutes of the start of rainfall. The failure time increases by increasing the grain size and decreasing the rain intensity. Infinite failure was not observed in coarse grain size tests. Water content measurements show that the infiltration is higher in coarse sand slopes than in medium and fine, attributed to larger pores and lower infiltration resistance.

The machine learning framework comprises classification, clustering, and linear regression models. Machine learning techniques perform better in large datasets; however, in this study, the goal is to synthesize better and visualize the experimental data. The classification and clustering models show good performance and help synthesize the data by classifying and clustering them into two groups of "*No Failure*" and "*Infinite failure*" by using the input variables. The sensitivity of the logistic regression model over a representative range of values for an individual variable shows the diminishing sensitivity to rain intensity in coarser grain. In addition, increasing the rain intensity makes the model more sensitive to grain size and slope gradient. The sensitivity analysis

is beneficial in understanding and interpreting the direct effect of each variable, while this can be hard to detect by directly examining the experimental results.

Overall, in this study, the fine sand is identified as the most problematic and risky sand type in post-wildfire areas in terms of mudflow and debris flow initiation. Fine sand is the most sensitive sand to hydrophobicity and changes drastically in splashing, spreading, and mobility after sand turns hydrophobic. It is shown that the fine sand slope, regardless of the spatial variability of the hydrophobic layer, is the most critical sand in terms of erosion and failure. In addition, the duration of rain is more critical in low-intensity rain than in high-intensity rain. In a high rain intensity, the first 10-minutes of rain is the most critical in terms of discharge, and most of the damage occurs within the initial period. In contrast, the discharged water maintains an almost steady percentage of the total received rain in low-intensity rain. All the observations lead to the conclusion that areas with dominated fine sand could show drastic changes in behavior after a fire, and more precautions should be considered in emergency response and evacuation plans in these areas.

REFERENCES

1. Doerr SH, Shakesby RA, Walsh RPD. Soil water repellency: Its causes, characteristics and hydro-geomorphological significance. Earth Sci Rev. 2000;51(1–4):33–65.

2. Martin DA, Moody JA. Comparison of soil infiltration rates in burned and unburned mountainous watersheds. Hydrol Process. 2001;15(15):2893–903.

3. Westerling AL, Hidalgo HG, Cayan DR, Swetnam TW. Warming and earlier spring increase Western U.S. forest wildfire activity. Science. 2006;313(5789):940–3.

4. Debano LF. Water repellent soils: a state-of-the-art. United States Dep Agric Gen Tech Rep PSW-GTR-46. 1981;1–21.

5. Debano LF. The role of fire and soil heating on water repellency in wildland environments: a review. J Hydrol [Internet]. 2000;231–232(0):195–206. Available from: http://www.sciencedirect.com/science/article/pii/S0022169400001943

6. Leelamanie DAL, Karube J, Yoshida A. Characterizing water repellency indices: Contact angle and water drop penetration time of hydrophobized sand. Soil Sci Plant Nutr. 2008;54(2):179–87.

7. Debano LF, Krammes JS. Water repellent soils and their relation to wildfire temperatures. Int Assoc Sci Hydrol Bull. 1966;11(2):14–9.

8. Scott DF, Van Wyk DB. The effects of wildfire on soil wettability and hydrological behavior of afforested chatchement. J Hydrol.1990;118:239–56.

9. Cannon SH, Bigio ER, Mine E. A process for fire-related debris flow initiation, Cerro Grande fire, New Mexico. Hydrol Process. 2001;15(15):3011–23.

10. Jordan P, Covert SA. Debris flows and floods following the 2003 wildfires in Southern British Columbia. Environ Eng Geosci. 2009;15(4):217–34.

11. Nyman P, Sheridan GJ, Smith HG, Lane PNJ. Evidence of debris flow occurrence after wildfire in upland catchments of south-east Australia. Geomorphology [Internet]. 2011;125(3):383–401. Available from: http://dx.doi.org/10.1016/j.geomorph.2010.10.016

12. Tiwari B, Ajmera B, Gonzalez A, Sonbol H. Impact of Wildfire on Triggering Mudslides—A Case Study of 2018 Montecito Debris Flows. In: Geo-Congress 2020 In : Engineering, Monitoring, and Management of Geotechnical Infrastructure. Reston, VA: American Society of Civil Engineering; 2020. p. 40–9.

13. Wells W. DEBRIS FLOWS / AVALANCHES : 1987;7:105–14.

14. Bond RD, Harris JR. The influence of the microflora on the physical properties of soils. I. effects associated with filamentous algae and fungi. Aust J Soil Res. 1964;2(1):111–23.

15. Doerr SH, Thomas AD. The role of soil moisture in controlling water repellency: New evidence from forest soils in Portugal. J Hydrol. 2000;231:134–47.

16. Jex GW, Bleakley BH, Hubbell DH, Munro LL. High humidity-induced increase in water repellency in some sandy soils. Soil Sci Soc Am J. 1985;49(5):1177–82.

17. Witter J V., Jungerius PD, Ten Harkel MJ. Modelling water ersoin and the impact of water repellnecy. Catena. 1991;18(2):115–24.

18. Granged AJP, Jordán A, Zavala LM, Muñoz-Rojas M, Mataix-Solera J. Short-term effects of experimental fire for a soil under eucalyptus forest (SE Australia). Geoderma. 2011;167–168:125–34.

19. Hallett PD, Young IM. Changes to water repellence of soil aggregates caused by substrate-induced microbial activity. Eur J Soil Sci. 1999;50(1):35–40.

20. Mao J, Nierop KGJ, Dekker SC, Dekker LW, Chen B. Understanding the mechanisms of soil water repellency from nanoscale to ecosystem scale: a review. J Soils Sediments. 2019;19(1):171–85.

21. Boinovich LB, Emelyanenko AM. Hydrophobic materials and coatings: principles of design, properties and applications. Russ Chem Rev. 2008;77(7):583–600.

22. Asadi H, Moussavi A, Ghadiri H, Rose CW. Flow-driven soil erosion processes and the size selectivity of sediment. J Hydrol [Internet]. 2011;406(1–2):73–81. Available from: http://dx.doi.org/10.1016/j.jhydrol.2011.06.010

23. Rose CW, Yu B, Ghadiri H, Asadi H, Parlange JY, Hogarth WL, et al. Dynamic erosion of soil in steady sheet flow. J Hydrol. 2007;333(2–4):449–58.

24. Cannon SH, Gartner JE, Wilson RC, Bowers JC, Laber JL. Storm rainfall conditions for floods and debris flows from recently burned areas in southwestern Colorado and southern California. Geomorphology. 2008;96(3–4):250–69.

25. Vieira DCS, Fernández C, Vega JA, Keizer JJ. Does soil burn severity affect the post-fire runoff and interrill erosion response? A review based on meta-analysis of field rainfall simulation data. J Hydrol. 2015;523:452–64.

26. Liu D, Sandeep CS, Senetakis K, Nardelli V, Lourenço SDN. Micromechanical behaviour of a polymer-coated sand. Powder Technol. 2019;347:76–84.

27. Liu D, Lourenço SDN. Stress-dilatancy behaviour of a polymer-coated sand. Acta Geotech. 2021;16(2):647–52.

28. Beckett C, Fourie A, Toll D. Water repellent soils: The case for unsaturated soil mechanics. Vol. 9, E3S Web of Conferences. EDP Sciences; 2016. 11011 p.

29. Czachor H, Doerr SH, Lichner L. Water retention of repellent and subcritical repellent soils:

New insights from model and experimental investigations. J Hydrol. 2010;380(1–2):104–11.

30. Wang Z, Wu QJ, Wu L, Ritsema CJ, Dekker LW, Feyen J. Effects of soil water repellency on infiltration rate and flow instability. J Hydrol . 2000;232:265–76.

31. Byun YH, Khoa Tran M, Yun TS, Lee JS. Strength and stiffness characteristics of unsaturated hydrophobic granular media. Geotech Test J. 2012;35(1):193–200.

32. Kern JS. Evaluation of Soil Water Retention Models Based on Basic Soil Physical Properties. Soil Sci Soc Am J. 2010;59(4):1134.

33. Marmur A. Penetration and displacement in capillary systems of limited size. Adv Colloid Interface Sci. 1992;39(C):13–33.

34. Leong EC, Rahardjo H. Review of soil-water characteristic curve equations. J Geotech Eng. 1997;123(12):1106–17.

35. Ahmad-Adli M, Huvaj N, Kartal Toker N. Effects of the size of particles on rainfall-induced slope instability in granular soils. Geotech Spec Publ. 2014;(234 GSP):4027–36.

36. Liu H, Ju Z, Bachmann J, Horton R, Ren T. Moisture-Dependent Wettability of Artificial Hydrophobic Soils and Its Relevance for Soil Water Desorption Curves. Soil Sci Soc Am J. 2012;76(2):342–9.

37. Bauters TWJ, Steenhuis TS, Dicarlo DA, Nieber JL, Dekker LW, Ritsema CJ, et al. Physics of water repellent soils. J Hydrol. 2000;231:233–43.

38. Bachmann J, Deurer M, Arye G. Modeling water movement in heterogeneous water-repellent soil: 1. Development of a contact angle-dependent water-retention model. Vadose Zo J. 2007;6(3):436–45.

39. Miyamoto S, Letey J. Determination of solid-air surface tension of porous media. Soil Sci Soc Am. 1971;35(6):856–9.

40. Chieng BW, Ibrahim NA, Ahmad Daud N, Talib ZA. Functionalization of Graphene Oxide via Gamma-Ray Irradiation for Hydrophobic Materials. In: Synthesis, Technology and Applications of Carbon Nanomaterials. Elsevier Inc.; 2019. p. 177–203.

41. Ragesh P, Anand Ganesh V, Nair S V., Nair AS. A review on "self-cleaning and multifunctional materials." J Mater Chem A. 2014;2(36):14773–97.

42. Feng GL, Letey J, Wu L. Water Ponding Depths Affect Temporal Infiltration Rates in a Water-Repellent Sand. Soil Sci Soc Am J. 2001;65(2):315–20.

43. Letey J. Causes and consequences of fire-induced soil water repellency. Hydrol Process. 2001;15(15):2867–75.

44. Leelamaanie DAL, Karube J. Effects of hydrophobic and hydrophilic organic matter on the water repellency of model sandy soils. Soil Sci Plant Nutr. 2009;55(4):462–7.

45. Kleber M, Sollins P, Sutton R. A conceptual model of organo-mineral interactions in soils: Self-assembly of organic molecular fragments into zonal structures on mineral surfaces. Biogeochemistry. 2007;85(1):9–24.

46. Nicita E, Halverson E. Holy Fire Burned Area Emergency Response Soil Resource Report.

47. Karim MZ, Tucker-Kulesza SE, Derby MM. Synthesizing Hydrophobic Sand and Comparison of Shear Strength Properties with Hydrophilic Sand. In IFCEE. 2018;75–83.

48. Saulick Y, Lourenço SDN, Baudet BA. Optimising the hydrophobicity of sands by silanisation and powder coating. Geotechnique. 2021;71(3):250–9.

49. Chan CSH, Lourenço SDN. Comparison of three silane compounds to impart water repellency in an industrial sand. Geotech Lett. 2016;6(4):263–6.

50. Ng SHY, Lourenço SDN. Conditions to induce water repellency in soils with dimethyldichlorosilane. Geotechnique. 2016;66(5):441–4.

51. Lee C, Yang H-J, Yun TS, Choi Y, Yang S. Water-Entry Pressure and Friction Angle in an Artificially Synthesized Water-Repellent Silty Soil. Vadose Zo J. 2015;14(4):0.

52. ASTM International. D6836-16 Standard Test Methods for Determination of the Soil Water Characteristic Curve for Desorption Using Hanging Column, Pressure Extractor, Chilled Mirror Hygrometer, or Centrifuge. ASTM International West Conshohocken, PA; 2016.

53. Wang Z, Wu L, Wu QJ. Water-entry value as an alternative indicator of soil water-repellency and wettability. J Hydrol. 2000;231:76–83.

54. Keatts MI, Daniels JL, Langley WG, Pando MA, Ogunro VO. Apparent Contact Angle and Water Entry Head Measurements for Organo-Silane Modified Sand and Coal Fly Ash. J Geotech Geoenvironmental Eng. 2018;144(6):04018030.

55. Kim D, Yang HJ, Yun TS, Kim B, Kato S, Park SW. Characterization of geomechanical and hydraulic properties of non-wettable sands. In: 18th International Conference on Soil Mechanics and Geotechnical Engineering. French Society for Soil Mechanics and Geotechnical Engineering,Paris; 2013. p. 361–4.

56. Movasat M, Tomac I. Post-Fire Mudflow Prevention by Biopolymer Treatment of Water Repellent Slopes. In: In Geo-Congress 2020: Biogeotechnics. Reston, VA: American Society of Civil Engineers; 2020. p. 170–8.

57. Annaka T, Hanayama S. Effects of contact angle on fingered flow during non-ponding infiltration into dry sand layers. Soil Sci Plant Nutr. 2010;56(3):366–70.

58. Ritsema CJ, Dekker LW. Modeling implications of preferential flow in water repellent

sandy soils. In: Soil Water Repellency: Occurrence, Consequences, and Amelioration' c. 2003. p. 259–69.

59. Byun Y, Lee J. Influence of Particle Shape of Hydrophobic Granular Materials on Shear Strength. In: Advances in Civil, Environmental, and Materials Research. Seoul, Korea; 2012.

60. Tatar HM. Consolidated undrained shearing response of hydrophobic sands. MIDDLE EAST TECHNICAL UNIVERSITY. 2018.

61. Yang HW, Lourenço SDN, Xing X. Grain surface analysis of a hydrophobized sand: Thickness estimation of the soft coating layer. Powder Technol. 2021;377:827–31.

62. Terry JP, Shakesby RA. Soil hydrophobicity effects on rainsplash: Simulated rainfall and photographic evidence. Earth Surf Process Landforms. 1993;18(6):519–25.

63. Yarin AL. Drop impact dynamics: Splashing, spreading, receding, bouncing. Annu Rev Fluid Mech. 2006;38:159–92.

64. Hamlett CAE, Atherton S, Shirtcliffe NJ, Mchale G, Ahn S, Doerr SH, et al. Transitions of water-drop impact behaviour on hydrophobic and hydrophilic particles. Eur J Soil Sci. 2013;64(3):324–33.

65. Rioboo R, Tropea C, Marengo M. Outcomes from a drop impact on solid surfaces. At sprays. 2001;(11(2)).

66. Mao T, Kuhn DCS, Tran H. Spread and Rebound of Liquid Droplets upon Impact on Flat Surfaces. AIChE J. 1997;43(9):2169–79.

67. Ukiwe C, Kwok DY. On the maximum spreading diameter of impacting droplets on well-prepared solid surfaces. Langmuir. 2005;21(2):666–73.

68. Roisman I V. Inertia dominated drop collisions. II. An analytical solution of the Navier-Stokes equations for a spreading viscous film. Phys Fluids. 2009;21(5).

69. Clanet C, Béguin C, Richard D, Quéré D. Maximal deformation of an impacting drop. J Fluid Mech. 2004;517:199–208.

70. Clanet C, Béguin C, Richard D, Quéré D. Maximal deformation of an impacting drop ´. J Fluid Mech. 2004;517:199–208.

71. Bayer IS, Megaridis CM. Contact angle dynamics in droplets impacting on flat surfaces with different wetting characteristics. J Fluid Mech.2006; Vol. 558: 415–449 p.

72. Wang F, Yang L, Wang L, Zhu Y, Fang T. Maximum Spread of Droplet Impacting onto Solid Surfaces with Di ff erent Wettabilities: Adopting a Rim − Lamella Shape. Langmuir. 2019;35(8):3204-3214.

73. Lin S, Zhao B, Zou S, Guo J, Wei Z, Chen L. Journal of Colloid and Interface Science Impact of viscous droplets on different wettable surfaces : Impact phenomena , the maximum spreading factor , spreading time and post-impact oscillation. J Colloid Interface Sci [Internet]. 2018;516:86–97. Available from: https://doi.org/10.1016/j.jcis.2017.12.086

74. Wildeman S, Visser CW, Sun C, Lohse D. On the spreading of impacting drops. J Fluid Mech. 2016;636–655.

75. Pasandideh-Fard M, Qiao YM, Chandra S, Mostaghimi J. Capillary effects during droplet impact on a solid surface. Phys fluids. 1996;8(3):650–9.

76. Zhang H, Zhang X, Yi X, He F, Niu F, Hao P. Effect of wettability on droplet impact : Spreading and splashing. Exp Therm Fluid Sci [Internet]. 2021;124(November 2020):110369. Available from: https://doi.org/10.1016/j.expthermflusci.2021.110369

77. Roisman I V. Inertia dominated drop collisions . II . An analytical solution of the Navier – Stokes equations for a spreading viscous film. Phys Fluids. 2010;052104(May 2009).

78. Lee JB, Laan N, Bruin KG De, Skantzaris G, Shahidzadeh N. Universal rescaling of drop impact on smooth and rough surfaces. J Fluid Mech. 2016;1–11.

79. Tang C, Qin M, Weng X, Zhang X, Zhang P. International Journal of Multiphase Flow Dynamics of droplet impact on solid surface with different roughness. Int J Multiph Flow [Internet]. 2017;96:56–69. Available from: http://dx.doi.org/10.1016/j.ijmultiphaseflow.2017.07.002

80. Nefzaoui E, Skurtys O. Impact of a liquid drop on a granular medium : Inertia , viscosity and surface tension effects on the drop deformation. Exp Therm Fluid Sci [Internet]. 2012;41:43–50. Available from: http://dx.doi.org/10.1016/j.expthermflusci.2012.03.007

81. Ahn S, Doerr SH, Douglas P, Bryant R, Hamlett CAE, Mchale G, et al. Effects of hydrophobicity on splash erosion of model soil particles by a single water drop impact. Earth Surf Process Landforms. 2013;38(11):1225–33.

82. Bordbar A, Taassob A, Khojasteh D, Marengo M, Kamali R. Maximum Spreading and Rebound of a Droplet Impacting onto a Spherical Surface at Low Weber Numbers. Langmuir. 2018;34(17):5149–58.

83. Zhao S, Jong R De, Meer D Van Der. Liquid-Grain Mixing Suppresses Droplet Spreading and Splashing during Impact. Phys Rev Lett. 2017;118(5):054502.

84. Zhao R, Zhang Q, Tjugito H, Cheng X. Granular impact cratering by liquid drops : Understanding raindrop imprints through an analogy to asteroid strikes. Proc National Academy Sci. 2015;112(2), 324-347.

85. Supakar T, Kumar A, Marston JO. Impact dynamics of particle-coated droplets. Phys Rev E. 2017;95(1):013106.

86.	Liu D, Tan H. Soft Matter. Soft Matter [Internet]. 2018;14:9967–72. Available from: http://dx.doi.org/10.1039/C8SM01858H

87.	Katsuragi H. Morphology Scaling of Drop Impact onto a Granular Layer. Phys Rev Lett. 2010;218001(May):1–4.

88.	Delon G, Terwagne D, Dorbolo S, Vandewalle N, Caps H. Impact of liquid droplets on granular media. Phys Rev E. 2011;84(4):046320.

89.	Mozhi Devan Padmanathan, Arul and Sneha Ravi, Apoorva and Choudhary, Hema and Varanakkottu SN and D, V S. Predictive Framework for the Spreading of Liquid Drops and the Formation of Liquid Marbles on Hydrophobic Particle Bed. Langmuir. 2019;35(20):6657–68.

90.	Tsai P, Pacheco S, Pirat C, Lefferts L, Lohse D. Drop impact upon micro- and nanostructured superhydrophobic surfaces. Langmuir. 2009;25(20):12293–8.

91.	Tsai P, Hendrix MHW, Dijkstra RRM, Shui L, Lohse D. Microscopic structure influencing macroscopic splash at high Weber number. Soft Matter. 2011;7(24):11325–33.

92.	Chen L, Xiao Z, Chan PCH, Lee YK, Li Z. A comparative study of droplet impact dynamics on a dual-scaled superhydrophobic surface and lotus leaf. Appl Surf Sci. 2011;257(21):8857–63.

93.	Cassie ABD, Baxter S. Wettability of porous surfaces. Trans Faraday Soc. 1944;(40):546–51.

94.	Wenzel RN. Resistance of solid surfaces to wetting by water. Ind Eng Chem. 1936;28(8):988–94.

95.	Bachmann J, McHale G. Superhydrophobic surfaces: A model approach to predict contact angle and surface energy of soil particles. Eur J Soil Sci. 2009;60(3):420–30.

96.	Young T. III. An essay on the cohesion of fluids. Philos Trans R Soc London. 1805;95:65–87.

97.	Lardier N, Roudier P, Clothier B, Willmott G. High-speed photography of water drop impacts on sand. Eur J Soil Sci. 2019;(March):245–56.

98.	Holsapple KA. The scaling of impact processes in planetary sciences. Annu Rev Earth Planet Sci. 1993;21(1):333–73.

99.	Jong R De, Zhao S. Crater formation during raindrop impact on sand. Phys Rev E. 2017;95(4):042901.

100.	Wyser E, Carrea D, Jaboyedoff M, Pudasaini SP. Cratering response during droplet impacts on granular beds. Eur Physc J E.2019;42(8):1-11.

101. Šikalo Š, Tropea C, Gani EN. Impact of droplets onto inclined surfaces.J Coll Interface Sci. 2005;286(2):661–669.

102. Aboud DGK, Kietzig A. Splashing Threshold of Oblique Droplet Impacts on Surfaces of Various Wettability. Langmuir. 2015;31(36):10100-10111.

103. Leclear S, Leclear J, Park K, Choi W. Journal of Colloid and Interface Science Drop impact on inclined superhydrophobic surfaces. J Colloid Interface Sci [Internet]. 2016;461:114–21. Available from: http://dx.doi.org/10.1016/j.jcis.2015.09.026

104. Marengo CAFVM. Oblique impacts of water drops onto hydrophobic and superhydrophobic surfaces : outcomes , timing , and rebound maps. Exp Fluids. 2014;55(4):1-9.

105. Aboud DGK, Wood MJ, Kietzig A. Influence of liquid properties on the oblique splashing threshold of drops. Phys Fluids [Internet]. 2020;061402(June). Available from: https://doi.org/10.1063/5.0011148

106. Yeong YH, Burton J, Loth E, Bayer IS. Drop Impact and Rebound Dynamics on an Inclined Superhydrophobic Surface. Langmuir. 2014;30(4)- 12021-12038.

107. Hayashi K, Sumita I. Low-velocity impact cratering experiments in granular slopes. Icarus [Internet]. 2017;291:160–75. Available from: http://dx.doi.org/10.1016/j.icarus.2017.03.027

108. Aussillous P, Quéré D. Liquid marbles. Nature. 2001;411(June):924–7.

109. Wang R, Li X. On the effective surface tension of powder-derived liquid marbles. Powder Technol [Internet]. 2020;367:608–15. Available from: https://doi.org/10.1016/j.powtec.2020.04.028

110. Bachmann J, Horton R, Van Der Ploeg R, Woche S. Modified sessile drop method for assessing initial soil--water contact angle of sandy soil. Soil Sci Soc Am J. 2000;64(2):564–7.

111. van Boxel JH. Numerical model for the fall speed of rain drops in a rain fall simulator. Work Wind water Eros. 1997;5:77–85.

112. Blake TD, De Coninck J. The influence of solid-liquid interactions on dynamic wetting. Adv Colloid Interface Sci. 2002;96(1–3):21–36.

113. Roisman I V., Berberović E, Tropea C. Inertia dominated drop collisions. I. On the universal flow in the lamella. Phys Fluids. 2009;21(5).

114. Tang C, Qin M, Weng X, Zhang X, Zhang P, Li J, et al. Dynamics of droplet impact on solid surface with different roughness. Int J Multiph Flow. 2017;96:56–69.

115. Marston JO, Sprittles JE, Zhu Y, Li EQ, Vakarelski IU, Thoroddsen ST. Drop spreading

and penetration into pre-wetted powders. Powder Technol. 2013;239:128–36.

116. Beard K V. Terminal velocity and shape of cloud and precipitation drops aloft. J Atmos Sci. 1976;33(5):851–64.

117. Palacios J, Hernández J, Gómez P, Zanzi C, López J. Experimental study of splashing patterns and the splashing/deposition threshold in drop impacts onto dry smooth solid surfaces. Exp Therm Fluid Sci. 2013;44:571–82.

118. Park H, Carr WW, Morris JF, Services HE. Single Drop Impaction on a Solid Surface. AIChE J. 2003;49(10).

119. Gennes D. Wetting: statics and dynamics. Rev Mod Phys. 1985;57(3).

120. Chen HX, Wang JD. Regression analyses for the minimum intensity-duration conditions of continuous rainfall for mudflows triggering in Yan'an, northern Shaanxi (China). Bull Eng Geol Environ. 2014;73(4):917–28.

121. Ritsema CJ, Dekker LW (Eds.). Soil water repellency: Occurrence, consequences, and amelioration. Elsevier; 2012.

122. Savage SM, Osborn J, Letey J, Heaton C. Substances contributing to fire-induced water repellency in soils. So, 36(4), 674-678. Soil Sci Soc Am J. 1972;36(4):674–8.

123. Doerr SH, Shakesby RA, Dekker LW, Ritsema CJ. Occurrence, prediction and hydrological effects of water repellency amongst major soil and land-use types in a humid temperate climate. Eur J Soil Sci. 2006;57(5):741–54.

124. Busse MD, Shestak CJ, Hubbert KR, Knapp EE. Soil Physical Properties Regulate Lethal Heating during Burning of Woody Residues. Soil Sci Soc Am J. 2010;74(3):947–55.

125. Arocena JM, Opio C. Prescribed fire-induced changes in properties of sub-boreal forest soils. Geoderma. 2003;113(1–2):1–16.

126. DeBano LF, Rice RM, Conrad CE. Soil Heating in Chaparral Fires : effects on soil properties, plant nutrients, erosion, and runnoff. USDA For Serv Res Pap PSW-145. 1979;1–21.

127. Kean JW, Staley DM, Cannon SH. In situ measurements of post-fire debris flows in southern California: Comparisons of the timing and magnitude of 24 debris-flow events with rainfall and soil moisture conditions. J Geophys Res Earth Surf. 2011;116(4):1–21.

128. CBS SF BAY Area. Mudslides Damage Up To 2 Dozen Structures In Monterey County; Flash Flood Warning Issued. 2021 CBS Broadcasting Inc. 2021.

129. ABC 7. Highway 38 near Big Bear reopens after mud, debris flow forced closure. 2021 KABC Television, LLC. 2021.

130. Kean JW, Staley DM, Lancaster JT, Rengers FK, Swanson BJ, Coe JA, et al. Inundation, flow dynamics, and damage in the 9 January 2018 Montecito debris-flow event, California, USA: Opportunities and challenges for post-wildfire risk assessment. Geosphere. 2019;15(4):1140–63.

131. Wells CG. Effects of fire on soil: a state-of-knowledge review. In Department of Agriculture, Forest Service; 1979.

132. DeBano LF, Savage SM, Hamilton DA. The transfer of heat and hydrophobic substances during burning. Soil Sci Soc Am J. 1976;40(5):779–82.

133. Scholl DG. Soil wettability and fire in Arizona chaparral. Soil Sci Soc Am J. 1975;39(2):356–61.

134. Robichaud PR, Hungerford RD. Water repellency by laboratory burning of four northern Rocky Mountain forest soils. J Hydrol. 2000;232:207–19.

135. Chen J, McGuire KJ, Stewart RD. Effect of soil water-repellent layer depth on post-wildfire hydrological processes. Hydrol Process. 2020;34(2):270–83.

136. Robichaud PR, Wagenbrenner JW, Pierson FB, Spaeth KE, Ashmun LE, Moffet CA. Catena In fi ltration and interrill erosion rates after a wild fi re in western. Catena. 2016;142:77–88.

137. Cannon SH, Boldt EM, Laber JL, Kean JW, Staley DM. Rainfall intensity-duration thresholds for postfire debris-flow emergency-response planning. Nat Hazards. 2011;59(1):209–36.

138. Cannon SH, Kirkham RM, Parise M. Wildfire-related debris-flow initiation processes ,. Geomorphology. 2001;39:171–88.

139. Cannon SH, Gartner JE, Parrett C, Parise M. Wildfire-related debris-flow generation through episodic progressive sediment-bulking processes, western USA. 2003;(October).

140. Wischmeier WH, Smith DD. Predicting rainfall erosion losses: a guide to conservation planning. Vol. 537, Department of Agriculture, Science and Education Administration. 1978.

141. Renard KG, Foster GR, Weesies GA, Mccool DK, Yoder DC. Predicting soil erosion by water: A guide to conservation planning with Revised Universal Soil Loss Equation (RULSE). Agriculture handbook. 1996;703:23.

142. Morgan RPC. A simple approach to soil loss prediction: A revised Morgan-Morgan-Finney model. Catena. 2001;44(4):305–22.

143. Benda L, James C, Miller D, Andras K. Road Erosion and Delivery Index (READI): A model for evaluating unpaved road erosion and stream sediment delivery. JAWRA J Am Water Resour Assoc. 2019;55(2):459–84.

144. Ciampalini R, Follain S, Le Bissonnais Y. LandSoil: A model for analysing the impact of erosion on agricultural landscape evolution. Geomorphology. 2012;175–176:25–37.

145. Kirkby MJ, Irvine BJ, Jones RJA, Govers G, Boer M, Cerdan O, et al. The PESERA coarse scale erosion model for Europe. I. - Model rationale and implementation. Eur J Soil Sci. 2008;59(6):1293–306.

146. Fernández C, Vega JA. Evaluation of RUSLE and PESERA models for predicting soil erosion losses in the first year after wildfire in NW Spain. Geoderma. 2016;273:64–72.

147. McGuire LA, Youberg AM. What drives spatial variability in rainfall intensity-duration thresholds for post-wildfire debris flows? Insights from the 2018 Buzzard Fire, NM, USA. Landslides. 2020;17(10):2385–99.

148. Karamesouti M, Petropoulos GP, Papanikolaou ID, Kairis O, Kosmas K. Erosion rate predictions from PESERA and RUSLE at a Mediterranean site before and after a wildfire: Comparison & implications. Geoderma. 2016;261:44–58.

149. Lopes AR, Girona-García A, Corticeiro S, Martins R, Keizer JJ, Vieira DCS. What is wrong with post-fire soil erosion modelling? A meta-analysis on current approaches, research gaps, and future directions. Earth Surf Process Landforms. 2021;46(1):205–19.

150. Movasat M, Tomac I. Assessment of Physical Properties of Water-Repellent Soils. J Geotech Geoenvironmental Eng. 2021;147(9):06021010.

151. Lourenço SDN, Wang G, Kamai T. Processes in model slopes made of mixtures of wettable and water repellent sand : Implications for the initiation of debris fl ows in dry slopes. Eng Geology. 2015;196:47–58.

152. Zheng S, Lourenço SDN, Cleall PJ, Fong T, Chui M, Ng AKY, et al. Hydrologic behavior of model slopes with synthetic water repellent soils. J Hydrol. 2017;554:582–99.

153. L.F D. The role of fire and soil heating on water repellDoerr, S. H., Shakesby, R. A., & Walsh, R. P. D. (2000). Soil water repellency: Its causes, characteristics and hydro-geomorphological significance. Earth Science Reviews, 51(1–4), 33–65. https://doi.org/10. J Hydrol [Internet]. 2000;231–232(0):195–206. Available from: http://www.sciencedirect.com/science/article/pii/S0022169400001943

154. Doerr SH, Shakesby RA, Blake WH, Chafer CJ. Effects of differing wildfire severities on soil wettability and implications for hydrological response. J Hydrol. 2006;319:295–311.

155. Staley DM, Negri JA, Kean JW, Laber JL, Tillery AC, Youberg AM. Geomorphology Prediction of spatially explicit rainfall intensity – duration thresholds for post- fi re debris-fl ow generation in the western United States. Geomorphology [Internet]. 2017;278:149–62. Available from: http://dx.doi.org/10.1016/j.geomorph.2016.10.019

156. Guzzetti F, Peruccacci S, Rossi M, Stark CP. The rainfall intensity–duration control of shallow landslides and debris flows: an update. Landslides. 2008;5(1):3–17.

157. Staley DM, Kean JW, Cannon SH, Schmidt KM, Laber JL. Objective definition of rainfall intensity – duration thresholds for the initiation of post-fire debris flows in southern California. Landslides. 2013;10(5):547–62.

158. Zhang YD, Park JS, Gao S, Sonta A, Horin B, Buscarnera G. Effect of Grain Crushing and Grain Size on the Evolution of Water Retention Curves. In PanAm unsat soils. 2017;268–78.

159. Goh ATC, Zhang WG. An improvement to MLR model for predicting liquefaction-induced lateral spread using multivariate adaptive regression splines. Eng Geol [Internet]. 2014;170:1–10. Available from: http://dx.doi.org/10.1016/j.enggeo.2013.12.003

160. Wang L, Wu C, Gu X, Liu H, Mei G, Zhang W. Probabilistic stability analysis of earth dam slope under transient seepage using multivariate adaptive regression splines. Bull Eng Geol and Environ. 2020;2763–75.

161. Zhang W, Li H, Li Y, Liu H, Chen Y. Application of deep learning algorithms in geotechnical engineering : a short critical review [Internet]. Vol. 54, Artificial Intelligence Review. Springer Netherlands; 2021. 5633–5673 p. Available from: https://doi.org/10.1007/s10462-021-09967-1

162. El Naqa I, Li R, Murphy MJ. Machine Learning in Radiation Oncology. Springer; 2015.

163. Goh ATC, Zhang W, Zhang Y, Xiao Y, Xiang Y. Determination of earth pressure balance tunnel-related maximum surface settlement : a multivariate adaptive regression splines approach. Bull Eng Geol Environ. 2018;77(2):489–500.

164. Zhang W, Wu C, Li Y, Wang L, Samui P. Assessment and Management of Risk for Engineered Systems and Geohazards Assessment of pile drivability using random forest regression and multivariate adaptive regression splines. Georisk-Assessment Manag Risk Eng Syst Geohazards [Internet]. 2019; Available from: https://doi.org/10.1080/17499518.2019.1674340

165. Bhattacharya B, Solomatine DP. Machine learning in soil classification. 2006;19:186–95.

166. Goh ATC. Neural Networks for Evaluating CPT Calibration Chamber Test Data.Computer Aided Civil and Infra Struc Eng, 1995;10:147–51.

167. Erzin Y, Cetin T. Computers & Geosciences The prediction of the critical factor of safety of homogeneous finite slopes using neural networks and multiple regressions. Comput Geosci [Internet]. 2013;51:305–13. Available from: http://dx.doi.org/10.1016/j.cageo.2012.09.003

168. Cui Y, Cheng D. Investigation of Post-Fire Debris Flows in Montecito. Int J Geo-Inf. 2018;8(1):5.

169. Bui DT, Moayedi H, Gör M, Jaafari A. Predicting Slope Stability Failure through Machine Learning Paradigms. Int J Geo-Inf .2019;8(9):395.

170. Wilder BA, Lancaster JT, Cafferata PH, Coe DB, Swanson BJ, Lindsay DN, et al. An analytical solution for rapidly predicting post-fire peak streamflow for small watersheds in southern California. Hydrol Process. 2021;35(1):e13976.

171. Kern AN, Addison P, Oommen T, Salazar SE, Coffman RA. Machine Learning Based Predictive Modeling of Debris Intermountain Western United States. Math Geosci. 2017;49(6):717–35.

172. Nikolopoulos EI, Destro E, Bhuiyan AE, Borga M, Anagnostou EN. Evaluation of predictive models for post-fire debris flow occurrence in the western United States. Natural Haz Earth Sys Sci. 2018;2331–43.

173. Qi C, Tang X. Computers & Industrial Engineering Slope stability prediction using integrated metaheuristic and machine learning approaches : A comparative study. Comput Ind Eng [Internet]. 2018;118(August 2017):112–22. Available from: https://doi.org/10.1016/j.cie.2018.02.028

174. Zhang Y, Ge T, Tian W, Liou YA. Debris flow susceptibility mapping using machine-learning techniques in Shigatse area, China. Remote Sens. 2019;11(23):2801.

175. Napoli M Di, Marsiglia P, Martire D Di, Ramondini M, Ullo SL, Calcaterra D. Landslide Susceptibility Assessment of Wildfire Burnt Areas through Earth-Observation Techniques and a Machine Learning-Based Approach. Remote Sens. 2020; 12(5): 2505.

176. Staley DM, Negri JA, Kean JW, Laber JL, Tillery AC, Youberg AM. Prediction of spatially explicit rainfall intensity – duration thresholds for post- fi re debris- fl ow generation in the western United States. Geomorphology [Internet]. 2017;278:149–62. Available from: http://dx.doi.org/10.1016/j.geomorph.2016.10.019

177. Addison P, Oommen T. Post - fire debris flow modeling analyses : case study of the post - Thomas Fire event in California. Nat Hazards [Internet]. 2020;100(1):329–43. Available from: https://doi.org/10.1007/s11069-019-03814-x

178. Puri N, Jain A. Correlation Between California Bearing Ratio and Index Properties of Silt and Clay of Low Compressibility. In Proc. Fifth Ind Young Geothec Eng Conf. 2015;(March 2020).

179. Puri N, Prasad, D. H, Jain A. Prediction of geotechnical parameters using machine learning techniques. Procedia Comput Sci. 2018;125:509–17.

180. Zhou Y, Li S, Zhou C, Luo H. Intelligent Approach Based on Random Forest for Safety Risk Prediction of Deep Foundation Pit in Subway Stations. J Comput Civil Eng. 2019;33(1):1–14.

181. James G, Witten D, Hastie T, Tibshirani R. An introduction to statistical learning. New York: springer; 2013.

182. Cannon SH, Gartner JE, Rupert MG, Michael JA, Rea AH, Parrett C, et al. Predicting the

probability and volume of postwildfi re debris fl ows in the intermountain western United States. Bull 2010;(1):127–44.

183. Staley BDM, Negri JA, Kean JW, Laber JM, Tillery AC, Youberg AM, et al. Updated Logistic Regression Equations for the Calculation of Post-Fire Debris-Flow Likelihood in the Western United States. US Department of the Interior, US Geological Survey.; 2016.

184. Friedman EQ, Santi PM. Debris-flow hazard assessment and validation following the Medano Fire, Great Sand Dunes National Park and Preserve, Colorado. Landslides. 2014;11(6):1093–113.